The Dissertation Committee for Michael William Brookman
certifies that this is the approved version of the following dissertation:

Experimental Measurement of Microwave Broadening by Fluctuations on the DIII-D Tokamak

Committee:

Kenneth Gentle, Supervisor

Roger Bengston

Herbert Berk

Gary Hallock

Philip Morrison

Experimental Measurement of Microwave Broadening by Fluctuations on the DIII-D Tokamak

by

Michael William Brookman,

DISSERTATION

Presented to the Faculty of the Graduate School of
The University of Texas at Austin
in Partial Fulfillment
of the Requirements
for the Degree of

DOCTOR OF PHILOSOPHY

THE UNIVERSITY OF TEXAS AT AUSTIN
December 2017

This work is dedicated to mankind's eternal quest for more power.

Acknowledgments

Mike would like to thank not just the plasma physicists who have guided much of this work, but whole cast that made it possible. He was recruited to the University of Texas by Doctor Bill Rowan of the Institute for Fusion studies. I joined the group of transport expert Ken Gentle. Without the wonderful administration of Teresa Garza, my paperwork surely would have fallen through the cracks years ago.The Graduate School at the University provided a generous recruitment fellowship, but it was these scientists who started me on plasma research during that first blazing hot summer in Austin. Those $104\deg C$ days made it easy to work long hours in the lab.

Hands-on research, building and calibrating hardware, provided an ideal introduction to plasma physics. I loved living in the City of Austin for graduate school - they made it a welcome place. Formative work at both Texas and Alcator C-Mod will not be forgotten, where skilled scientists were always quick with an observation and even quicker with a correction. I sorted most of these observations and corrections into a functioning scientist. After my time at Alcator C-mod, I took a transfer to a long term posting in San Diego at DIII-D. The fusion group here, both experimental and theoretical, provided help to this effort.

I would like to thank God and Mimi for getting me through this. Without their constant distractions, it may have gone faster, but it wouldn't have been nearly as worthwhile.

Experimental Measurement of Microwave Broadening by Fluctuations on the DIII-D Tokamak

Publication No. ____________________

Michael William Brookman, Ph.D.
The University of Texas at Austin, 2017

Supervisor: Kenneth Gentle

High gain, disruption free operation in tokamak fusion reactors requires the use of localized heating and current drive. Microwave power is the ideal tool for this purpose. Microwave power from gyrotrons is injected in focused, steerable beams which are absorbed by a thin layer of electrons at a resonant position in the tokamak's magnetic field. Heretofore, simulations and experimental benchmarking of deposition suggested a continuous, traceable propagation of this power from the edge to the deposition region. Recent work in analytic theory[1] and simulation[2] suggests that an untreated interaction between density fluctuations inherent to the tokamak edge will lead to scattering of the RF beam, broadening its deposition in the plasma. This work details the first experimentally derived scaling of fluctuational broadening. In a set of perturbative heat transport experiments on the DIII-D tokamak, deposition broadening has been studied. Electron temperature (T_e) measurements

from a 500 kHz, 48-channel ECE radiometer are Fourier analyzed and used to calculate a deposition-dependent heat flux generated by perturbative heating.

Consistency of the electron heat flux with a transport model is used to evaluate the power deposition profile. A diffusive($\propto \nabla T_e$) and convective($\propto T_e$) transport solution is linearized and compared with energy conservation-derived fluxes. Fitting agreement between these two forms of heat flux can be used to evaluate the quality of ECH deposition profiles, and a χ_2 minimization finds a significant broadening is needed over base 1D equilibrium ray tracing calculations from TORAY-GA. This work presents transport results and a validation of this transport fitting against past studies. The method is applied to a range of DIII-D discharges and finds a broadening of deposition which scales linearly with edge density fluctuation level. Simulation results from full wave[3] and beam tracing codes[4] which treat fluctuation effects can be evaluated through comparison with these experimental results.

As part of this work, upgrades have been undertaken to improve the radiometer system, with 8 tunable high-resolution channels based on Yttrium Iron Garnet spheres. Their narrow bandpass and flexible positioningincrease the resolution of measurements. Cross-calibration through density cutoff[5] has become an important application for the DIII-D ECE system, yielding a publication. Heat deposition measurements made as part of this work have already yielded one paper[6], with two journal papers, one experimental and one based on 3D full wave simulations[3], currently in review for publication in Nuclear Fusion.

Table of Contents

List of Tables

List of Figures

Chapter 1

Introduction

1.1 A Mandate to Develop Future Energy Technologies

A number of viable technologies seem poised to replace fossil fuels in the 21st century. Global oil reserves are sufficient to last through the century[7]. Development of new exploratory tools and extraction techniques can extend these resources, but extraction costs continue to increase, leading a substantial rise in the per-barrel price of oil, which topped \$100 in 2015 before falling to a still substantial \$50[8]. Growing awareness of the externalities related to fossil fuel use, together with the growing affordability of renewables are driving an energy revolution.

The extrinsic cost of using these fuels clear to scientists over the past two decades. Uncombusted hydrocarbon chains constitute a significant source of ground-level particulate pollution in the atmosphere. Increases in concentration of $10\mu m$ particles in the atmosphere are a consequence of gasoline combustion engines. A increase in concentration of these particles of just $10\mu g/m^3$ the background level can reduce life expectancy by over a decade[10]. These levels are regularly achieved in cities in the developing world. China experiences 1.6 million premature deaths a year related to pollution coming from

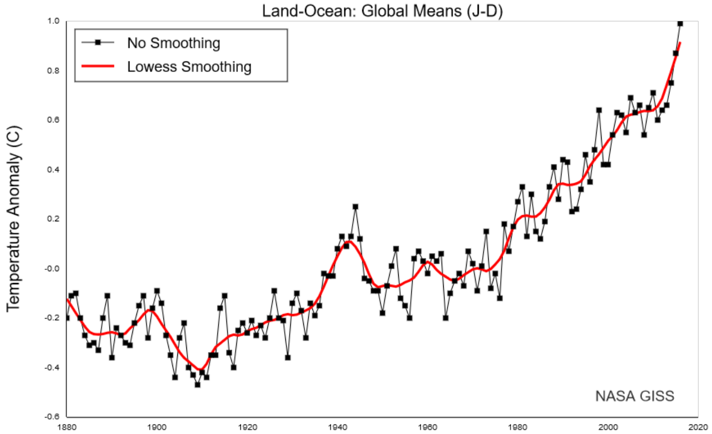

Figure 1.1: The difference between the yearly mean and average temperature over the past 140 years. The $0.5\deg C$ increase observed over the past half century could be the start of a much more substantial warming (fig, data c.o. NASA Goddard Institute for Space Studies).

chemical combustion reactions[11].

Even when hydrocarbon chains are optimally combusted and particulate sequestered, harmful gases are produced. Products hydrocarbons include carbon monoxide, carbon dioxide, and methane. These gases are generally acknowledged by scientists as contributing to climate change[12]. The mean surface temperature anomaly over the past century, as measured by the NASA Goddard institute for space studies, shown in Figure 1.1, has substantially increased[13].

Attractive options for replacing fossil fuels include include solar and wind power. These technologies are approaching economic competitiveness with fossil fuels in many areas[12]. The primary drawback of renewables is intermittency. Our Sun, currently the only functioning fusion reactor in the solar system, is occluded by the earth during much of the day. This phenomenon is referred to by scientists and others as night[14]. Similarly, wind generation is subject to environmental constraints. In catastrophic scenarios, these means of power generation may become untenable. True energy independence requires the ability to generate a baseline power capacity.

1.2 The Motivation for Tokamak Physics

The primary driver of magnetized plasma research is to produce fusion power. Under conditions of extreme temperature and pressure, nuclei can overcome the electrostatic potential separating them and interact by the strong force. Starting from Hydrogen with a single proton at Z=1 to Iron at Z=26, atoms require progressively less and less energy to bind them together. Thus a Helium ion (Z=2, A=4) - has less mass than its constituent 2 protons and 2 neutrons. During the fusion reaction, this mass is not lost but rather is converted into energy. The energy density of nuclear reactions is substantially higher than that of chemical reactions, increasing massively the yield per unit mass.

The conventional 'tokamak' design discussed in this work will use a combination of Deuterium (Z=1,A=2) and tritium (z=1,A=3), because of its favorable reactor cross section. A single D+T reaction produces an atom of Helium, a neutron, and 17.6 MeV of energy [15]. Fusion reactors produce limited radioactive waste, and don't have the same risk of catastrophic failure as fission reactors. These arguments taken together make fusion a compelling source of energy.

Fusion offers the highest energy density per unit fuel of energy technologies. 33 J/g of energy can be extracted from fossil fuels, compared to 2 GJ from the fission of Uranium. 340 GJ/g is released from the fusion of Deuterium and Tritium in Helium. Given the atomic masses of the constituent atoms the ratio of energy/mass ratio of fusion is .008 - 1 gram of reaction mass will yield .008 gc^2 of energy[15]. The only energy source known to have a higher yield is antimatter, which does not occur in significant quantities naturally and is incredibly difficult to synthesize. CERN is capable of generating small quantities of antimatter - 10 million anti-protons a day - which would produce 1 g of antimatter after 100 billion years[16]. This process is also incredibly costly, $\approx$ 250 Billion USD per gram. Given these constraints, fusion seems the ideal power source not just for terrestrial applications, but also for interstellar travel.

Achieving the high densities and temperatures required for deuterium-tritium fusion requires a means of containing very hot fuel. Deuterium-tritium fusion reactors require confining the behavior particles far hotter than the 6000 K surface of the sun. At fusion-relevant temperatures, no solid material can survive, requiring the use of alternative means of confinement. This work will explore the physics of heating in one such concept, a device called the tokamak, which uses a magnetic field to contain particles.

One metric of evaluating a fusion reactor's ability to confine energy and reach fusing conditions is referred to as the triple product. A combination of

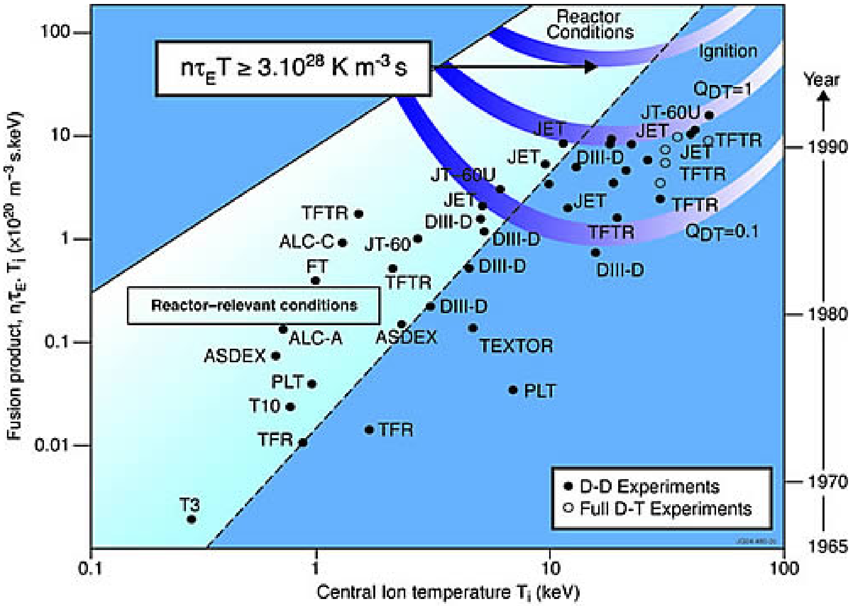

Figure 1.2: The triple product relates the density, confinement time, and ion temperature needed to achieve net-gain an a reactor. Some devices have achieved a fusion gain, $Q > 1$, but a significantly higher gain is needed for a power plant. The international thermonuclear reactor, ITER, is planned to reach Q=10[9]. (Figure courtesy of Eurofusion consortium[17])

the plasma ion density, n_i in m^{-3}, ion temperature T_i in keV (1 keV=1.2E7 K), and energy confinement time τ_e over which heat flows out from the plasma core are multiplied. Another metric is the fusion gain $Q = P_{fusion}/P_{in}$. Fusion devices need gains on the order of Q=10 to be a viable energy source. Figure 1.2 shows the factors achieved by existing devices. More work must be done to produce viable fusion reactors. Only by understanding the behavior of input power, and maximizing the ability of plasma to confine this power can fusion achieve its great promise.

1.2.1 Fusion Energy Density is a Path to the Stars

Even if one disregards the terrestrial energy applications in favor of renewable resources, only nuclear technologies offer the energy density necessary for long distance space travel. Fusion reactors offer an order of magnitude gain in energy per unit fuel mass over uranium fission with the added advantage of including an inherent powerful magnetic field which can deflect charged particles found in interstellar space. Miniaturization is a concern - the ITER reactor will have a mass of 20,000,000 kg, yet previous electrical generation technologies have always had a time to maturation. Although the viability of fusion power plants have not yet been demonstrated, the advantages are clear.

A future spaceship could potentially be built around a fusion reactor. We can consider an idealized tokamak as a baseline for this. The model D demo reactor planned by the European Power Plant Conceptual Study is planned to produce 2.5 GW of fusion power[18]. Such a reactor consumes .8% of the reaction mass to produce energy, and generates only a helium waste product that could potentially be used as a reaction mass. Sustaining this level of power product requires $7E20$ fusion reactions per second. This number seems substantial, but represents the consumption of only 6 mg/s of D+T fuel. Assume 2GW of this power is dedicated to propulsion using an ion drive, with the helium ash of the D+T fusion reaction as propellant. A back-of-the-envelope calculation, using this energy to produce momentum in a reaction mass of the helium ash, suggests that a thrust of 110 newtons could be achieved. While this is a factor of 10000 times lower thrust than the third stage of the Saturn

V rocket used by the US space program[19], such acceleration could be maintained for much longer times. The Saturn V Stage 3 can burn for only 500 seconds before it uses 110,000 kg of conventional propellant. 300 kg of fusion fuel can produce the same amount of force. While an earnest evaluation of such a concept will require many decades of advancement in fusion technologies, such advantages make a compelling argument for the development

1.3 Magnetic Fusion Concepts

A plasma with the temperature and density need for fusion is incredibly difficult to maintain. Any particle approaching a temperature where fusion becomes viable (1 billion Kelvin) would melt, vaporize, and ionize any material it contacted. Extended confinement of such plasmas requires the use of magnetic fields to retain the charged plasma particles -both ions and electrons. Imposing a magnetic field on a hot plasma limits motion perpendicular to the field - at the single particle level confines the hot plasma to fixed 'cyclotron' orbits along magnetic field lines (see Sec. 2 for a derivation of the cyclotron orbit). This behavior is the basis of all concepts in magnetic confinement fusion. However, in a homogeneous field, streaming along the field is unconstrained. A finite homogeneous field - such as that generated by a solenoid - will inevitable lose plasma from both ends. Building an infinitely long solenoid has and will remain beyond the United States Department of Energy's budget. Reactor concepts generally attempt to close this magnetic field in a symmetric way, retaining plasma. One early device used to confine plasmas is the magnetic mirror[20].

1.3.1 Magnetic Mirror

A magnetic mirror relies a set of coils which define high field throats around a lower field region - to confine particles[21]. Through the conservation of magnetic moment $\mu = 1/2mv_{\perp}/B$ - parallel velocity is converted perpendicular velocity as particles on gyro-orbits approach the coil. Most particles are 'trapped' by this magnetic field - confined to a circulating orbit inside the magnetic well. Particles with a sufficiently large perpendicular velocity component, defined in Eq 1.1, can remain trapped in such a configuration:

$$v_{\perp}/v > \sqrt{B_{low}/B_{high}} \tag{1.1}$$

Particles which have too much parallel velocity cannot convert sufficient momentum to turn as they approach the high field throat. These particles are in the 'loss cone' of the mirror. They proceed through the high field throat and are lost. In a collisional plasma, particles are inevitable scattered into this portion of velocity space[22]. Electrons move much faster than ions (thermal velocity for a species, $v_{th} = \sqrt{kT_s/m_s}$, has an inverse root dependence on mass) - leading mirror machines to have a much lower electron temperature than ion temperature. Particle losses out the end caps lower electron temperature to the point where mirrors quickly become unstable due to non-neutrality. Heating is viable in the ion channel and electron channels, but mirror machines are subject to diminishing returns from heating as the temperature difference grows too large. Modern mirror machines have great potential as a neutron source, but have limited applicability to fusion power generation[23].

1.3.2 Toroidal Magnetic Devices

The solution to losses out the endcaps of a linear device is topgraphically quite simple. Coils can be arranged in a circular loop, forming a toroidal magnetic field to confine particles. Within this broad category of toroidal plasma confinement schemes there are numerous examples. Early in fusion research it was found that a simple toroidal field was insufficient - the outer extent of the cross section has a lower magnetic field than the inner extent. This led simple toroidal schemes to experience substantial losses, as particles drifted from their orbits due to the field gradient. The application of an additional field can disrupt these drifts, although different schemes apply fields of varying complexity. We discuss in this chapter only the most reactor relevant concepts being explored today - stellarators and tokamaks.

These applied fields can be highly complex. Devices called stellarators, such as the German Wendelstein 7-X (shown in Fig. 1.3), use painstakingly-designed 3D fields to minimize currents in the plasma, reduce drifts, and avoid magnetic reconnection. Optimizing the field to such a great extend results in a highly complex magnetic geometry with no emphasis on gross toroidal and poloidal symmetry. Stellerators are capable of achieving substantial densities and temperatures, but these limits have not yet been thoroughly explored[24].

Using a simpler geometry based on an imposed toroidal field and a

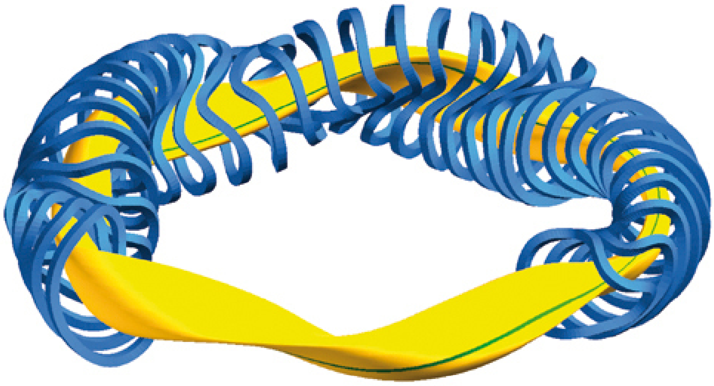

Figure 1.3: Magnetic coils and plasma of Wendelstein 7-X. The shape of the plasma is governed by the optimized magnetic field: It features fivefold symmetry, i.e. viewed from above, the plasma is not circular but resembles a pentagon. Optimization to avoid currents and trapped particle effects leads to the spiral shape of the magnetic axis and the varying, triangular to bean-shaped, cross-section of the plasma[24].

plasma-carried current which generates a poloidal field, the tokamak is the current world leader in fusion reactor design, both in terms of fusion triple product achieved and number of running experiments[15]. For the bulk of this work work, we consider the tokamak reactor, a classical design based a self-generated poloidal field. Reactor-relevant tokamak discharges will be explored in the international ITER[18] project currently being constructed in southern France. This tokamak, pictured in Fig. 1.4, will be the first fusion device to produce a substantial net gain, with an objective of a fusion gain (defined as Q=P_{fusion}/P_{in}) of Q=10[9].

1.4 The Tokamak

The word Tokamak is a direct transliteration from Russian, an acronym which translates to 'Toroidal chamber with magnetic coils'. The name describes the design philosophy aptly. Large magnetic coils are used to drive a closed toroidal field which confines a plasma. Current driven in the reactor then generates a poloidal field which stabilizes particle drifts out of the tokamak caused by inherent gradients in magnetic field, curvature, and electric fields. Particles stream along field lines in a helical orbit around the axis - averaging out much of the drift effect. This streaming behavior, in the ideal limit, defines a series of nested flux surface which are equilibrated through the high rate of parallel transport[15].

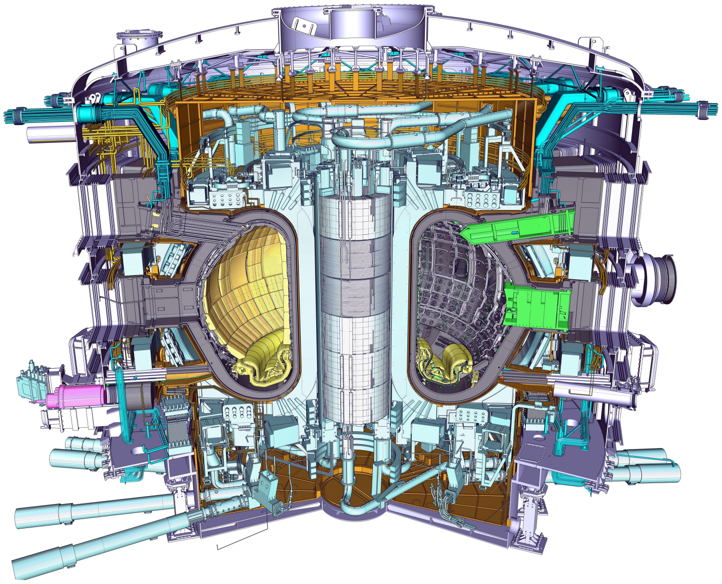

Figure 1.4: The coils and vessel of the ITER tokamak being constructed in southern France. While this machine may be the most complex engineering project being undertaken by mankind, the basic design possess a simple toroidal symmetry. A set of toroidal and poloidal coils define helical magnetic field which confines a plasma. ITER uses powerful external heating - megawatts of injected ion beam and microwave power - to create temperatures in excess of 100 million Kelvin[18].

1.4.1 Tokamak Geometry

Before continuing discussion heat transport physics in tokamaks, it is necessary to introduce a set of coordinates which describe the tokamak spatially. These are labeled in Figure 1.5, and defined in this section. These definitions will be used throughout this work.

The major radius, R, is the distance from the center stack of the tokamak perpendicularly outwards. The compliment of R is Z, the distance perpendicular to R. Z=0 defines the midplane, the greatest extent in R of the plasma. The minor radius, r, is measured from the axis of the tokamak. This axis is not an axis of symmetry, but rather is the point of highest pressure in the tokamak. The location of r=0 expressed in (R,Z) can vary with discharge. The poloidal angle θ, defines the angle between r and R. All of these coordinates exist in the cross-section of the tokamak shown in the figure. Toroidal angle, ϕ, defines the location around the torus, and goes into the page in Fig. 1.5. The tokamak is generally assumed to be symmetric in ϕ[15], and this work will consider cases where departures from this assumption are not significant.

1.4.2 Flux Surfaces and Flux Coordinates

The derivations and quantities in this section follow from the Wesson's *Tokamaks*[15]. The combination of poloidal and toroidal fields give rise to a set of equilibrating surfaces. Charged particles are free to stream along field lines. Therefore, along these surfaces, transport of heat and particles is so rapid that profiles can be considered in a 1D equilibrium. The equilibration along flux

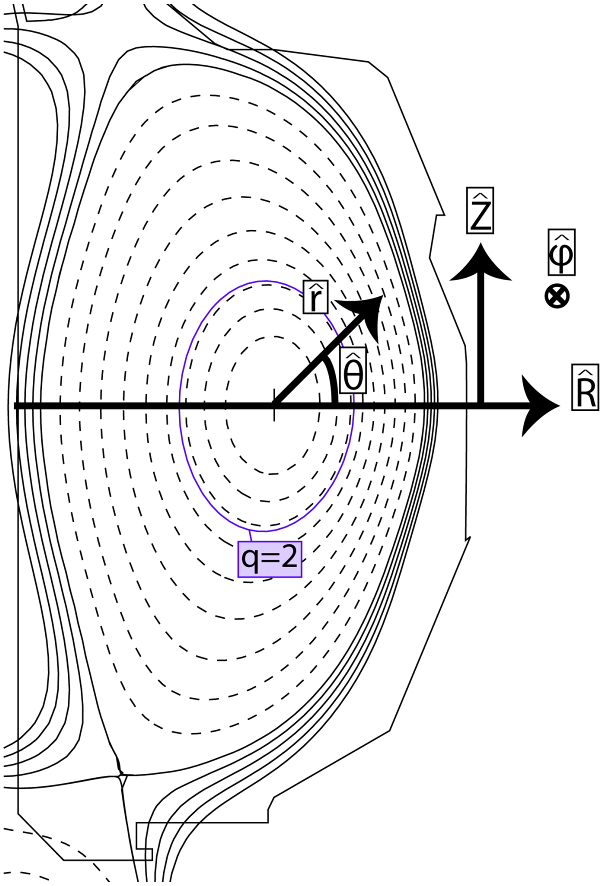

Figure 1.5: The spatial (R,Z), radial (r) and angular(ϕ,θ) coordinates are indicated in a figure of plasma cross section. Drawn in the tokamak cross section are surfaces of constant flux, along which many plasma parameters are approximately constant.

surfaces makes them a good basis for a radial coordinate in plasmas. These surfaces can be quantified in terms of the magnetic flux that passes through them, poloidally or toroidally.

The EFIT plotted in the previous section uses a normalized poloidal flux $\psi_n = \psi(r)/\psi(r=0)$, where psi is defined as

$$\psi = \int_{Sp} (\mathbf{B}) \cdot \mathbf{n} dS \tag{1.2}$$

where n is the normal to a surface drawn in the torus at Z=0, $R = R_0 + a$ (a fixed value of $\theta = 0$).

A toroidal flux coordinate, defined as $\rho = \sqrt{\phi(r)}/\sqrt{\phi(R=a, Z=0)}$ is commonly used as a radial coordinate for diagnostics. Here ϕ is the toroidal flux, defined by

$$\phi = \int_{St} (\mathbf{B}) \cdot \mathbf{n} dS \tag{1.3}$$

Where S_t is a surface drawn in the cross section (a fixed ϕ).

The winding of field lines can be found from the relative strengths of the fields. The ratio of the toroidal and poloidal magnetic fields defines the safety factor - a number expressing the pitch of the magnetic field lines as they wind around the torus:

$$q = \frac{d\Phi_{tor}}{d\Phi_{pol}} = m/n = \frac{rB_t}{RB_p} \tag{1.4}$$

q is referred to as safety factor because a high q value is protective against certain modes where are deleterious to plasma confinement. When q falls too much below 1, currents in the core can cause instability. Instabilities form and grow resonantly on rational q=m/n, where m and n are integer toroidal and poloidal mode numbers. A field with m=2 and n=1 can close on itself after making 2 poloidal circuits and 1 toroidal circuit of the tokamak. This effect generates large, 3D structures inside the plasma called tearing modes. The periodicity of the mode poloidally defines an x-point in the plasma - a helix of period m which twists toroidally according to n.

Modes with lower values of m/n are more deleterious as they grow more readily. When the safety factor is above 1, the tokamak is stable against a range of tearing modes with $n m$. When q is less than 1, a spectrum of modes will generally drive a 1/1 sawtooth oscillation which ejects plasma until the safety factor falls and the mode stabilizes[15]. In the absence of these modes, confinement along flux surfaces was classically expected to minimal. 1D flux surfaces in a toroidal configuration were expected to provide a confinement only hindered by scattering of particles called Bohm diffusion.

1.4.3 Classical Transport in Tokamaks

Based on this picture, classical Tokamaks expected a degree of confinement defined by a very strong scaling with magnetic field. Basic transport in tokamaks was predicted to be dominated by diffusion - collisions between particles being the primary means of knocking particles off of their simple orbits. Thus the loss of particles is diffusive, and can be considered dimensionally as a combination of collision scale and collision rate. Diffusive transport is a relationship between a differential flux and the derivative of the quantity driving the diffusive behavior, in this case particle density, such that $Q_e = D\nabla n_e$. Diffusion has units of distance squared over time. When particles collide in a reactor, their energy and momentum can be changed, but they still retain a cyclotron orbit. The scale length for these collisions is the gyro-radius of the cyclotron orbit defining confinement, ρ_s. The cyclotron orbit frequency, ω_c would determine a timescale for collisions. Bohm found the parameters determining the diffusion coefficient were temperature, T, charge e, and magnetic field, B[15].

$$D_B = \langle \delta \frac{x^2}{\tau_c} \rangle = \frac{\rho_s^2}{\omega_c} \approx \frac{T}{eB} \tag{1.5}$$

Experiments with larger fusion devices have found that transport generally exceeded this level, sometimes by an order of magnitude. Classical diffusion simply cannot account for observed heat and particle fluxes. Studies over the past decades have found that fluctuations in the tokamak are a source of significant transport [25]. The full plasma volume, but especially the edge, are defined by structures which extend well beyond a gyro-radius. Turbulence, especially in the tokamak edge, is discussed in Chapter 3 of this work. Turbulent transport drive substantial flows in plasmas, accounting for 80% of the heat and particle flux in some discharges[15]. This work will focus on transport fitting in microwave heated discharges which are entirely dominated by turbulent contributions[26].

1.4.4 DIII-D

DIII-D is a copper coil Tokamak which features powerful heating sources and a set of diagnostics which can measure a host of plasma quantities. It was developed in the 1980's by General Atomics in San Diego California from the earlier Doublet 3 device. It has a major radius of 1.67 m, minor radius .67 m, with a typical toroidal field of 2T. An inner wall of graphite tiles minimizes the sources of heavy impurities into the plasma. External heating power is provides through two means. Neutral beam injection uses a series of accelerator grids and neutralization to launch relativistic deuterium atoms into the tokamak. 7 70 kV beams have a combined 25 MW of power[27]. This work focuses on the applications of microwave heating in tokamaks. Six 110 GHz gyrotrons generate microwaves to be absorbed through a resonant interaction with the plasma electrons[28]. Gyrotron power is injected from above the midplane from any of 6 launchers at R=240 cm, Z=68 cm spaced around the Tokamak. Gyrotrons can be steered poloidally and toroidally Both beam and gyrotron heating sources can be independently power modulated at up to 3 kHz for feedback control and perturbative experiments.

DIII-D is also home to a powerful suite of diagnostics. Experimental measurement of tokamak quantities is the only means to produce a valid understanding of reactor physics. Tokamak plasmas can in part be quantified by the radiation they emit. Radiation diagnostics take numerous forms - active Thompson scattering uses scattering of laser pulses to measure both electron density and temperature profile measurements, albeit with a much lower time

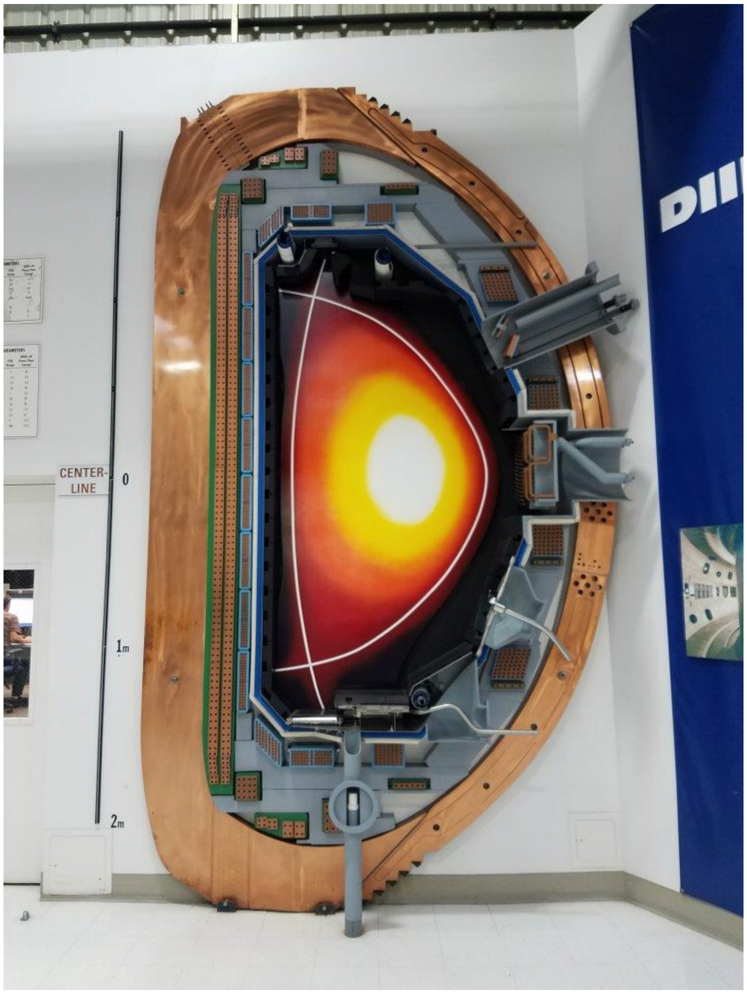

Figure 1.6: A cross-section mock-up of the DIII-D Tokamak. DIII-D. the large copper ring shown around the machine is a toroidal field coil. Other coils shape and provide a baseline poloidal field to the plasma. An ECH launcher, a part of special significance to this work, is shown at the top right.

resolution than ECE[29]. Neutral beams can drive line emission from charge exchange to measure ion temperature, density, and rotation[30]. The next chapter discusses passive measurements electron cyclotron of temperature[31]. Diagnostics to measure turbulent fluctuations are discussed in Chapter 3.

Chapter 2

Electron Cyclotron Resonance as a Diagnostic and Actuator

2.1 Basic Physics of Cyclotron Emission

This work focuses on the use of electron cyclotron emission as both a measurement tool and an actuator. Cyclotron emission is a natural consequence of confinement of charged particles in a magnetic field. Maxwell's equations provide the basis for understanding the emission and propagation of all forms of radiation. The plasma is a conductive, charged medium, with a strong anisotropy in the direction of the magnetic field. This nature gives rise to a complex propagation behavior as compared with the vacuum.

This chapter will explore in brief the nature of electron cyclotron radiation in plasmas. A single charged particle accelerated in a field will produce radiation, but it must absorb radiation as well. Starting from a single particle orbit, it is possible to derive the cyclotron frequency which characterizes this behavior. Interactions between emission and absorption of will alter the character of single particle emission. This behavior is actually desirable, the utility of ECH as a diagnostic and a heating method relies on absorption and thermalization through repeated interaction of radiation with particlese sig certain tokamak configurations and frequencies, cyclotron emission is a thermodynamic black body. This allows microwave calorimetric measurements to resolve electron temperature of a tokamak in a straightforward fashion[33].

2.1.1 Single Particle Motion

force The motion of a single particle in a magnetic field is the basis for this work, and more broadly tokamak reactors as a whole. A particle in an electromagnetic field experiences a Lorentz force. A charged particle of mass m, charge q, moving at a speed $\hat{v}$, in an electric field $\vec{E}(\vec{r})$ and magnetic field $\vec{B}(\vec{r})$ experiences a given by Eq. 2.1[34].

$$m\frac{d\hat{v}}{dt} = q\left(\hat{E} + \frac{\vec{v}}{c} \times \vec{B}\right) \tag{2.1}$$

The curl of the magnetic field causes charge particles to spiral, accelerating perpendicularly to both their motion and the magnetic field. When electric and magnetic fields are constant, the particle motion can be described by a helical orbit about a guiding center position, together with a set of drifts. This 'cyclotron orbit' is the basis of all magnetic confinement of plasmas. Changed articles are not free to cross magnetic field lines - they are forced to follow the closed field line of the plasma until they drift or are pushed out by collisions or flows. A symmetry exists when $\vec{v} \times \vec{B} = 0$, that is when the particle is traveling along the magnetic field lines. Separating this vector equation into perpendicular and parallel components relative to the magnetic field of amplitude B.

$$m\frac{dv_{\|}}{dt} = E_{\|} \tag{2.2}$$

$$m\frac{dv_{\perp}}{dt} = \frac{q}{c}(v_{\perp} \times B + E_{\perp}) \tag{2.3}$$

The motion of the cyclotron orbit is perpendicular to the equilibrium field - this motivates a trial solution $v_{\perp} = v_0 + 2\pi\omega_c\rho$ where ρ is the radius of the cyclotron orbit. Separating the angular frequency portion gives

$$m\frac{d\omega_c}{dt} = \frac{q}{c}(\omega \times B) \tag{2.4}$$

This equation has a solution $\omega_c = eB/m$ with a corresponding radius $\rho = \frac{mv_{\perp}}{|q|B}$. Furthermore, from the form of $E_{\perp}$ Eq. 2.3 shows a force against the magnetic field does not produce an acceleration, but rather a drift in the guiding center. Cyclotron orbits and drifts can be considered the single particle expression of plasma confinement and plasma losses.

2.1.2 Cyclotron Emission by Charged Particles

A charged particle will emit radiation as it accelerated through the cyclotron orbit. The form of this emission will be briefly summarized here referring to the derivation of Hutchinson[35].

The power radiated per unit frequency and solid angle per charged particle is given by Eq. 2.5.

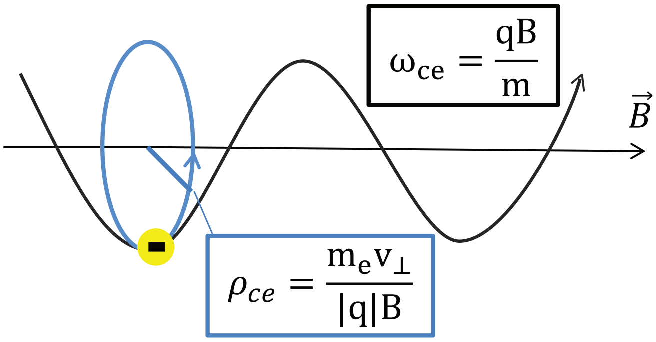

Figure 2.1: A basic diagram illustrating cyclotron motion. Particles stream around field lines in helical orbits.

$$\frac{d^2P}{d\omega d\Omega_s} = \frac{e^2\omega^2}{8\pi^2\epsilon_0 c}\sum_{m=1}^{\infty}\left(\left(\frac{cos\theta + \beta_\parallel}{sin\theta}\right)^2 J_m^2(\eta) + \beta_\perp^2 J'^2_m(\eta)\right) \times \frac{\delta(1-\beta_\perp cos\theta)\omega - m\omega_{ce}}{1-\beta_\parallel cos\theta} \quad (2.5)$$

The power emitted depends on the normalized perpendicular velocity ($\beta_\perp = v_\perp/c$), the harmonic of the cyclotron frequency, and the synchrotron ratio ($\eta = \frac{\omega\beta_\perp sin\theta}{\omega_{ce}}$)). This form gives the emission of a single particle.

The intensity of radiation emitted at a location is a function of a number of variables, but the local frequency of emission is dictated primarily by the delta function of equation 2.5,. Because $\beta_\perp$ is generally small (T_e/m_ec^2 is $\mathcal{O}1\%$) power is localized in a set of cyclotron frequency harmonics about the cold-plasma center frequency.

By integrating this equation over a distribution function it is possible to calculate the emission from a plasma. Calculating the emissivity j at a harmonic m from a non-relativistic collection of electrons in a Maxwellian equilibrium is a valid approximation for bulk cyclotron emission.

$$j(\omega,\theta) = c^3 \int \frac{d^2P}{d\omega d\Omega_s} f(\beta_\perp, \beta_\parallel) 2\pi d\beta_\perp d\beta_\parallel \tag{2.6}$$

A Maxwellian velocity distribution has the form of Eq. 2.7.

$$f(\beta_\perp, \beta_\parallel) = n_e (m_e/2\pi T_e)^{3/2} exp(-\frac{m_e c^2(\beta_\perp^2 + \beta_\parallel^2)}{2T_e}) \tag{2.7}$$

The intensity of radiation emitted at a location is a function of a number of variables, but the local frequency of emission is dictated primarily by the delta function of equation 2.5,. Because $\beta_\perp$ is generally small ($T_e/m_e c^2$ is $\mathcal{O}1\%$) power is localized in a set of cyclotron frequency harmonics about the cold-plasma center frequency.

Inserting $j(\omega,\theta)$ into the emissivity, and integrating it over solid angle, frequency, and distribution function, one finds an intensity.

$$\begin{aligned} c^3 \int \frac{d^2P}{d\omega d\Omega_s} f(\beta_\perp, \beta_\parallel) 2\pi d\beta_\perp d\beta_\parallel = d_\Omega & \\ \frac{e^2 \omega_m^2 n_e}{8\pi^2 \epsilon_0 c} \frac{m^{2m-1}}{(m-1)!} (sin\theta)^{2(m-1)} (cos^2\theta + 1)(\frac{T}{2m_e c^2})^m & \end{aligned} \tag{2.8}$$

In the next section, we'll see that at some frequencies, much of this power does not reach the edge of the tokamak due to reabsorbtion by other resonant electrons. Absorption of power at the second harmonic X-mode used on DIII-D is significant out to the edge of the plasma ($\rho = .25$), and an emitted photon has little chance of directly reaching the edge.

2.2 Propagation of EC radiation

A reactor-grade plasma consists of an amalgam of ions and electrons. In tokamak reactors $\approx 10^{20}$ charged particles cab occupy a single cubic centimeter. Even at the millimeter scale of cyclotron emission, there will be $\approx 10^{11}$ charged particles. Plasma is not strictly speaking, homogeneous, there are structures and flows which form across and along magnetic surfaces. In fact, turbulent inhomogeneities motivate this work and will be discussed in Section 3. To understand the basic nature of cyclotron emission, we will consider a simplifying assumption. When the inhomogeneity scale length is far greater than that of the radiation, the plasma can be approximated as a homogeneous medium, where the bulk local parameters dictate propagation.

This is possible when inhomogeneities are not substantial[36], called the Wendel-Kramers-Brillouin approximation. The WKB approximation treats variations in these parameters in a series expansion. For propagation through a cold plasma at electron cyclotron frequencies, we assume that WKB applies. Section 3.5 will discuss the necessity of simulations where fluctuations comparable to the cyclotron wavelength are significance. We consider the simple case which applied for diagnostic purposes. Here, prorogation is governed by Maxwell's equations. For a cold plasma perturbed by an equilibrium fields, there will be a flow generated in the plasma in the form of a current, **j**. S Eq.2.10.

$$\nabla \times \mathbf{E} = -\frac{\partial \mathbf{B}}{\partial t} \tag{2.9}$$

$$\nabla \times \mathbf{B} = 1/c^2 \frac{\partial \mathbf{E}}{\partial t} + \mu_0 \mathbf{j} \tag{2.10}$$

Combining these two equations with the assumption of plane wave solutions of the form: $\mathbf{E} = E_0 * exp(i(\mathbf{k} \cdot \mathbf{x} - \omega t))$

$$i\mathbf{k} \times (\mathbf{k} \times \mathbf{E}) + \frac{\omega^2}{c^2}\mathbf{E} + i\omega\mu_0\mathbf{j} = 0 \tag{2.11}$$

Assuming a cold plasma width a dominant magnetic field in a single directions allows for a relationship between $\mathbf{j}$ and $\mathbf{E}$ to be established. This relationship, known as the dispersion relation, produces a set of solutions for the wave propagation in the medium. These are defined by the angle between the electric field of the wave and the dominant magnetic field.

Radiation with its electric field perpendicular to the magnetic field is governed by the X-mode dispersion relation. This is called $N_\perp$, which has two branches because there are two directions which are not field aligned. Radiation with its electric field aligned to the magnetic field is governed by O-mode, $N_\|$ dispersion. The solution derived by[20] is reproduced below. It expresses the dispersion relation as a combination of cutoffs and resonances, based on a set of characterizing frequencies. These are the plasma electron frequency ω_{pe}, the left and right hand cutoffs $\omega_L \& \omega_R$ based on the interaction of the electron and plasma frequencies, and the lower and upper hybrid $(\omega_{UH}, \omega_{LH})$ resonances, which are named as they come from a 'hybrid' of ion and electron responses.

$$\omega_{pe} = \frac{n_e^2}{\epsilon_0 m_e} \tag{2.12}$$

$$\omega_R = \frac{1}{2}\left(\omega_{ce} + \sqrt{\omega_{ce}^2 + 4\omega_{pe}^2}\right) \tag{2.13}$$

$$\omega_L = \frac{1}{2}\left(-\omega_{ce} + \sqrt{\omega_{ce}^2 + 4\omega_{pe}^2}\right) \tag{2.14}$$

$$\omega_{LH}^2 = \frac{\omega_{ci}\omega_{ce} + \omega_{ci}^2 + \omega_{pi}^2}{\omega_{ci}\omega ce(\omega_{ci}^2 + \omega_{pi}^2)} \tag{2.15}$$

$$\omega_{UH}^2 = \omega_{ce}^2 + \omega_{pe}^2 \tag{2.16}$$

The dispersion relation for propagation through a dominant magnetic field can be expressed in terms of two branches based on the angle between the wave's electric field and the background magnetic field **B**[35]. O-mode radiation which has **E** aligned with the background field **B**, which is not considered further in this work, is defined by a simpler relation.

$$N_\parallel^2 = \frac{k^2 c^2}{\omega^2} = \omega_{pe}^2 \tag{2.17}$$

X-mode radiation, which is orthogonal to the magnetic field **B** has a more complex form with two branches.

$$N_\perp^2 = \frac{k^2c^2}{\omega^2} = \frac{(\omega^2 - \omega_R^2)(\omega^2 - \omega_L^2)}{(\omega^2 - \omega_{LH}^2)(\omega^2 - \omega_{UH}^2)} \tag{2.18}$$

This algebraic relation of X-mode contains a great deal of physical significance. When the refractive index goes to zero, radiation at a given frequency cannot propagate through the plasma. This is referred to as 'cutoff'. While cyclotron cutoff has some utility as a density measurement(see section 2.3.5) it generally frustrates temperature measurements and can lead to the reflection of injected RF heating beams. Cutoff of X-mode radiation is determined by the right hand cutoff layer, which is always higher frequency than the left hand cutoff.

2.2.1 Thermalization of Electron Cyclotron Radio-frequencies

The blackbody nature of cyclotron emission in tokamaks is the source of its utility for temperature measurements. Millimeter radiation is, fortuitously, strongly absorbed by resonant electrons at reactor-relevant densities and fields [37]. Absorption and re-emission of radiation enables the use of electron cyclotron emission as a thermal diagnostic.

The radiation equation (Eq. 2.19) governs the transport of cyclotron emission. It is a differential equation for intensity at a given frequency $I(\omega)$

as a function of emission $j(\omega)$ and absorption $\alpha(\omega)$.

$$\frac{dI(\omega,r)}{dr} = j(\omega,r) - I_f(r)\alpha(\omega) \tag{2.19}$$

The transport of radiation at one frequency is independent of the absorption at another in the limit of geometric optics, which. In a region where j and α are constants, an optical depth can be defined by integration, producing

$$\tau = \int_x^a \alpha(\omega_n, x')dx' \tag{2.20}$$

The optical depth in a plasma can be calculated from Bornatici[38]

$$\tau_m = \frac{\pi m^{2(m-1)}}{2^m(m-1)!}\frac{\omega_{pe}^2}{\omega_{ce^2}}(\frac{T_e}{m_e c^2})^{m-1}\mu^x_{\pi/2,m}\frac{\omega_{ce}R}{c} \tag{2.21}$$

Where for 2nd harmonic X-mode, m=2 and μ is defined as

$$\mu^x_{\pi/2,2} = |N_\perp|^{2m-3}\left[1 + \frac{(\omega_{pe}/\omega_{ce})^2}{m(m^2-1-(\omega_{pe}/\omega_{ce})^2)}\right]^2 \tag{2.22}$$

When the optical depth is higher than 2, the plasma can be considered optically thick. A statistical photon will undergo several absorbtion/emission can be said to be in thermal equilibrium. The ratio of emission and absorption become constant such that outside the region at some distance a, the measured intensity is given by a black body. A microwave photon at 100 GHz will have a fraction of an eV in energy ($10^{14} \times h \approx .4$), thus for plasmas which have temperatures of at least hundreds of eV, the Rayleigh-Jeans low frequency limit of a the classical black body formulation applies. Emission of a thermal plasma with a sufficient optical depth is a simple function of frequency and temperature.

$$I(r = a) = \frac{j}{\alpha} = \frac{\omega^2}{8\pi^2 c^2} T_e \tag{2.23}$$

Note that optical depth is in fact a function of density and temperature. The review of Erckmann[37] shows that for densities and temperatures of modern tokamaks, 2nd harmonic X-mode emission is the only optically thick resonance. On tokamaks with the higher density of ITER, both O-mode and X-mode will be optically thick. Scattering by fluctuations of O-mode microwaves is predicted by analytic theory to be stronger than X-mode[1], although O-mode heating are is not used on DIII-D and other current devices because of the 'shine-through' - poor absorption of power at achievable densities. For optically thick harmonics, emission can be localized as a result of the radial falloff in magnetic field, **B**, that comes from the tokamak geometry.

$$B = \frac{B_0 R_0}{R} \tag{2.24}$$

Because cyclotron frequency is a function of B

$$\omega_{ce}(m) = m \frac{eB}{m_e} \tag{2.25}$$

By observing a band in frequency of width $\delta\omega$, the one observed a specific emitting volume of the plasma. The localization diagram, Fig. 2.2, shows the first, second, and third channels of the DIII-D ECE system plotted versus major radius in the tokamak.

$$\delta\omega = m\frac{eB_0R_0}{m_e}(\frac{2r}{R_0^2 - r^2}) \tag{2.26}$$

The ECE channels on DIII-D measure a spectral width, $\delta\omega_{ce} < 1GHz$, corresponding to local emission in volumes at most a few centimeters wide. DIII-D has major radius $R_0 = 1.67m$ and minor radius $a = .67m$.

Cyclotron radiation is collected on the midplane to minimize the effects of propagation perpendicular to the flux surfaces[39]. In the tokamak, radiation equilibrates along flux surfaces, so the 1D measurements of ECE temperature. These are taken at specific locations in (R,Z), as shown in Figure 2.3, which are mapped to flux surfaces.

Thus ECE temperature profiles can be displayed against normalized minor radius coordinates, ρ and ψ_n.

2.3 Making ECE T_e Measurements

This section discusses the microwave radiometer hardware used to make measurements integral to this work. The high time and spatial resolution of ECE systems is necessary to measure the rapid transport of heat in tokamaks. The time resolution of Thompson scattering - the other source T_e measurements on DIII-D - is limited by laser pulse rates, which are 25-50 Hz for each of the 10 lasers. The DIII-D ECE system is a passive diagnostic with sufficient signal to be digitized at 500 kHz. High time resolution enables ECE to

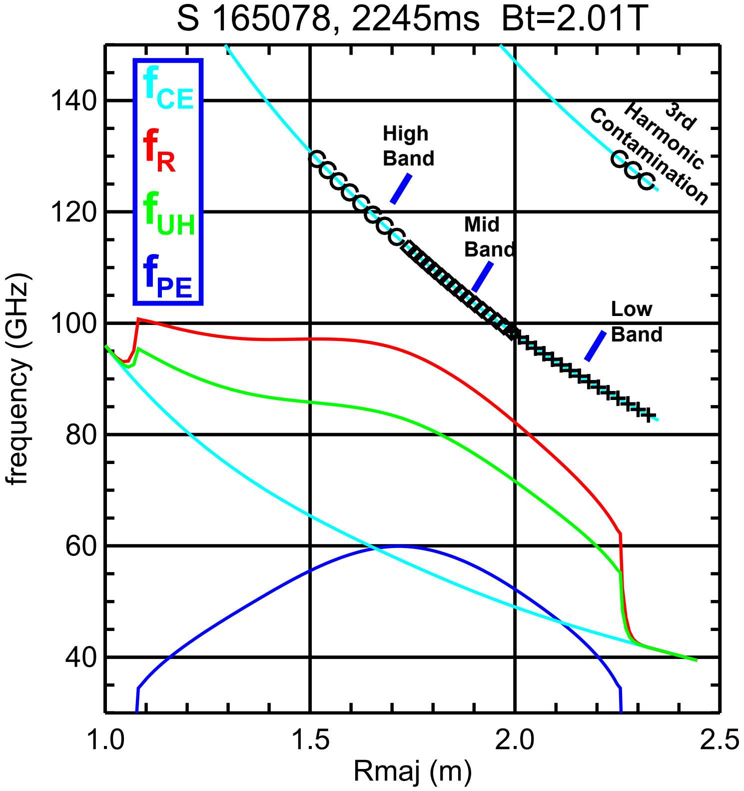

Figure 2.2: The frequency to spatial mapping in the DIII-D tokamak is shown together with significant frequencies for RF propagation. O-mode waves are cut off at the electron plasma frequency ω_{PE}. X-mode waves (the ones measured by the ECE radiometer) are cut off by the right-hand cutoff ω_{RH}. Marked positions are the measurement frequencies of the ECE radiometer, which is discussed in section 2.3.

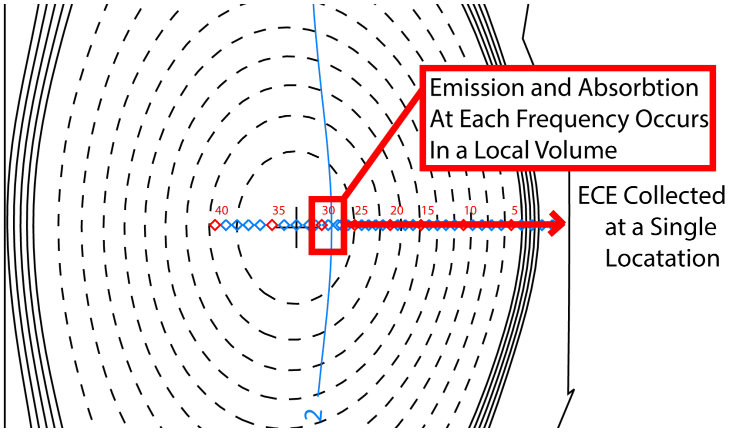

Figure 2.3: The location of the 2nd harmonic ECE resonances are shown in the tokamak cross section. ECE emission is collected by an array on the mid-plane, because emission is localized to specific frequencies and can generally propagate out freely.

quantify tearing modes, edge localized modes, and disruptions. For this work, high time resolution ECE data enables Fourier analysis of multiple harmonics of a 50 Hz ECH perturbation - in some cases up to the 15th harmonic at 750 Hz. ECE hardware and data storage routines have been upgraded as part of this work. In addition to the clear utility of its T_e measurements, the radiometer can also contribute to n_e measurements made by Thompson scattering on DIII-D.

2.3.1 The DIII-D Radiometer

The University of Texas operates the 40+8 channel heterodyne radiometer system on the DIII-D Tokamak. 40 fixed frequency channels, and 8 tunable channels are mixed off a baseline signal piped in from the Tokamak. A hardware diagram for the system is shown below. Broadband microwave emission is collected by an ellipsoidal mirror which focuses onto a scalar horn located 10 cm away from the DIII-D plasma. These collection optics create a 'Gaussian beam telescope', in which radiation is collected from a well defined Gaussian beam region of the plasma. This volume runs radially inward extending along the nominal midplane of the Tokamak at Z=2 mm Choice of frequency determines the radial measurement location along the beam, with the band. In this radiometer, the IF stage is limited by design to 20 GHz. Above this frequency, commonly available RF hardware suffers significant losses. 2nd harmonic X-mode is emitted from 82 to 122 GHz in DIII-D's rated toroidal field of $B_t = 2T$. Providing sufficient radial coverage over this range requires use of 3 heterodyne banks with local oscillators at 81, 97, and 102 GHz. These local oscillators provide a beating frequency which generates a frequency downshifted signal with a consistent power such that $P_{IF}(f = 2 - 20GHz) \propto P_{RF}(f = 84 - 102GHz)$. This hardware constitutes the radiometer's RF Mixer section, show in Figure below in Figure 2.4.

The IF sections of the radiometer convert emission from 2-20 GHz into the individual channel measurements. The low frequency band is pictured as an example in Figure 2.5. Through a combination of splitters and filters, the banks produce 40 linear signals with a bandpass of 400 MHz in the edge at the lowest frequencies (01-08), 500 MHz at mid radius (09-16), and 1000 MHz(17-40). The varying pass width was chosen to approximate a constant spatial width for each channel the $1/R$ falloff in magnetic field in the tokamak core, and to ensure sufficient signal level on each channel. A finer radial resolution

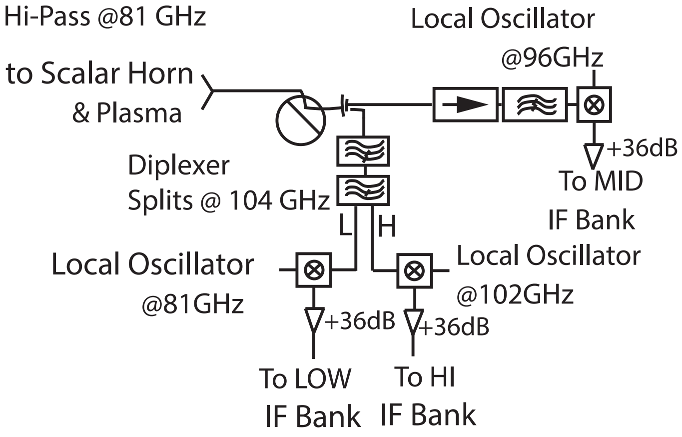

Figure 2.4: HF section of the radiometer. Input radiation is split into 3 banks through heterodyning and filtering. After mixing, the high (102-122 GHz), medium(99-117 GHz), and low frequency bands (81-101 GHz) can be carried to 3 IF sections by 1-20 GHz RF cables with SMA hardware.

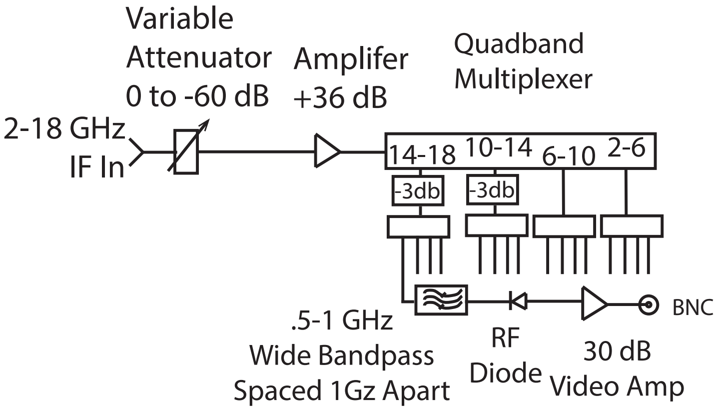

Figure 2.5: IF section of the radiometer. After the RF section, frequencies are mixed down to 20 GHz, which can be carried by SMA cables and processed with solid state hardware. Individual channels are split off using quadraplexers that minimize losses, and fed through bandpass filters to rectifying diodes that produce a digitizable voltage signal from each IF band.

can be produced by a narrower filter, but increased filtering also reduces the measured signal from the plasma. After filtering, IF power is converted to a voltage through use of a Schottky diode. The diode signal, 50 mV per μW of input power, is multiplied by a x250 video amplifier for capture. Two 50 channel D-tAcq digitizers, operating at 500 kHz and 20 kHz, capture the outputs of 40 fixed frequency channels as well as the 8 tunable YIG filters detailed in Section 2.3.2. Data is stored in the DIII-D PTDATA archive, while setup and calibration information is stored in the MDS+ database.

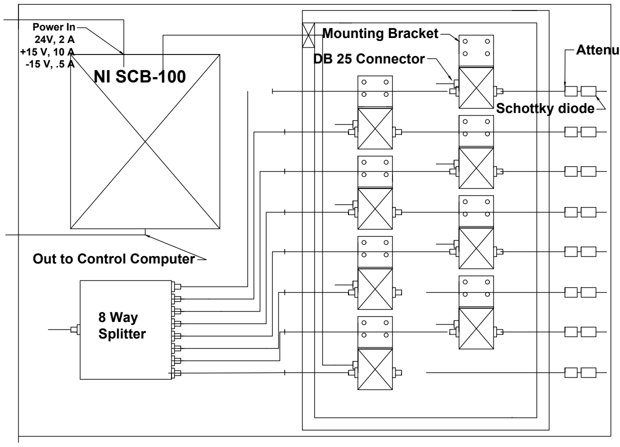

Figure 2.6: Located at the bottom of the existing radiometer cabinet, the 8 New Tunable Filters are split off from the fixed channel RF system and digitized simultaneously. These filters are designed to compliment the existing system with enhanced spatial resolution. Channels can be adjusted to increase measurement density in regions of interest.

2.3.2 Tunable Hi-Res Filter Bank

As part of this work, a system of tunable filters were developed by the author. The DIII-D Tunable YIG Filter System consists of 8 Micro Lambda YIG 3.75-18 GHz tinput bandpass a bank filters. A Yttrium-Iron-Garnet sphere is enclosed by an electromagnet. A field applied to a sphere determines a narrow microwave bandpass in the 2-20 GHz IF band. Filters are controlled by an NI SCB-100 which is fed by a PCIe-6509 controller system.

2.3.2.1 Filter Hardware

The YIG filter system is currently fed by a power splitter from the lowest IF frequency band (81-114 GHz) covering the full low field side in normal DIII-D conditions. IF power is fed through a 30 dB linear amplifier and 18 dB attenuator, An 8 way power splitter feeds each of the YIG filters, which are then rectified using Schottky Diodes, amplified, and digitized at 50 and 500 MHz using extra capacity on the 40 channel ECE system. As the filters operate at a 85 C set point for stability. A considerable amount of heat (120 W) comes from the coil current, and a 24 V heater coil is activated as needed. With the space constraints on the DIII-D system, the filters were enclosed in an insulated aluminum box, which limits airflow, allowing the filters to maintain temperature within the 22 C ECE cabinet. This enclosure must allow some limited heat exchange âĂŞ accomplished through venting the lid âĂŞ to prevent the internal temperature of the YIG box from becoming too high (95 C was reached in one case, approaching the rated limits of the DB-25 cables used to control the filters). Temperature is monitored with 2 NI TC-01 thermocouples.

The filters are fed with a digital control signal from a 92 channel NI DIO system which feeds an SCB-100 connection board (pictured). +15 V, -15 V and +24 V power is fed with a ground and 12 control bit signals which define a 4096 position range between the filter's minimum and maximum frequency, corresponding to steps of approximately 3.8 MHz. In practice, channels are tuned between discharges, making the time characteristics irrelevant, but filters can potentially be tuned during a discharge by using a triggered control sequence.

The 12 bit filter controller (corresponding to a 3. 7 MHz /bit step size for the 3.75-18 GHz range) NI PCIe-6509 92 Channel DIO board, wired through an NI SCB-100 to a custom breakout configuration which feeds into the YIG box. Control of this box is discussed in Sec II, but it should be noted that the level of TTL logic compared to system ground is very important. If a voltage greater than 6.5 V is applied to a logic channel, the filter could be damaged, thus our digital common is connected to the power supply's common terminal.

2.3.2.2 Labview Filter Control

Previous iterations of YIG filter, including some installed on DIII-D, have used an external voltage to directly drive the tuning coil. Counter-intuitively, direct tuning is undesirable for numerous reasons. These include consistency issues between supplies over time and with temperature, cost and controllability concerns, and noise pickup. Many manufacturers (ML included) responded by offering digitally controllable filters âĂŞ fixed supply voltages and control logic are fed to a circuit board which regulates coil current to produce a more reliable bandpass. The benefits are many: TTL logic is not sensitive to drifts or noise, meaning filter behavior is predictable, and the considerable DC currents (10 A @ 15 V for the DIII-D system) needed to drive these filters can be provided from a single well-regulated and filtered supply.

Control of the digital driver is accomplished through the use of an NI Labview VI (MultiYIG5.vi) (Fig Below). It takes in calibration information providing the bit setting to frequency relation, and uses this to set the center frequency of the filter bandpass to an input value. When a value is set, it is immediately written to the filters, and to the MDS+ model tree (shot = -1), such that the most recent setting is copied over when a shot is taken. The user must be careful to change values only between shots, but the instantaneous (10 ms) response of the filters allows the system to be set freely between them.

The program allows input of a calibration file which currently has the effect of writing the filter width at its set frequency to the tree. Also pulled from this file is the Dynamic calibration factor which will be used to adjust for the variable tunable filter pass. Changes are made by adjusting input values of center frequency set for the filters. Labview detects the changed setting and automatically adjusts the bit setting. Care should be taken to adjust filters only between shots. Check boxes enable writing of a log file, source for a .csv calibration file of appropriate format. On-off switches enable options including writing of calibration adjustment and, writing of filter settings to the -1 model shot.

2.3.2.3 Calibration of Tunable Filters

An immediate question arises when using tunable channels to measure T_e. How might the calibration, which relates the measured ECE band power linearly to temperature, change as the filters' frequency is adjusted? The answer to this question is found through calibration. While filters can be dynamically adjusted to match corresponding fixed channels, any time dependent sweeping of frequency will require some knowledge of the changing

The ECE band power in a band for a non-relativistic, optically thick plasma is

$$P_{EC} = \int I\left(f\right) kTdf \approx \delta f kT$$

[33]. From this power, an ideal linear rectifier diode (which is a good approximation for our Schottky diodes, in the range f= 0 to 20 GHz, P=-22 to -30 dBm [1-7 Îijw]) then produces a voltage, $V = C_1 P_{EC} + C_0$. The constant offset is found at zero power, but for our Radiometer, a comparison with the absolutely calibrated Michelson interferometer is necessary to produce C_1. This is done by averaging signal from a plasma over a time window in which the plasma is in a steady state. The Michaelson and the Radiometer should observe the same radiation temperature at the same emission frequency, and C_1 is set to match the Michelson temperature.

For a tunable filter, there is an addition concern âĂŞ adjusting the filter tuning can completely change the gain of the system (which is really a combination of the responses of every component âĂŞ splitters, filters, amplifiers, and even SMA barrel connections have a varying frequency response) - C_1 is a clear function of frequency, varying by as much as x3 over the range of a tunable filter. Because of this nest of dependencies, it is not advisable to calibrate individual components. It is instead advisable to feed the full system in place âĂŞ in our case after the LO/mixer that also feeds our outer fixed filter bank, allowing for calibrations that can be reliably referenced to the known fixed filters. Calibration is performed using a synchronized frequency scan from an Acopian Noise Source with a known input power, inserted before the Amplifier feeding the 8 way splitter, passing through the filter system to the Schottky diodes where it is digitized with an NI DAQ module. The bandpass is mapped using coherent averaging of a number of source frequency scans (see Fig next page). Numerical integration provides a total integrated power p at this frequency, and therefore allows one to adjust $C_1(f) = C_{1,base} * p_f/p_{base}$. The calibration factor, as well as the instrument function width and amplitude are acquired and stored by a Labview calibration program (tigL.vi) as waveform data in a .csv. An IDL program (yigcal.pro) analyzes this and then writes a file that can be read by the control program. In the future, it may be advisable to eliminate IDL analysis in favor of an all-Labview approach.

2.3.2.4 Results From Tunable Filters

The ECEview program /u/brookmanmw/runeceview allows quick display of ECE profiles for a given shot. It plots temperature profiles from the slow data vs any of frequency, R_{mid}, or Rho. The primary uses of the filters so far have been to improve the measurement resolution of magnetic islands.

2.3.3 MDS+ Storage

Nodes for the calibrated data from the HR and fixed filter systems have been added to MDS+. While PTDATA is used for initial acquisition

Node in ECE::TOP	**Size**	**Description**
$.SETUP.FREQ$	48	Center RF Frequency of Channel
$.SETUP : FLTRFREQ$	48	Frequency of IF Filter
$.SETUP : FLTRCALTBL$	$8xNcal$	Stored calibration grid for tunable filter
$.SETUP : FLTRBIT$	48	12 bit word as integer controls filter settings
$.CAL.CC1$	48	Linear calibration factor for slow ch.s
$.CAL.CC1F$	48	Linear calibration factor for fast ch.s

and storage, it does not have the ability to rewrite calibration factors âĂŞ necessary for the HR system which will eventually be tuned on a shot to shot basis. MDS+ data is also easily appended with dimensions, and could eventually be used for time-dependent calibration factors that would arise from a sweep in YIG frequency. The latest filter settings are written to the MDS+ model shot, -1. The model tree is then copied over to each new shot as it is taken. Adjustments made between shots do not then need to rewrite previous shots. Calibration Data can also be stored to the tree at later time, rather than immediately when the discharge is taken. Storing data in this form makes it independent of programming language, removing barriers to access. Python, IDL, and Labview all have MDS+ interfaces, and the MDS+ software itself is available free of charge. Below is a list of relevant nodes used by the Labview VI:

Temperature data from both the slow ($@/TECEXX$) fast digitizers ($@/TECEFXX$) is now available in a calibrated form for all 48 channels. Channel ρ positions will soon be written allowing for the localization of every channel. Using MDS+ routines, /u/brookmanmw/ecelib/get_ECE_mdsv1.pro âĂŸs get_ece_MDS loads out calibrated data from all 48 channels from the

MDS+ database. Recalibration is not done for the standard PTDATA pointnames. The MDS+ data structure does not have this drawback, so long as new factors are written, no external program is needed to process the MDS+ ECE data.

Using setup data the updated ecelocHR procedure located in /u/brookmanmw/ecelib/eceloc calculates the positions of all 48 channels in the tokamak, maps these to ρ and ψ_n and optionally applies a relativistic correction based on a user supplied density file.

2.3.4 Relativistic Corrections to Radiometer Measurements

In the relativistic limit the cyclotron frequency goes as, ÏĽ$_e c = eB/m$Îş with most ECE deposition calculations using the approximation ÎşâĽĹ1. For plasmas below 4 keV, this approximation is sufficient - shifts are small compared to the 1 cm inherent widths of the fixed frequency radiometer channels. For a hotter plasma, this kinetic effect becomes more important. It is possible to perform a relativistic correction to the ECE channel positions by calculating the ECE channel positions by the method of Bornatici et al. The kinetic corrections to the emission and absorption are calculated along the ECE line of site.

The emission of radiation turns out to be broader than the cold plasma resonance, as shown in Figure 2.7. The distribution function's exponential falloff means at modest temperatures the two frequencies are comparable, below about $3keV$ the relativistic correction is less than 1%.

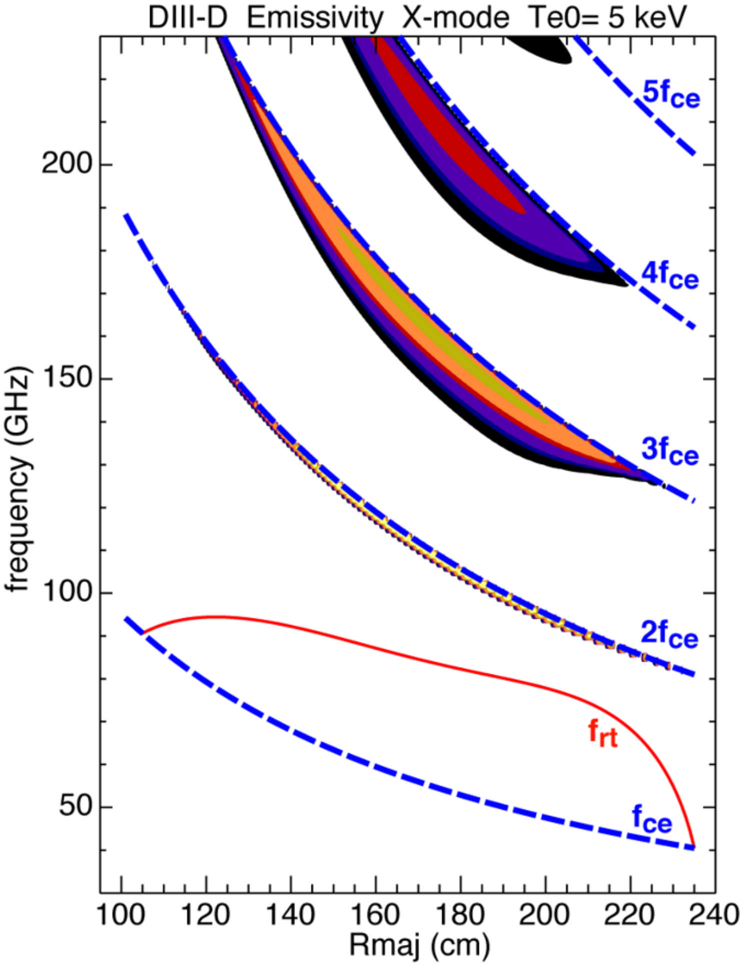

Figure 2.7: The relativistic effects modeled for a warm plasma broaden the cold radius significantly. A heat map shows the center of emission below the cold frequency, known as relativistic downshift. The first harmonic of X-mode is always cut off, as the plasma frequency defines a minimum for f_{ce}. Higher harmonics are more strongly perturbed, but even the second harmonic can see broadening on the order of hundreds of MHz in a 5 Kev DIII-D plasma. Fig C.O. ME Austin *et. al.*

For X-mode radiation (relevant for DIII-D's heating and diagnostic systems) the absorption has be found in a weakly relativistic limit to have a simple analytic form expressed in four algebraic equations.

$$\alpha_n = A_n \frac{n^(2n-1)}{2^n n!} (\frac{\omega_{pe}}{\omega_{ce}})^2 (\frac{T_e}{m_e c^2}) \tag{2.27}$$

$$A_n = N_{\perp}^{(2n-3)} \left[1 + \frac{(\omega_{pe}/\omega_{ce})^2}{n\left[n^2 - 1 - (\omega_{pe}/\omega_{ce})^2\right]^2} \right] \tag{2.28}$$

$$F_q'' = -\frac{\pi}{\Gamma(q)} |z_n|^{q-1} e^{-|z_n|} \tag{2.29}$$

$$z_n = \frac{m_e c^2}{T_e} \frac{\omega - n\omega_{ce}}{\omega} \tag{2.30}$$

A method has been develop to perform this correction based on electron temperature and density profiles from Thompson scattering. An example calculation for a single channel from a DIII-D H-mode with a core temperature of 5 keV is shown in Figure 2.3.4. Absorption of emitted power actually occurs entirely inside the cold resonance. The difference between the peak frequency of emitted power and the true cold resonance depends most strongly on electron temperature, with the difference becoming significant only above 3 keV.

As part of this work, a routine to make this calculation based on Thompson n_e and T_e profiles for all 48 channels was developed by the author

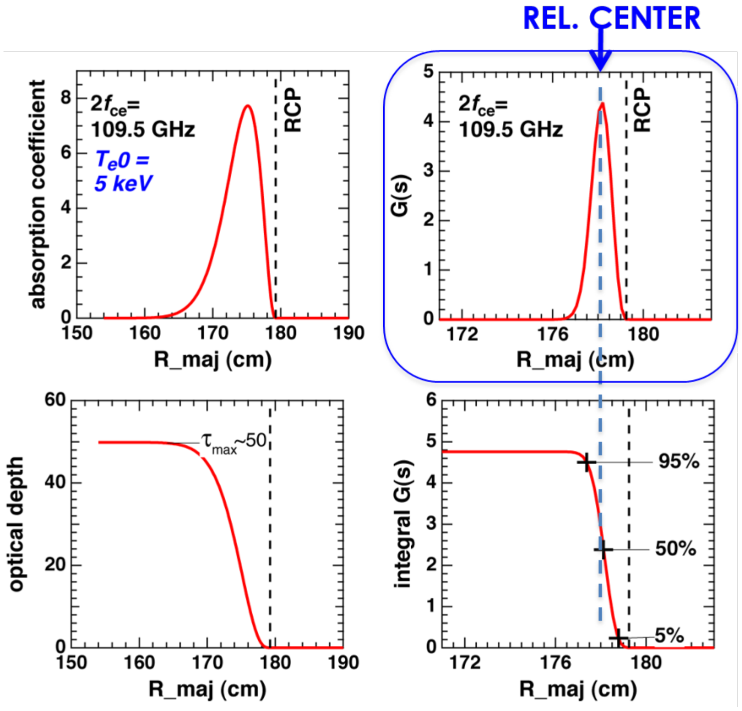

Figure 2.8: Absorption coefficient, emissivity, optical depth, and integrated emission are shown in this figure. High temperature conditions in fusion grade plasmas cause emission and absorption to shift away from the cold plasma resonance. Temperature and density dependent calculations can be made to correct for shifts away from the cold plasma resonance. Figure C.O. M.E. Austin

in the IDL language. The ECE channel positions shown in this work have been calculated by this method, including relativistic effects where applicable.

2.3.5 Novel Applications - ECE as an n_e diagnostic

Electron cyclotron emission has seen much application as a temperature diagnostic. By watching as that temperature measurement fails, ECE can be used as a density diagnostic. As discussed in section Thomson scattering (TS) is used to measure electron temperature and density on DIII-D and many other tokamaks. Thomson n_e and T_e measurements provide baseline profiles used for transport analysis, modeling, and kinetic equilibrium reconstruction. All these applications are sensitive to the absolute values of these quantities and their spatial gradients. An initial calibration of the DIII-D Thomson system is performed using Raleigh scattering in a reference gas. This produces a linear factor for each chord and laser, $C_1 \times I_{scattered} = n_e$ with a 5% uncertainty. The calibration is subject to drifts with a characteristic time on the order of 500+ discharges over 3-4 weeks of plasma operation. Fits of ∇n_e are highly sensitive to these drifts and error levels. Calibration of the core TS system is found to be significantly improved with regular use of the density-driven cutoff of electron cyclotron emission.

The right-hand cutoff, ω_R increases with density. When ω_R exceeds locally the frequency of 2nd harmonic X-mode ECE, that radiation cannot propagate though the region. This is expressed as

$$2\omega_{ce} \leq \omega_R = \frac{1}{2}(\omega_{ce} + \sqrt{\omega_{ce}^2 + 4\omega_{pe}^2}) \tag{2.31}$$

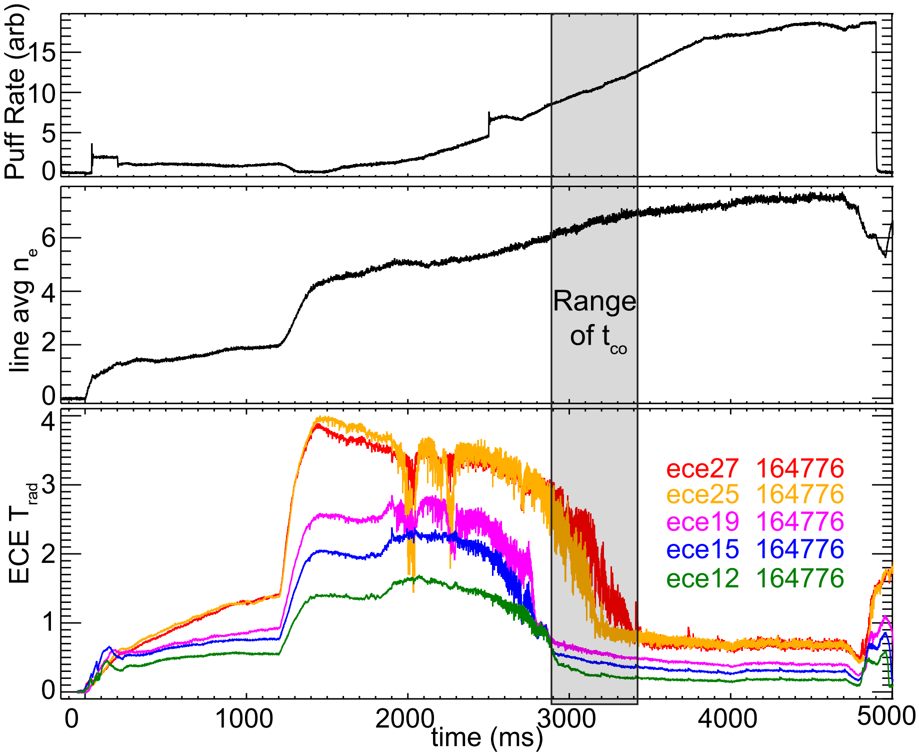

Figure 2.9: Time traces from a cross-calibration discharge. A ramp in gas puffing produces an increase in density which drives ECE channels into cutoff. At the time of cutoff t_{co} on each channel, the local density is the cutoff value n_{co}.

Where

$$\omega_{pe} = \sqrt{e^2 n_e / \epsilon_0 m_e}$$

is the electron plasma frequency and $2\omega_{ce}$ is defined by the center frequency of each filter channel. This creates an intrinsically stable absolute calibration value which depends only on the flux mapping between the ECE channel and the Thompson system.

An increase in n_e can be induced across the plasma through a gas ramp in an H-mode discharge with good particle confinement. An uptake of gas sharply increases density in the edge, driving $\omega_R(r)$ above $\omega_{ce}(r)$, and emission drops leading to drop in the measured radiometer temperature as shown in Fig.2.3.5. Cutoff occurs first at the top of the pedestal, and the density increase propagates corewards over a variable time on the order of $\approx 100MHz$. Edge channels will often fall into cutoff shortly later. The rate at which cutoff occurs has been observed to be enhanced by ECH heating and RMP these channels fall into cutoff. Fig. 3 shows $T_e(t) = arctan(ct - t_{CO})$ is fit to each channel, producing the center time of the cutoff, t_{CO}. At the cutoff time, fit for a core channel in Fig. 2.3.5, the density at the observation location for an ECE channel must be the cutoff density for 2nd harmonic ECE emission at that channel's frequency.

Solving $2\omega_{ce} = \omega_R$ gives the cutoff density for each ECE channel as a function of frequency:

$$n_{CO}(m^{-3}) = 2 * (f_{ce}(Hz))^2/80.64 \tag{2.32}$$

This n_{CO} is mapped from the 2nd ECE channels to the Thomson chords using an EFIT 1D equilibrium. At the time t_{CO}, the Thompson density is corrected to match n_co. A reconstruction for a typical TS cross-cal shot is shown in Fig. 2. So long as gas is not supplied too abruptly, the plasma shape and 1D symmetry is maintained throughout the cutoff.

This method has been used successfully the last decade on DIII-D.

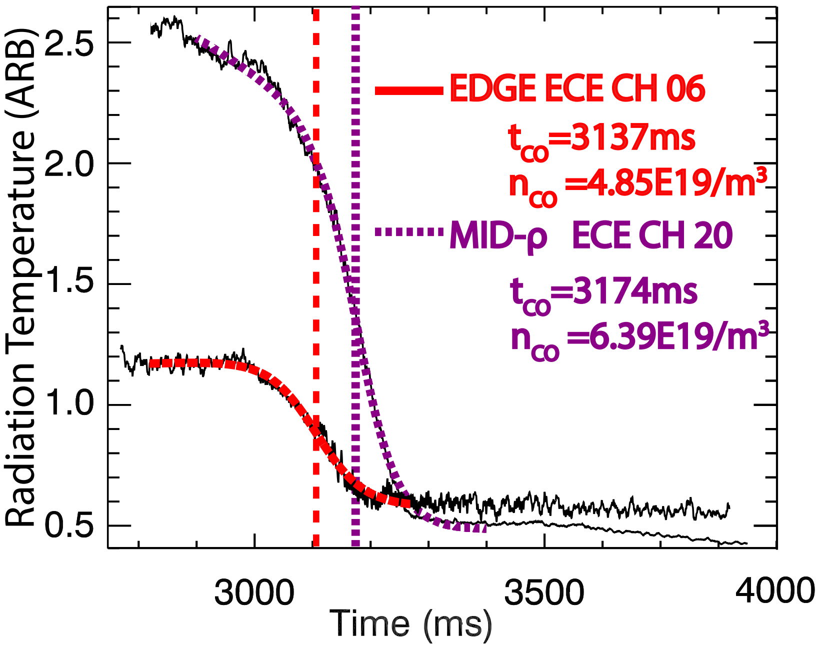

Figure 2.10: Cutoff fit times and densities for two ECE channels. The ECE temperature is fit with an arctangent centered at $t = t_{CO}$. This reliably finds a cutoff, so long as the change in density across the channel is smooth. The user input into the fitting algorithm is only a start and end time for the fitting form.

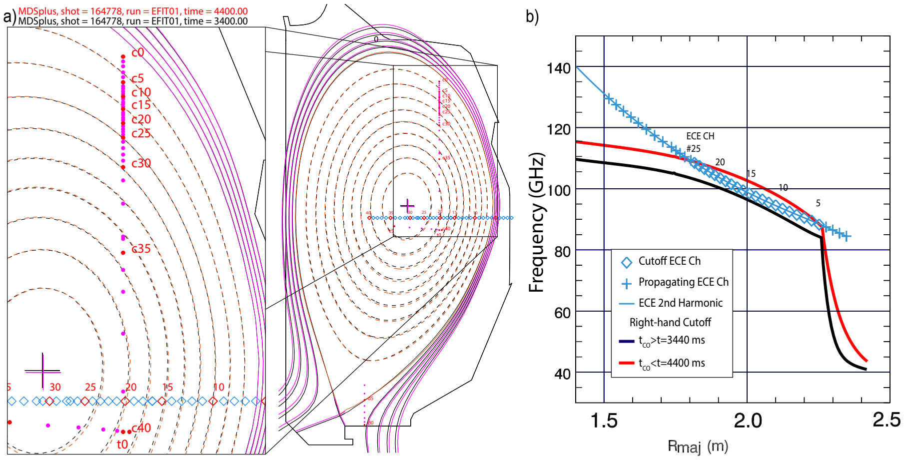

Figure 2.11: A reconstruction of the ECE/TS Cross-Calibration discharge. High upper squareness discharge brings all Thomson channels inside the seperatrix, where the 1D equilibrium assumption is valid. ECE channels are indicated with diamonds and TS channels with dots. The reconstruction before cutoff is shown in black, after cutoff in red. The equilibrium can be sustained if density is not ramped too sharply.

It reduces the uncertainty of n_e measurements from a 5% uncertainty to a 2%[5]. This improvement cannot be achieved by other methods such as CO2 interferometer cross-calibration, or Rayleigh scattering from neutral gas. Fig. 2.3.5 shows a profile before and after a ECE/TS correction. Improvement in the steep gradient region in the edge is substantial, enough to alter the local gradient by a factor of 4.

While the absolute magnitude of the shifts is small, they produce a much smoother profile - especially in the pedestal region. As a result the density gradient, ∇n_e can be determined much more accurately. While T_e measurements are primary purpose of the radiometer, this cross-calibration has become another valuable contribution to the DIII-D effort. It is performed at

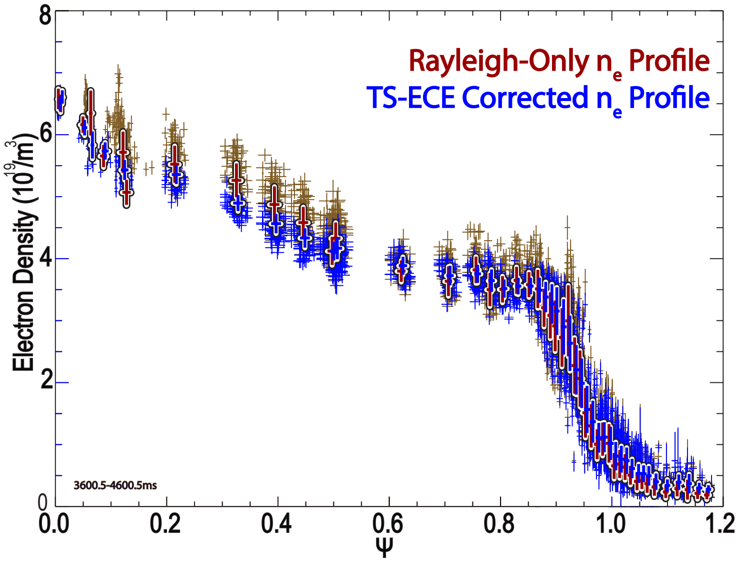

Figure 2.12: Density profiles before and after a TS/ECE correction. The corrected profile shows significantly less scatter in the pedestal and also significant changes in the local gradients.

the start of every campaign to improve the quality of Thompson measurements.

2.4 Using Microwave Power in Tokamaks

Microwave power has a number of applications in tokamak physics - local electron heating and current drive can be used to tailor T_e and q profiles[40]. It can be used to drive breakdown - producing the initial plasma to start a reactor[41]. Local current drive is especially important for future devices as it can repair deleterious structures which form in the plasma[42]. This section will review in brief the basic generation, applications, and measurement of power deposition.

2.4.1 DIII-D Gyrotron Systems

To produce microwave power, DIII-D uses a series of gyrotrons designed by Communication & Power Industries of Palo Alto, California. A gyrotron, pictured in Fig. 2.4.1, works by accelerate electrons within a precisely machined cavity to generate microwave power at the designed millimeter-scale wavelength. Electrons are launched from a triode located RF power is collected and transmitted by a waveguide system to the DIII-D tokamak, where it is injected to heat and drive current in the machine. An array of 6 110 GHz gyrotrons, with a 7th 117 GHz gyrotron in testing, is used to support DIII-D operations[28].

Gyrotron power can be modulated by capping the voltage on the Triode emitter. Power output will be suppressed for a period of time as emission of new electrons is limited. In practice, power can only be suppressed for a short duration before an arc occurs. This limits the minimum modulation frequency achievable without losing power. For this work, a range of modulation frequencies, from 7 to 1500 Hz were explored. On the high end, diagnostic response provides a limitation. Above about 3 kHz, modulation effects, even at full power, approach the noise level of the ECE diagnostic. This modulation capacity will prove key to transport analysis.

2.4.2 Changing Plasma Turbulence

This work focuses on direct perturbative transport measurements, but the applications of microwave heating power are numerous. For example,

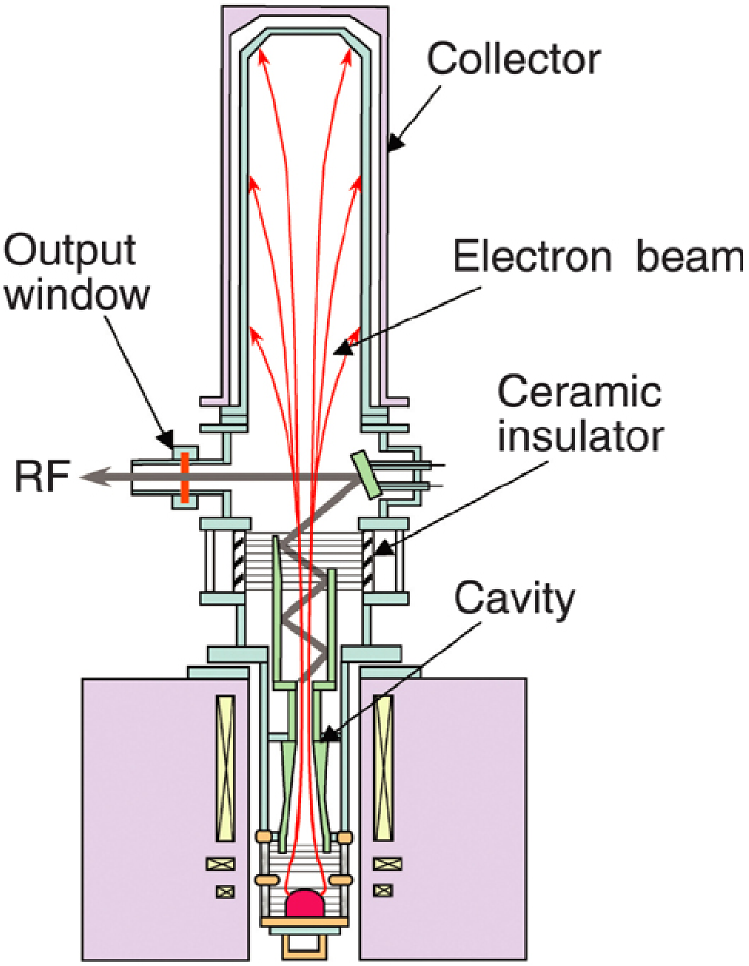

Figure 2.13: An internal schematic of a fusion-grade gyrotron. Electrons are emitted by the triode indicated in red at the bottom of the figure. Electrons flow up through a precisely designed magnetic cavity which causes emission of cyclotron radiation. The high-field point of the cavity is optimized for emission at a specific frequency. Emission from these electrons is captured and focused out of the gyrotron, and onto a waveguide system which directs it into the plasma. This diagram is reprinted under fair use from the Journal of Fusion Science and Technology[43].

ECH can be used to adjust the ratio T_e/T_i. In current generation devices, this number is often below unity, as ion heating through NBI and Ohmic resistivity dominates. Alpha-heated fusion reactors will have T_e/T_i near unity , and this ratio has been observed to drive changes in physics[44]. Significant changes in particle and heat transport have been observed with changing T_e/T_i with substantial impact on profiles and mode behavior. Gyrotron power can increase T_e/T_i in existing devices, allowing them to explore the underlying physics of this parameter. Results suggest that many of the changes with an increasing electron to ion ratio are a result of changing turbulence[45]. Turbulence modulation will need to be avoided in these studies, so as not to alter the underlying transport of measured heating power.

2.4.3 Suppressing Tearing Modes

Tearing modes are structures that form on rational surfaces in a plasma. To the 1D ECE system located on the plasma midplane. Turbulence leads to the formation of island structures through a sort of pinching of flux surfaces, turning a 1D topography in cross section to a 2D profile. Measured the ECE system on the midplane, this appears as a flat spot in the plasma profile (Fig. 2.14).

The motivation for studying the broadening of RF deposition is the locality of current drive. Microwave power, when injected with a substantial $k_\parallel$ component along the field lines, will preferentially interact with a subset of particles in velocity space. Increasing the $v_\parallel$ of some electrons, distorting the

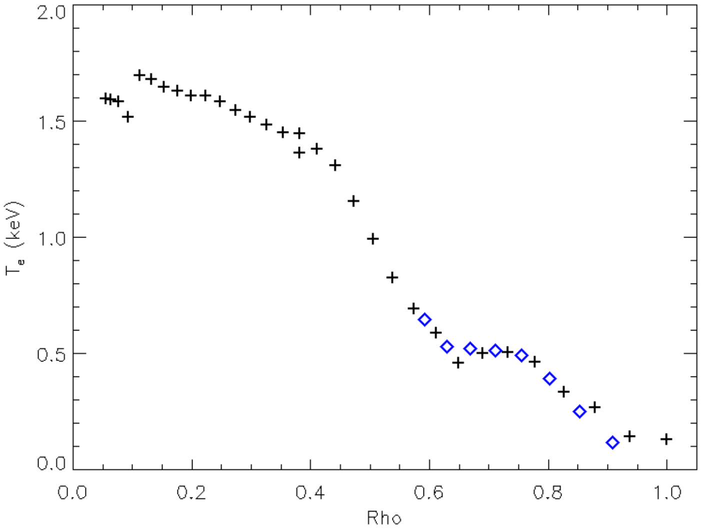

Figure 2.14: Electron temperature ECE measurements from a discharge show the consequences of profile flatting due to a magnetic island, here a 3/2 tearing mode. The island centered at $\rho = .7$ in the tokamak dramatically reduces core temperature achievable in the machine.

basic Maxwellian in velocity space and producing a net current in the toroidal direction[37]. The effect of this is to generate a current in the plasma. Power deposition and current drive profiles have a self consistency to their widths. The ECCD current drive profile can in fact be calculated from the basic power deposition profile. Following from Petty *et. al.*:

$$I_{ec} = P_{ec}\frac{\epsilon_0^2}{e^3}\frac{kT_e}{\ln \Lambda R n_e}\zeta(Z, \epsilon, \theta_{pol}, \omega) \tag{2.33}$$

Here, I_{ec} is the ECCD driven current, P_{ec} is the power deposition profile, R is major radius, T_e and n_e are electron temperature and density respectively. The $ln\lambda$ is the classic coloumb logarithm, which varies only weakly is of order 10 in tokamak plasmas. ζ is a dimensionless factor, based on poloidal angle, effective charge, and a normalized electron thermal velocity. Increases in the power deposition profile lead to a commensurate increase in ECCD profile width. Should the ECCD width be increased, this has consequences for the current drive.

The magnetic island associated with the NTM has a 2D structure- a perturbation which is extended along the field lines. The topography forms a series of 'O-points', where the gradient is not fully relaxed, and 'X-points', where the transport is directly enhanced. It is the O-point islands where current drive with ECCD is targeted[46]. Driving current in the O-point can force the island chain to open, destroying the X-point by replacing the deficit it drives in the bootstrap current[47]. The relative width of the island structures

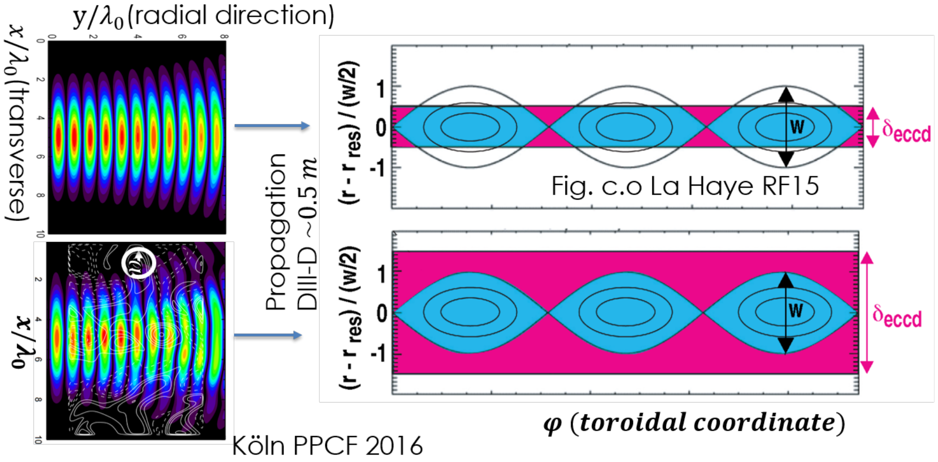

Figure 2.15: This schematic cartoon shows the consequences of fluctuational broadening. A wider beam propagating in from the edge will have a wider deposition in the plasma. When this is larger than the island width, power is lost.

and current drive is significant, because current not driven outside the island does not help to heal the structures. This issue is illustrated in Figure 2.15 , which combines work from Koln[2] and La Haye[48]:

In practice, ECCD deposition width is predicted by codes, which are then benchmarked against experiments. In the next section, we discuss one of the codes used to make predictions for ITER.

2.4.4 TORAY-GA Ray Tracing

The primary means of predicting the deposition of microwave heating and current drive at DIII-D is the code TORAY-GA. TORAY is a ray-tracing code developed by John Kinsey originates from the older RAYS code developed by D. Batchelor *et. al.*[49].

TORAY characterizes RF deposition by drawing a number of rays (100 in these simulations) starting from the EC launcher. The ray is broken into a series of differential steps, calculated iteratively inwards. Absorption and defraction are calculated for each ray increment. The power which is not absorbed is advanced an increment into the plasma, then the absorption and path are recalculated. Rays are propagated until 99% of power is absorbed, or until the ray hits the inner wall. A density-driven cutoff leads to reflection of the ray, and studies using this capability to map reflected power to the tokamak wall are important for machine protection. As discussed in the opening of this section, use of 2nd harmonic X-mode power means that, over the full range of densities and temperatures explored in this efforts, that absorption is 100%[37].

As inputs, TORAY-GA requires an equilibrium reconstruction, profiles, and aiming parameters. Equilibrium information can be provided as an EFIT g-file or as a ONETWO 'psiin' file. These files contains information about the magnetic properties of the tokamak - a characterization of the toroidal and poloidal magnetic field, flux surfaces, and plasma boundary. Profile parameters, $n_e(\rho)$, $T_e(\rho), Z_{eff}(\rho)$, and aiming information are provided in the 'echin' ASCII file. An additional 'TORAY.in' namelist file can be used to define the injected source, ray behavior, and desired output files. Examples of the profiles used are shown in Figure 2.16.

For this work, an interface has been set up in the OMFIT python package to generate batches of TORAY files based on the OMFITprofiles module.

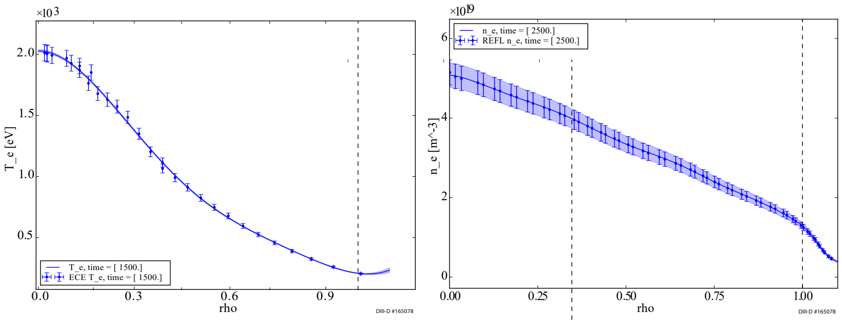

Figure 2.16: Electron temperature and density files form a key input into TORAY-GA. These, together with the equilibrium of Fig. 2.17, allows for calculation heat deposition. The heating cyclotron resonance is susceptible to kinetic and optical depth effects which are treated by the code. In the original ECHRES package, a fixed Z_eff=1.75 is used, but OMFIT allows this Z_eff fit in the OMFITprofiles package to be used instead.

For a chosen shot and time, magnetics and equilibrium profiles are culled and fit from a selected EFIT and ECE, Thompson scattering, and impurity diagnostic data. These are used to generate profile and equilibrium files. OMFIT interfaces with the TORAY-GA framework and can run the code on multiple time steps TORAY-GA has been benchmarked against a range of ray and beam tracing codes[49]. These efforts have found good agreement as to the deposition location, but provide different profile widths. A comparison of beam and ray tracing codes finds good agreement on the deposition center in the plasma, but even in these codes which disregard the degree of fluctuations in the tokamak, there is variation in the drive width predicted.

In experiments using time correlation measurements in ECE by Zerbini *et. al* [50], the ECH deposition center has been found to agree well with experimental modulation measurements. Zerbini found that significant amount

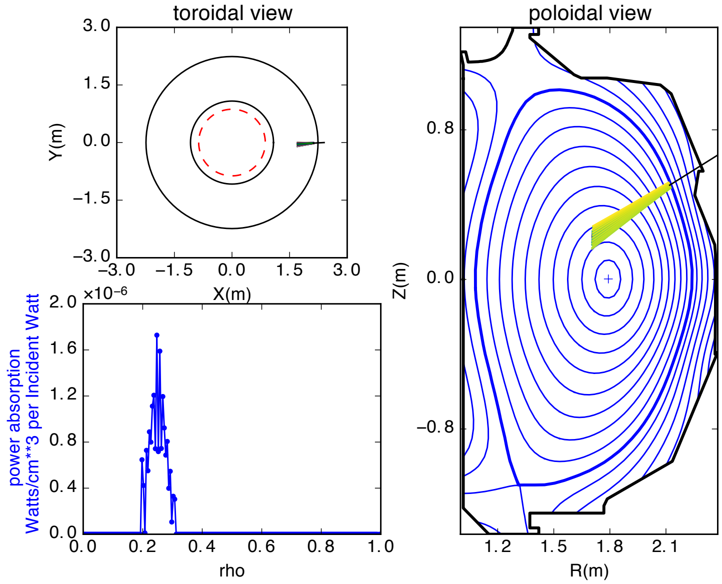

Figure 2.17: Results from a TORAY-GA run performed in the OMFIT framework. An applied 100 ray propagation pattern and absorption location are shown in the poloidal and toroidal cross section. From the absorption calculated along these rays, a 1D power profile can be produced.

of transport obscures the experimental width of deposition. Resolving this transport has been treated in past work has found only a factor of $\mathcal{O}(\times 2)$ consistency in deposition width, and in the intermeaning time, the χ_e diffusivity model has been shown to be completely insufficient to describe transport in ECH heated discharges[51].

Codes such as TORAY-GA, GREY, and CQL-3D [49] are powerful in their ability to resolve kinetic effects and basic ECCD profiles, but they do not treat an interaction between ECH and drift wave turbulence. Assumptions made about the beam waist as it exits the strongly fluctuating edge of the plasma are propagated into the core. This turbulence is discussed briefly in the next section.

Chapter 3

Understanding Turbulent Fluctuations

3.1 Background

Electron cyclotron current drive (ECCD) is used to stabilize the growth of tearing modes in the plasma through local current drive at the island O-point [48]. Past efforts have found agreement in deposition location of the injected microwave beam between experiment[50] and ray tracing code TORAY-GA[52]. However, reconciling experimental and theoretical deposition profile width measurements requires ad-hoc diffusion of current, an effect that was not supported by soft x-ray profile measurements of ECCD on TCV[53]. Based on simulations [54] and analytic work, density fluctuations on the same scale as the injected wavelength produce a scattering of the wave, spreading and deflecting the beam. Edge structures generated by drift wave turbulence move past the beam and turn over quickly $\mathcal{O}(10\text{ kHz})$[55], deflecting the beam about the equilibrium path. Thus the observed effect on the plasma, on both the $\mathcal{O}(100\text{ ms})$ thermal timescales which govern heating, and $\mathcal{O}(1\text{ s})$[15] resistive time scales for current drive) is an effectively broadened heating profile about the TORAY-GA derived deposition center.

Fluctuations can effectively broaden the ECCD profile such that power falls outside of the magnetic islands, where it does not contribute to mode suppression. Increasing requirements for ECCD could impact the gain achievable on ITER[48]. This concern motivates the present effort, centered on the DIII-D tokamak, to produce a validated measure of broadening in a tokamak discharges through measurement of microwave power deposition. This work will introduce a means of transport fitting to recover the deposition profile width, which scales with the measured level of millimeter-scale density fluctuations in the tokamak edge. A scaling of fluctuations is achieved through analyzing multiple confinement modes with a single factor that characterizes the broadening of deposition over that predicted by TORAY-GA[6].

These first experimental results will validate concerns about broadening of RF beams, and form a dataset which can be used to both drive and benchmark simulation efforts. Simulations by Matthew Thomas at the University of York complement the experimental results,[3] measuring a comparable degree of beam broadening. These simulations are discussed in brief in Section 3.5.

3.2 Drift Wave Turbulence Generates Fluctuations

The main concern of this work is the interaction with density variations in plasma on the scale of the electron cyclotron wavelength. A fundamentally electrostatic variation in the plasma drive coherent structures across a range of scales in density, temperature, and magnetic field.

Drift wave turbulence is a consequence of electric fields which arise in the tokamak. As defined in the first section, plasmas consist of charges which act to screen out electric charges. In fact, plasmas are not entirely neutral, rather they are only 'quasineutral' - charge is screened out in plasma response over a finite scale length. Plasma temperature and density play a role in determining the scales over which non-neutralities can exist. This length can be found from the Poisson-Boltzmann equation, reproduced below from Chen[20]:

$$\frac{\delta n_i - \delta n_e}{n_e} = \frac{-k_B T_e}{4\pi e^2} \nabla^2 (\frac{e\theta}{k_B T_e}) \tag{3.1}$$

This equation can be solved for the debye length, $\lambda_D = (\epsilon_0 T_e / 2e^2 n_e)$ over which electric fields can arise. An electron density and temperature control the debye length because lighter electrons respond more quickly to a perturbation than heavier ions. The screening response of the electrons will shield the potential from an arbitrary charge, q, according to the form.

$$V = \frac{q}{4\pi r \epsilon_0} \times exp(-r/\lambda_D) \tag{3.2}$$

In practice, this limits the fractional charge separation, given by Eq. 3.3 to be very small.

$$\frac{\delta n_i - \delta n_e}{N} = \frac{-k_B T_e}{4\pi e^2 N} \nabla^2 (\frac{e\phi}{k_B T_e}) \ll 1 \tag{3.3}$$

hOWEVER, The restoring force responsible for enforcing quasineutrality can give rise to waves in the plasma. The theoretical description below follows mostly from work by Horton[56]. When gradients, either in density or temperature, are substantial, they constitute a source of free energy for structures driven by the restoring force, which are known as drift waves. Electrostatic and magnetostatic structures can grow on top of the 1D equilibrium as perturbations in charge create electric fields.

Small scale perturbations will be significant for their interaction with RF in this work, but structures of variety of scales drive substantial heat and particle fluxes which have frustrated decades of efforts to produce viable fusion reactors, constituting the single greatest source of energy losses in most high performance tokamak discharges. In many cases, these fluxes will be an order of magnitude greater than that predicted by the gyro-Bohm scaling based on collisional diffusion of particles[20]. Ion-gyro scale turbulence is responsible for much of the difficulty in achieving fusion[60]. As in the case of Bohm diffusion, the turbulent diffusion coefficient can be expressed in terms of a scale length and a characteristic time, which vary depending on the form of turbulence under consideration. The ion gyro-radius and sound speed dictate the response of ion scale turbulence. Large ion-driven turbulence structures have characteristic sizes as large as a few centimeter in DIII-D[60] and smaller electron temperate driven streamers drive significant fluxes[57]. In this work, transport coefficients are entirely dominated by their turbulent contributions.

The tokamak edge is the location of the steepest gradients, and this provides a significant source of energy for turbulence across a range of scales. RF scatters off of plasma turbulence in the Tokamak edge. In L-mode, electrostatic, density gradient-driven turbulence drives significant ion scale fluctuations in the plasma edge near the last closed flux surface [55]. H-mode sees a combination of ion and electron driven turbulence as significant, but reduced overall fluctuation. Zonal flows - regions of coherent structures - drive not only transport characteristics [58], but also the H-mode pedestal itself. In this chapter, we will explore turbulence measurements, as well as analytic and simulated representations of turbulence which will be significant to this work.

3.3 Experimental Measurements of Turbulence

Electron density fluctuation measurements for this work are derived from two diagnostics. Doppler backscattering uses phase shift measurements from a backscattered microwave beam[59]. In a continuous plasma, a 74.8 GHz probe beam could propagate smoothly to its resonance without being scattered. However, fluctuations can interact with this beam much as they interact with the high power microwave beam used for EC heating. When these structures are coherent in their size, they produce an interference pattern in backscattered radiation which is related to the scale and motion of the structures. These fluctuations scatter and shift the wavenumber of the injected beam, producing a returned signal which is proportional to the amplitude of the fluctuations. By observing specific wavenumbers of backscattered power, it is possible to probe different regions of the plasma.

DBS comes closest to measuring the appropriate scale for scattering-relevant fluctuations. The wavenumber sensitivity of DBS is $1cm^{-1} \geq k_{\theta}\rho_{s}$.

The scattering response peaks for structures of half the vacuum ECH wavelength ($\approx 1.2mm$) Thus for this work the fluctuation amplitude measured by DBS comes closest to the fluctuational amplitude. No high-k system was available on DIII-D at the time of this work, but the similarity between DBS and ECH scales makes it the best possible proxy. An interferometer system such as MIT's phase contrast imaging (PCI) could in principle make these measurements, but the DIII-D PCI chord is optimized for core measurements, as opposed to the edge measurements needed for this work. Fluctuation measurements from some of the discharges used to derive the scaling of broadening with fluctuations.

For this work, measurements from a set channels corresponding to different locations is time averaged and the measured amplitude in the edge region, at$\rho = .95$, is extracted or linearly extrapolated. A significant radial uncertainty resulting from the wavenumber acceptance range of the dbschannels means that a measurement taken at $\rho = .95$ will in fact reflect fluctuations in a wider range. Uncertainties in some discharges will stretch from $.9 > \rho > 1.05$ - the entire region where the fluctuation interaction is significant

There are advantages to utilizing other turbulence diagnostics in addition to DBS data. The fluctuations measured by DBS map to a 1D set of flux surfaces in the plasma and these channels can have a significant spacing between them - two channels on nearby flux surfaces can be seperated by centimeters. This makes it difficult to derive information about the coherence length of fluctuation structures in plasma. 2D informatation - such as the

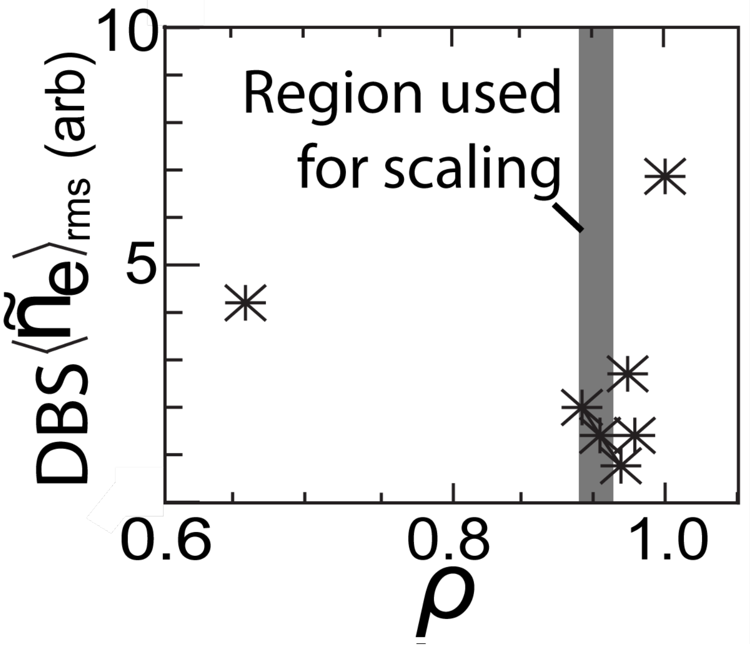

Figure 3.1: Density fluctuation measurements from Doppler backscattering made for a DIII-D H-mode broadening case. The amplitude of the fluctuations at $\rho = .95$ are taken as characterizing the turbulence amplitude. It is in this region where the turbulence drive term - the density gradient - is largest. Radial uncertainties are of the order $\Delta\rho = .05$. Thus the channel value at $\rho = .95$ can be considered an average over the entire steep gradient region.

poloidal correlation length of fluctuations - cannot be derived from DBS. To understand the 2D variation of turbulence - radially and poloidally, DIII-D's beam emission spectroscopy (BES) system is used[60].

An array of optical fibers collect emission generated by one of DIII-D's neutral beams. Shifts in this line emission provide information about ion-scale fluctuations in the plasma. Fibers can be distributed up and down the body of the beam. This extent in Z makes it one of the few diagnostics able to measure poloidal as well as radial variations in fluctuations. By modeling the beam character, based on the known emissivity of the deuterium majority and measured characteristics of the beams - voltage, current, optics - it is possible to achieve measurements of poloidal and radial fluctuation correlation lengths in addition to turbulence amplitude. The correlation length varies with structure size. BES measures a weighted average of the correlation lengths of turbulence within its measured range. Simulations made as part of this scientific effort (see Sec. 3.4.1) find correlation lengths of a significant number of smaller structures are indeed comparable to the ECH wavelength.

3.4 Scattering by Blobs Solved Analytically

Some of the first predictions of the effects of fluctations come from analytic theory. This work summarizes the consequences of papers by Ram[62] and Kyriakos[1], rather than reproduce them in full here. Analytic theory enables treating of density fluctuation structures as a polarizable mass, similar to a dielectric. 'Blobs' are density structures which occur in the scrape-off

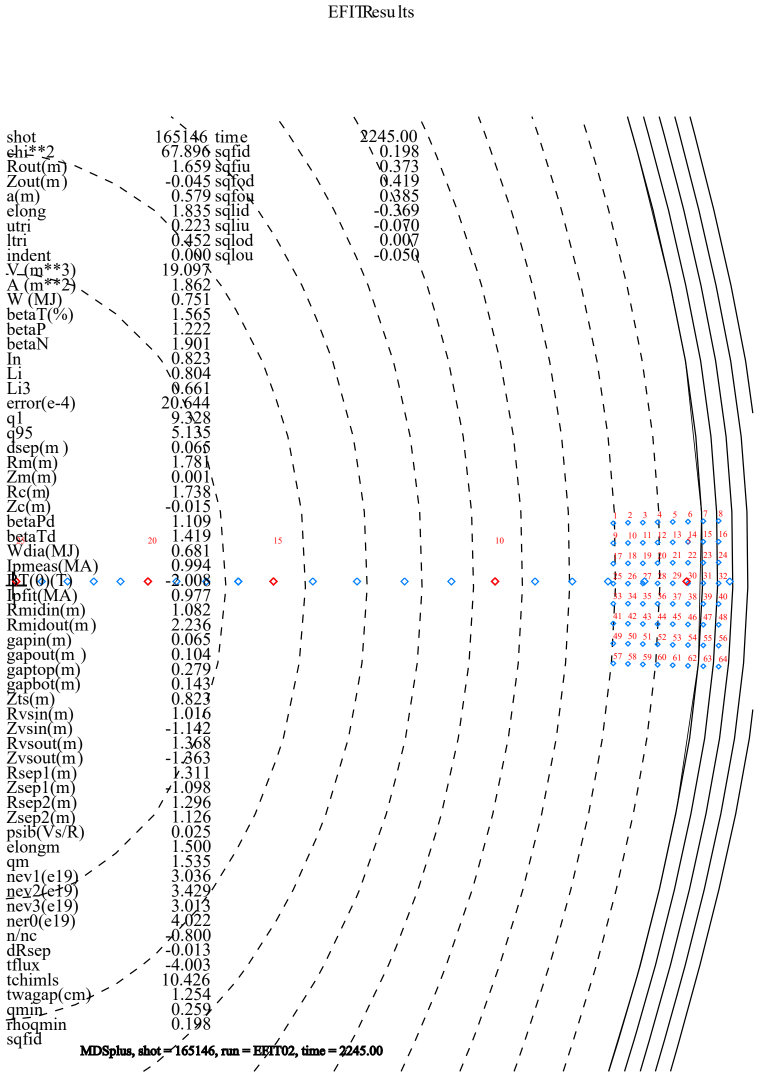

shot	165146	time	2245.00
chi**2	67.896	sqfid	0.198
Rout(m)	1.659	sqfiu	0.373
Zout(m)	-0.045	sqfod	0.419
a(m)	0.579	sqfou	0.385
elong	1.835	sqlid	-0.369
utri	0.223	sqliu	-0.070
ltri	0.452	sqlod	0.007
indent	0.000	sqlou	-0.050
V (m**3)	19.097		
A (m**2)	1.862		
W (MJ)	0.751		
betaT(%)	1.565		
betaP	1.222		
betaN	1.901		
In	0.823		
Li	0.804		
Li3	0.661		
error(e-4)	20.644		
q1	9.328		
q95	5.135		
dsep(m)	0.065		
Rm(m)	1.781		
Zm(m)	0.001		
Rc(m)	1.738		
Zc(m)	-0.015		
betaPd	1.109		
betaTd	1.419		
Wdia(MJ)	0.681		
Ipmeas(MA)	0.994		
BT(0)(T)	-2.008		
Ipfit(MA)	0.977		
Rmidin(m)	1.082		
Rmidout(m)	2.236		
gapin(m)	0.065		
gapout(m)	0.104		
gaptop(m)	0.279		
gapbot(m)	0.143		
Zts(m)	0.823		
Rvsin(m)	1.016		
Zvsin(m)	-1.142		
Rvsout(m)	1.368		
Zvsout(m)	-1.363		
Rsep1(m)	1.311		
Zsep1(m)	-1.098		
Rsep2(m)	1.296		
Zsep2(m)	1.126		
psib(Vs/R)	0.025		
elongm	1.500		
qm	1.535		
nev1(e19)	3.036		
nev2(e19)	3.429		
nev3(e19)	3.013		
ner0(e19)	4.022		
n/nc	-0.800		
dRsep	-0.013		
tflux	-4.003		
tchimls	10.426		
twagap(cm)	1.254		
qmin	0.259		
rhoqmin	0.198		
sqfid			

Figure 3.2: Position of the BES channels on the low field side edge are shown. Behind it run the 40 ECE channels, displayed for reference. The base 8X8 array of optics is arrayed along the the path of a neutral beam to measure spectroscopically the emission of deuterium. The array can optionally be extended with a midplane channel by switching some fibers.

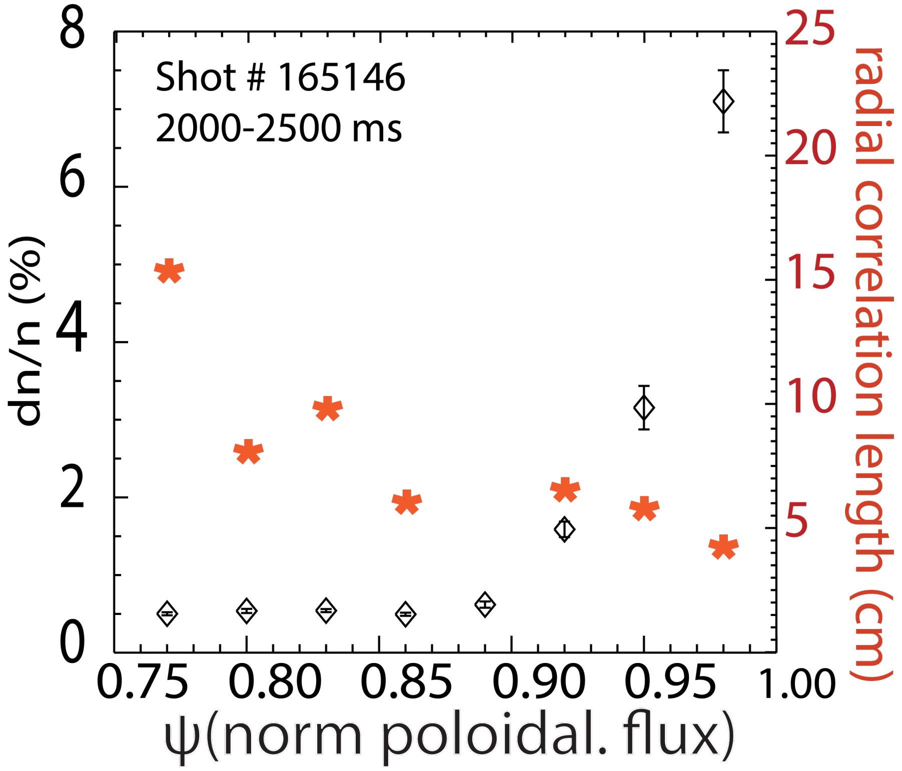

Figure 3.3: Density fluctuation measurements from beam emission spectroscopy made for a DIII-D H-mode broadening case. These larger scale fluctuations inform Simulations made to understand the poloidal structure and correlation length of fluctuations. Because BES measures larger scale structures, it produces a lower fractional amplitude than is generally found for smaller scale structures[61].

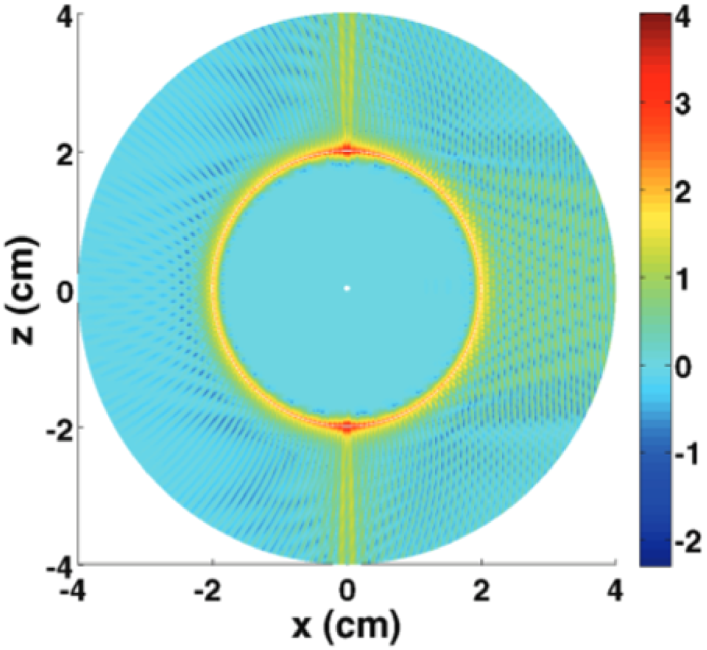

Figure 3.4: An analytic blob, with twice the background density, experiences in an incident plane wave from the left. This problem is a tractable analytic analogy for what happens when microwaves interact with filaments.(Figure C.O. Abhay Ram)

layer of plasmas. As, opposed to filaments, which are extended along field lines inside and outside the scrape off layer, blobs are density structures which have been ejected from the plasma, and they have spherical character.

In the work of Ram, an analytic blob is imposed in a homogeneous background. It experiences an incident microwave plane wave. The incident wave polarizes the blob, altering the dielectric permissivity. Matching of the boundary conditions of Maxwell's equations produces both polarization and wavenumber scattering. This work leaves a full analytic treatment to the literature[62], but this analysis is significant in that it provides a theoretical underpinning for scattering by density structures. The scattering caused by filaments goes well beyond simple defraction effects, requiring treatment of the full electric and magnetic fields associated with propagation.The similarity between structure size and wavelength also clearly violates the WKB approximation which underlies geometric optics.

The tokamak edge is 100 ECH vacuum wavelengths long. A propagating wave will encounter a number of structures over this distance, perhaps undergoing multiple scatterings. Solving such problems in any practical sense requires combining a treatment of Maxwell's equations with a realistic model of turbulent structures. As part of this work, profile data was used to drive a set of simulations which retain the full Maxwell's equations together with density and magnetic field variation. By using modeled turbulence generated self consistently from plasma profiles, and benchmarked against experimental measurements, simulations can treat scenarios comparable to the tokamak edge.

3.4.1 HERMES model simulations of Edge Turbulence

This section discusses the Hermes model, following from the 2017 papers by M.W. Brookman and M. B. Thomas. The turbulence used for simulating microwave interaction was generated using the BOUT++ framework [63]. The Hermes model [55] was simplified to include only electrostatic effects in a quasi-3D geometry. In the perpendicular plane the fluid equations were modeled explicitly, while separate closures were used for the parallel direction to simulate the behavior inside and outside the separatrix. The Hasegawa-Wakatani [64] closure (written as as an electric potential in Eq. 3.4) describes the closed field line region, which models nearly adiabatic electrons through a parallel current and resistivity. The Hasagawa-Wakatani modes the evolution of an electrostatic potential is a result of charge separation in the tokamak.

$$\frac{\partial}{\partial t}\left(\nabla^2\phi - \phi\right) - \left[(\nabla\phi \times \hat{z}) \cdot \nabla\right]\left(\nabla^2\phi - ln\frac{n_0}{\omega_{ci}}\right) \tag{3.4}$$

Debye shielding can be expanded into an approximation. which is a function of density and ion electron cyclotron frequencies (as the ion scale is the larger of the two). Outside the separatrix, a sheath model provides a sink for plasma density and energy[65]. Experimentally measured L-mode density and temperature profiles from DIII-D shot 165078 provided a drive for the plasma turbulence, which was simulated as a quasi-3D slab of plasma at the mid-plane. The resulting turbulence is described by a radial (flux coordinate) and binormal correlation lengths, $\lambda_\psi = 3$mm and $\lambda_\perp = 9$mm respectively which is consistent with experimental measurements in the edge [60, 61]. The correlation length is defined as the average distance over which the normalized autocorrelation falls off to a value of 1/e which corresponds to the eddy radius. The resulting time averaged radial RMS fluctuation level profile of the generated turbulence is shown in Fig. 3.5 and is also consistent with experimental measurements [60][61][66] made on DIII-D.

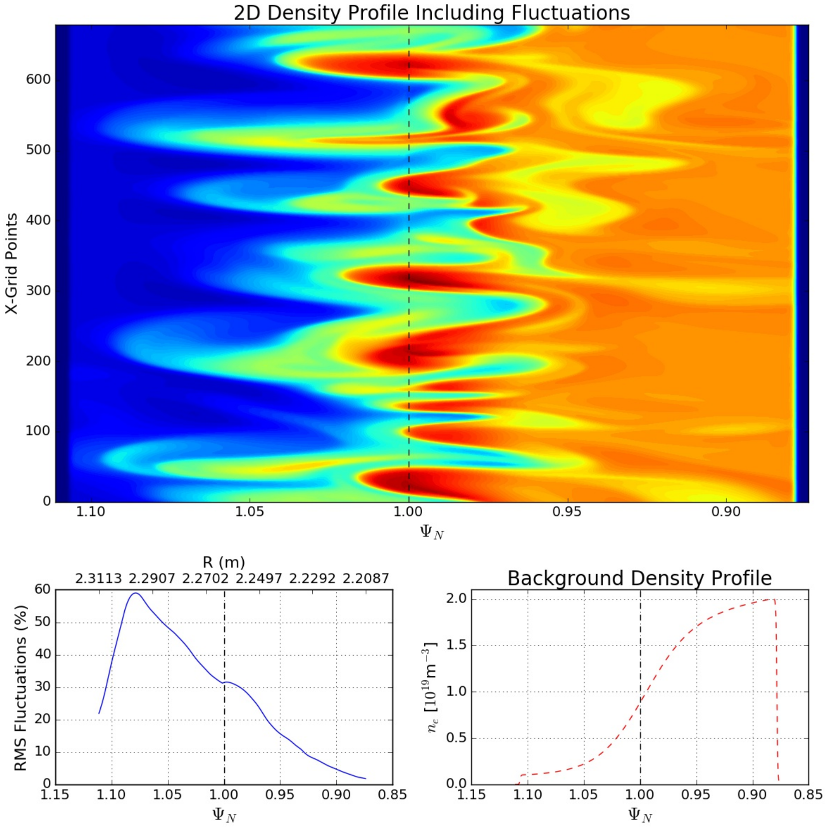

Figure 3.5: The top image shows the 2D density profile as a function of normalized psi ($\psi_N =$) for a single turbulence snapshot. The bottom right image shows the background density profile on which the fluctuations lay. The bottom left image shows the fluctuation level profile for the time averaged ensemble of 172 snapshots overlaid with major radius R. The dashed black line represents the seperatrix in all plots.

These simulations focus on the edge region, examining a slab which runs from ψ=.85 to 1.15. Scattering will be seen to be mostly significant in the steep gradient region, $\psi = 9.5 - 1.05$, but simulations are performed in a wider region to allow for a falloff of scattering amplitude.

3.5 3D Full Wave Simulations of RF Propagation Through Turbulence

A 3D full-wave cold plasma finite difference time domain code EMIT-3D [67] has been used to simulate the extent to which scattering broadens a microwave beam in DIII-D. A full wave treatment is necessary when the inhomogeneity scale length is comparable to the wavelength [2]. This occurs in the steep density gradient region of the plasma edge where the turbulence RMS fluctuation level is large (up to 70%) and the correlation length is most comparable to the wavelength. Due to the large computational demands of a full wave code it is therefore only necessary to model the plasma edge.

The simulated domain as shown in Fig 3.5 defines a distance of $40\lambda_0$ ($\lambda_0 = 2.7$mm) radially through the plasma edge. The beam is launched as X-mode with a width defined as the value to which the intensity falls to $1/e^2$, is $6.8\lambda_0$ (waist radius $w0 = 3.4\lambda_0$) thus ensuring a plane wave front to match experiment. The magnetic field is assumed constant 1.5 T over the simulation domain. The beam is launched perpendicular to the magnetic field vector and density filamentary structures. Due to the separation in time scales, each simulation propagates a wave through a still snapshot of the turbulence profile. The time averaged effect of scattering due to plasma turbulence is to sweep out an area resulting in a new Gaussian profile with an increased width. An ensemble average of the RMS power at the back plane for 172 simulations provides a natural method for measuring the average beam width after propagating through the turbulent layer. This average beam width is then compared with the RMS power from a simulation containing the density profile with no fluctuations (see figure 3.6).

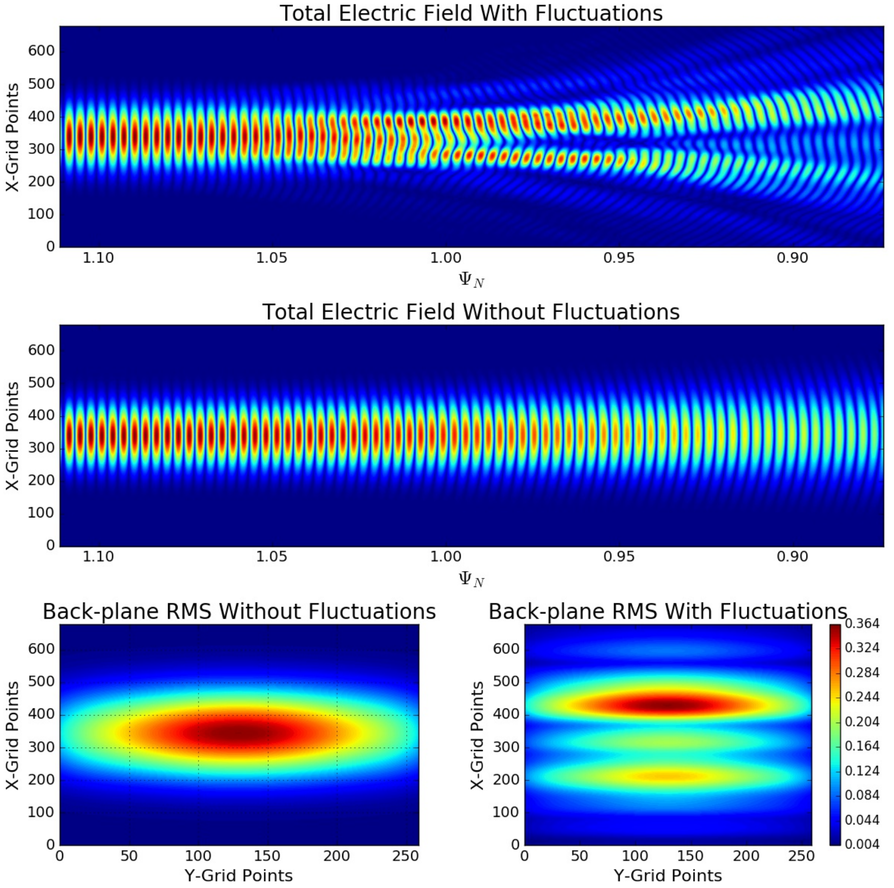

Figure 3.6: Full wave propegation results for the 2D HERMES fluctuations based on real DIII-D experiments. The top image shows the Total electric field of a wave propagating through the snapshot shown in figure 3.5. The resulting RMS electric field for this simulation at the back plane is shown in the bottom right. The middle image shows the total electric field for a wave propagating through the background density profile as in figure 3.5. The resulting RMS electric field for this simulation at the back plane is shown in the bottom right.

It was found that the resulting beam broadening due to scattering by density fluctuations over the simulation domain was 1.94 times that of a beam propagating over the same profile without fluctuations. The deposition location is a further $100\lambda_0$ into the plasma ($\psi_N = 0.11$), so the broadening is expected to be larger. What follows is an estimation of the beam broadening at the absorption point by extrapolating the beam RMS electric field profile from the simulation domain to the absorption point. The extrapolation is done for both the non-scattered beam and the ensemble averaged scattered beam which approximates as a Gaussian. A beam divergence angle is found by relating the beam width at the back plane to that at the antenna. This divergence is then assumed constant and a linear fit is applied to the divergence of the beam as shown in figure 3.7 as the beam is projected forward from the back plane to the absorption point. EMIT-3D has therefore calculated the scattering physics leading to the ratio of the beam widths over the scattering region. This ratio is then simply projected further into the distance assuming no further scattering takes place and that the difference in beam widths is purely due to scattering in the edge simulated domain.

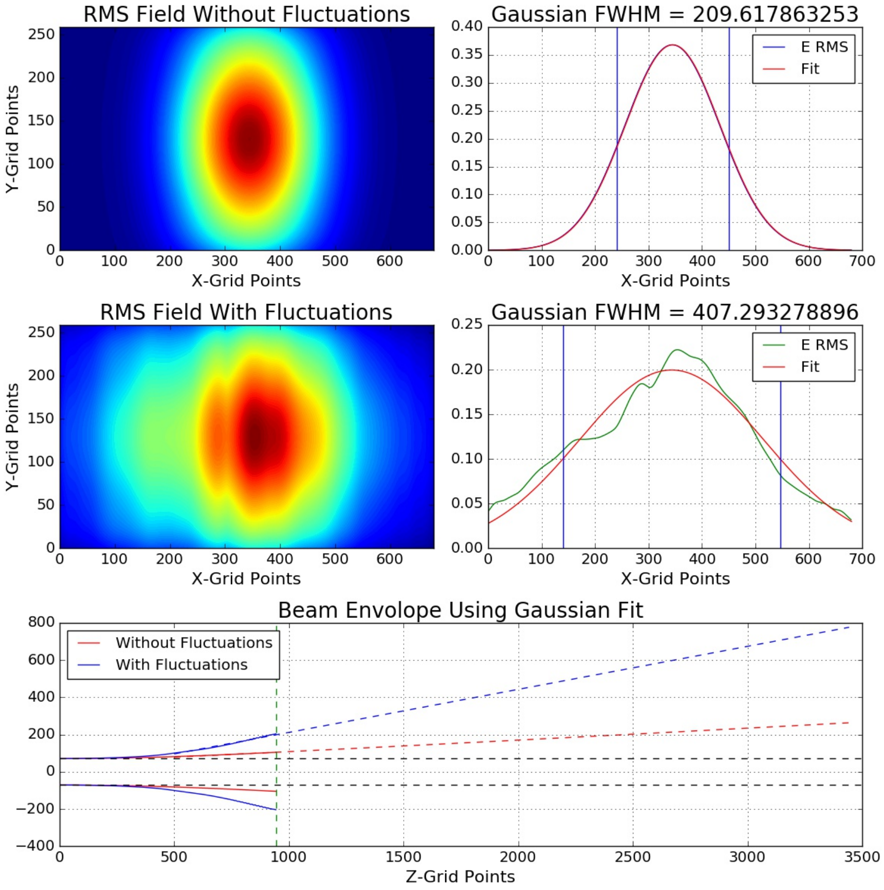

Figure 3.7: The top two figures on the left are 2D images of the RMS electric field at the backplane as defined by the dashed green line in the bottom figure. The top two figures on the right are their respective 1D out put at a Y-grid point of 135 through their centre. The bottom image shows the beam envelope after a Gaussian has been fit to the RMS electric field along the path of propagation. The extrapolation in the forward direction shown by the dashed lines is a further 2.5 times the simulation domain.

The estimated beam broadening due to fluctuations when extrapolated to the absorption point is 2.8 - 3.2 depending on the fit used which is in excellent agreement with the experimental value of 2.7 given the basic extrapolation technique and the small sample size. It must be noted that the extrapolation must be used as an indication only given the large uncertainties and future work would ideally use the output from EMIT-3D as input to a beam tracer to propagate the distance to the absorption layer. The reader is referred to the excellent paper by Thomas[3] for more simulated cases.

Chapter 4

Using Heat Transport to Resolve Microwave Deposition

4.1 Perturbative Deposition Measurements

Measurement of microwave heat deposition[1] in tokamaks is complicated by transport[50]. It is well known that application of auxiliary heating leads to a degradation of plasma confinement[68]. As the plasma is heated, temperature and density gradients increase, driving an enhanced level of transport in the plasma. The timescales associated with increased heat transport are short. The thermal confinement time on DIII-D is of the order of 100 ms, but the flux surface equilibration time is less than 1 ms[15], so the 1D equilibration of the plasma to a new source of energy is rapid. Increased transport with heating means that additional power does not produce a commensurate change in the stored energy. Shown in Figure 4.1, an increase of 20% in input power in the form an additional 1 MW of ECH power, added to 6.5 MW of power from neutral beams perturbs profiles modestly, and does not increase

---

[1] Work in this chapter has been submitted for publication in Nuclear Fusion as *Resolving ECRH deposition broadening due to edge turbulence in DIII-D by heat deposition measurement.* by Michael W Brookman, Matthew B Thomas, Jarrod Leddy, C Craig Petty, Robert J La Haye, K Barada, Terry L Rhodes, Zheng Yan, Max E Austin, Roddy G L Vann, which details the power deposition analysis developed by Brookman and detailed in the next section.`https://arxiv.org/abs/1710.03503`

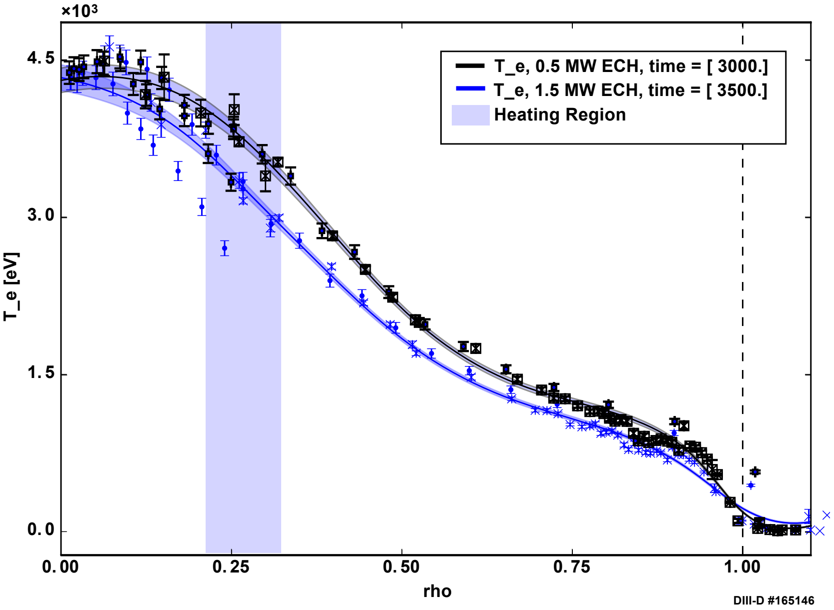

Figure 4.1: The electron temperature in a discharge where injected gyrotron is stepped down from 1.5 MW to .5 MW. Core temperature is not altered, but there is a modest increase in stored energy in the profile.

the core temperature.

When power is modulated, heat transport evolves quickly enough to change in tokamak parameters[26]. Added to this, diffusion and convection cannot be separated in steady state[68]. To separate enhanced transport from a broadened profile width, modulated transport coefficients must be quantified and separated from inherent broadening of the RF beam. This effort is based on a method of fitting the consistency between power transport and energy conservation. Generating a perturbation in the plasma through ECH modulation (fig: 4.2) allows for the deposition profile to be determined. In this chapter, a method of transport fitting based on a heat flux technique [69]

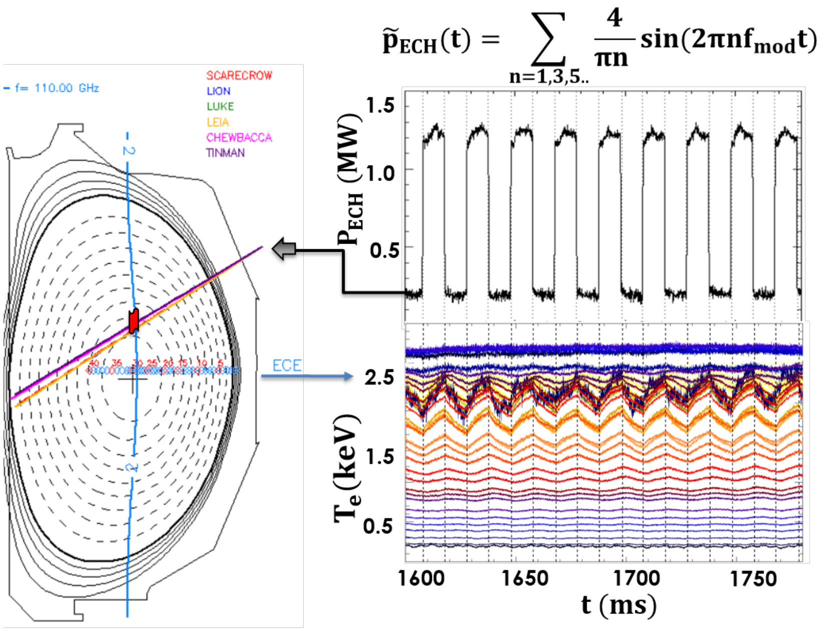

Figure 4.2: This diagram describes the modulation process used to generate perturbative transport measurements. Because the transport coefficients D and V cannot be separated in equilibrium, a perturbation must be generated in the plasma. Through application of a square wave modulation with ECH, a 1D heat perturbation is generated. The same harmonics that appear in the power modulation appear in the temperature modulation. Electron temperature measurements from the 48 channel ECE system are used to quantify this heat perturbation. Here $f_m od$=50 Hz.

with transport fitting across the modulation frequencies is introduced.

4.2 Perturbative Deposition Analysis

In the absence of transport effects, the change in electron stored energy could be calculated as a function of density n_e, and temperature T_e at the switch-on of ECH power[50]. Stored energy would change with input power, and perturbation measurements would then directly provide the power deposition as a function of radius.

$$3/2n_e\frac{\partial T_e(\rho,t)}{\partial t}\approx p_{ECH}(\rho,t) \tag{4.1}$$

The perturbation from microwave heating on DIII-D is resolved by measurements of electron temperature (T_e). 2nd harmonic X-mode ECE coverage at the applied toroidal field of $B_t = 2$T extends inwards from the optically thin scrape off layer at $\rho = 1$, where ρ is a radial coordinate normalized to square root of toroidal flux (coordinates are defined in Section 1.4.1). Fourier analysis produces temperature perturbation profile (modulated quantities are expressed with a tilde, for example $\tilde{T_e}$) which is compared with the ray tracing derived deposition profile in Figure 4.6. Experimental perturbation profiles are always wider than TORAY-GA calculated deposition due to heat transport, ash shown in Fig. 4.3.

This is because heat perturbations leads to a prompt change in the flow of energy, such that $\partial T_e/\partial t \neq dT_e/dt$, a change to the electron heat flux Q_e which obscures the base deposition profile. This chapter will discuss how, through perturbative heating experiments, the inherent deposition width can be seperated from this transport.

4.2.1 The Heat Equation

The 1D heat equation[70] is the basis for resolving power deposition broadening from heat transport. Heat deposition and edge density fluctua-

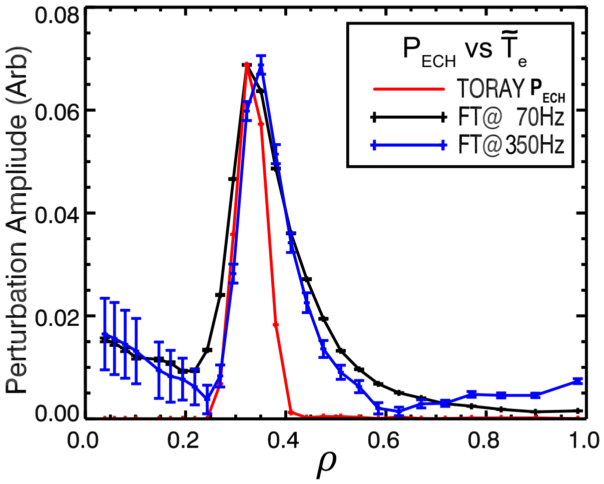

Figure 4.3: Normalized electron temperature perturbation profile produced, with uncertainties, by a least-squares Fourier Analysis. 1st (black) and 5th (blue) harmonics of the modulation frequency are shown. These are both wider than the $P_{ECH}(r)$ source function predicted by the TORAY-GA ray tracing code [49].

tions have a significant 2D character[71]. However, transport of heat along a flux surface is much faster than transport across surfaces. Equilibration times for T_e along a flux surface are $\approx 10\mu s$[15]. This is 100 times less than the heat confinement timescale which is of the order of 1 ms. Thus modulation of ECH at a modest frequency, here $70 \geq f_{MOD} \geq 27$ Hz, creates a 1D temperature perturbation which can be treated through energy conservation. To do this, we'll first start by considering the full 1D heat equation of Gentle[70], which is written as Eq. 4.2. This expression is simply a statement of energy conservation - sources and sinks of energy must be balanced by flows in the plasma.

$$\frac{d}{dt}\left(\frac{3}{2}n_eT_e\right) - Q_e = P_{ECH} + P_{NBI} + P_{OHM} + P_{OTHER} \tag{4.2}$$

Here, n_e is the electron density, T_e is the electron temperature, Q_e is the electron heat flux. Terms on the right are power sources from electron cyclotron heating (ECH), neutral beam injection (NBI), Ohmic power (OHM), and radiated power, which do not vary significantly over the modulation cycle. (These are captured by a fitting constant in the following chapters).

Through detrending and linearization, this equation can be used to resolve the deposition width $P_{ECH}(r)$. This power modulation can be analyzed with any number of assumptions about transport.

4.2.2 Break-in-Slope Analysis

The most basic means of measuring power deposition is to watch for the prompt change in plasma stored energy as power is switched on. Any change in transport must be causal, as changes in the plasma itself drive the change flow of heat. The ECH heats the bulk electrons[37] and is not a particle source. Heating therefore drives an immediate change in electron temperature, with the power being equal to the local change in stored energy. Break-in-slope fitting uses a simple assumption - that the heat flux electron Q_e evolves like a simple exponential, as shown in Fig. 4.3.

$$p_{ECH}(r) \approx \frac{\partial}{\partial t} 3/2 n_e T_e(r,t) - \nabla \cdot Q_e \tag{4.3}$$

As discussed in the previous chapter, ECE T_e measurements have a 5% error, which is compounded by taking of derivative. The change in energy is the time derivative of the plasma, obscured by some transport effects which in principle take time to develop. Older works [37] used an approximation to characterize the transport. They assumed that the transport induced by the modulation was approximately constant. When Q_e is independent of time, the solution of the differential Equation 4.3 is an exponential saturation response.

By fitting the temperature perturbation $\tilde{T}_e$ with an exponential, tracing it back to the local maximum of the data, the time derivative of the temperature, and thus the power deposition profile is fit. Fig. 4.4 shows an example of these fits - made at turn-on and turn-off for a square wave ECH-modulation. The observed perturbation is described well by an exponential for some cases on DIII-D, such as this. This method provides a decent resolution of the approximate deposition region, but uncertainties are substantial.

Fitting such a simple form to the heat flux discards a considerable amount of time information. The uncertainty and variation in the peak position results in substantial error bars. Transport is also significantly more complex than can be captured by a simple fit exponential. In practice, simulation codes are used to provide an immediate post-shot deposition profile, as

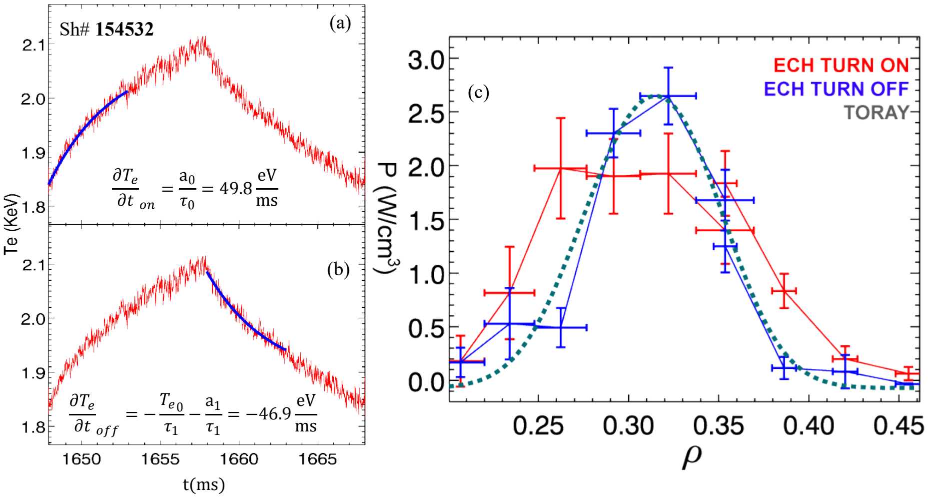

Figure 4.4: Fig:(a) the response of an ECE channel in the deposition region fit during the 'ON' phase of ECH modulation. (b) same channel fit during 'OFF phase' (c) The fit derivative profile at turn on and turn off are averaged over 20 modulation periods, as compared with the TORAY ray tracing profile. Uncertainties for the BIS method are significant.

well as a predictive capability, with experimental measurements serving as a check on these codes. Rather than optimizing for fitting simplicity, this work explores a method of multivariate fitting based on the use of Fourier analysis to resolve time derivatives by treating the full complexity of the heat flux.

4.2.3 Fourier Analysis of Microwave Heat Perturbations

A robust analysis of microwave deposition profile width will require considerably more information than fitting with a simple exponential can provide. Regular modulation allows perturbations and fluxes to be treated in a Fourier basis instead. A set of Fourier harmonics replace the time domain heat flux equation. In a linear transport model a square wave modulation produces a temperature perturbation with the same harmonic content, allowing for frequency-domain analysis of the heat flux. A square wave with a frequency f_{mod} and amplitude P_0 is defined by the harmonic equation:

$$P_{ECH}(t) = P_0 \frac{4}{\pi} \sum_{n=0}^{\infty} \frac{sin(2\pi(2n-1) f_{mod} t)}{2n-1} \tag{4.4}$$

Applying a Fourier transform to the calculated ECH input power allows for a comparison of the gyrotron square wave with the ideal formulation. Figure 4.5 shows the amplitude and phase information from transforming the input gyrotrons used in L-mode discharge 154532.

This frequency dependence will be used together with the power profiles based on broadened TORAY-GA deposition to produce the full profile

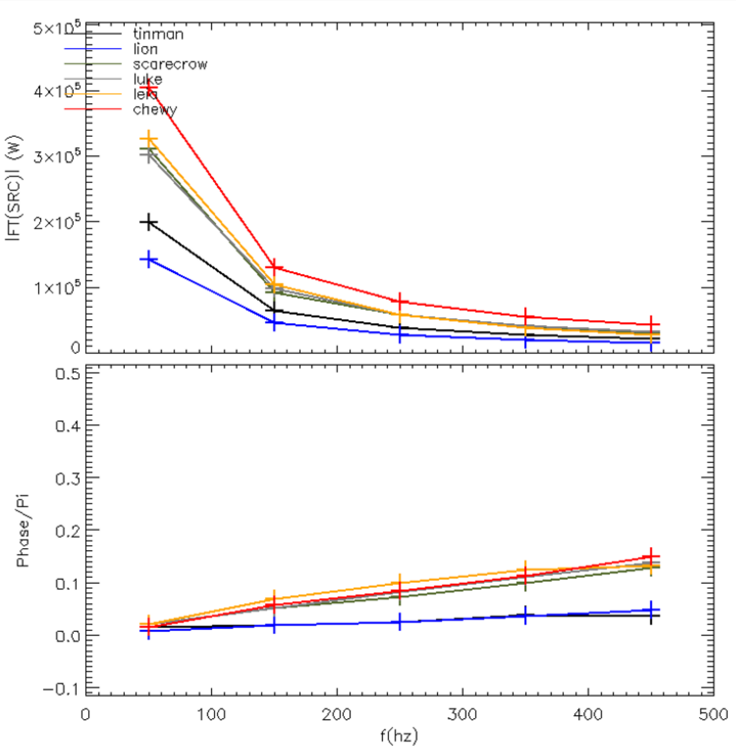

Figure 4.5: The Fourier transform (in the $n * f_{mod}$ basis) of the ECH input power for 6 DIII-D gyrotrons. These were commanded to produce an ideal square wave with f_{mod}=50 Hz. The falloff of power with frequency follows the expected $1/n$ form of the ideal square wave, but phasing differences reflect the practical difficulty of producing an instantaneous switching of power.

$\tilde{p}_{ECH}(r,t)$. In this work, modulated quantities are expressed with a tilde, for example $\tilde{T}_e$ for the temperature perturbation.

Fourier analysis is useful for resolving the temperature perturbation. The 48 channel absolutely calibrated radiometer discussed in Section 2.3 provides a 1D T_e profile digitized at 500 kHz[31]. 2nd harmonic X-mode ECE coverage at $B_t = 2$T in DIII-D extends inwards from the optically thin scrape off layer at $\rho = 1$, where ρ is a radial coordinate normalized to square root of toroidal flux. An advantage of Fourier analysis of ECE data comes from the derivative identity under the transform. For a function f(t), transformed into a frequency basis f, this is expressed by Eq. 4.5.

$$\mathfrak{FT}(\frac{df(t)}{dt})[f] = 2\pi * f \tag{4.5}$$

The Fourier transform, $\mathfrak{FT}$, of the time derivative of some quantity is a factor in frequency times that quantity. Therefore, Fourier analysis of the 2nd harmonic ECE T_e data produces the temperate perturbation and its time derivative directly. This analysis retains significantly more information than the exponential fit used for break-in-slope calculations. Modulated quantities with their baseline values subtracted are expressed with a tilde in this work. The modulated electron temperature profile, $\tilde{T}_e$ is compared with the TORAY-GA deposition profile in Figure 4.6.

Transport always leads to a significant broadening of the $\tilde{T}_e(r,f)$ profiles over $\tilde{p}_{ECH}(r,f)$, even up to the highest measured harmonic.

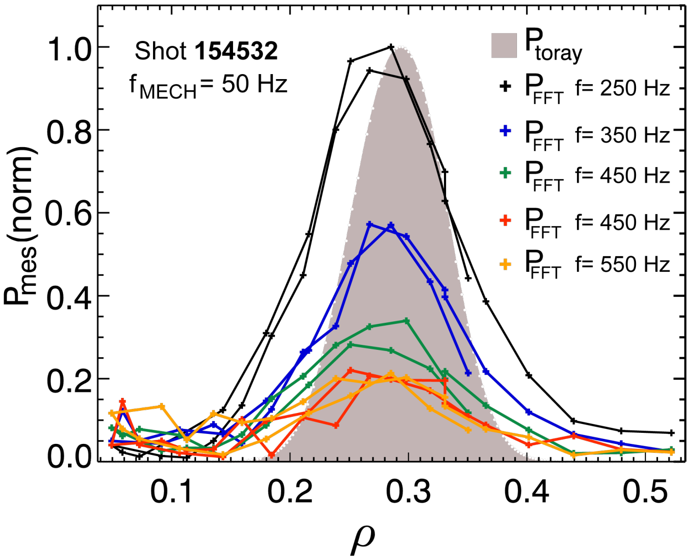

Figure 4.6: Harmonics of the modulated heating are measured by the absolutely calibrated electron cyclotron emission diagnostic. Faster harmonics reflect higher timescale behavior, but fail to converge on the microwave heat deposition predicted by TORAY-GA ray tracing is shown in grey. Transport accounts for some, but not all of this difference. Fitting multiple harmonics simultaneously is needed to separate transport broadening from fluctuation effects.

4.2.4 Fourier Analysis by Matrix Inversion

This section discusses the mathematical form of the least-squares fit Fourier Analysis method used in this work, which has been found to produce significantly lower uncertainties than an FFT which does not directly utilize the known f_{mod}. Fourier analyzed temperatures profiles in this work are constructed through use of a matrix fitting method. Through application of a detrending polynomial (Shown in Fig. 4.2.4), the modulation is separated from variations in the background $\langle T_e \rangle$.

By inverting an unknown coefficient matrix from a Fourier basis acting on a measured signal, it is possible to decompose the signal into Fourier components. The basic matrix equation, Eq. 4.6, consists of two vectors S, a measured signal from a single channel, and C an initially unknown vector of Fourier coefficients.

$$S = \mathbf{M}C \tag{4.6}$$

M is a matrix representation of the components of a Fourier basis, $cos(n\omega t)$ and $sin(n\omega t)$. An arbitrary base frequency ω can be chosen. Choices need not be constrained to match the spacing of the timebase of S. The rows of the matrix represent the real and imaginary (cos and sin) components at each harmonic $n \times \omega$, and the columns are evaluation of these sin and cos harmonic functions at the same time point as used to define the input signal.

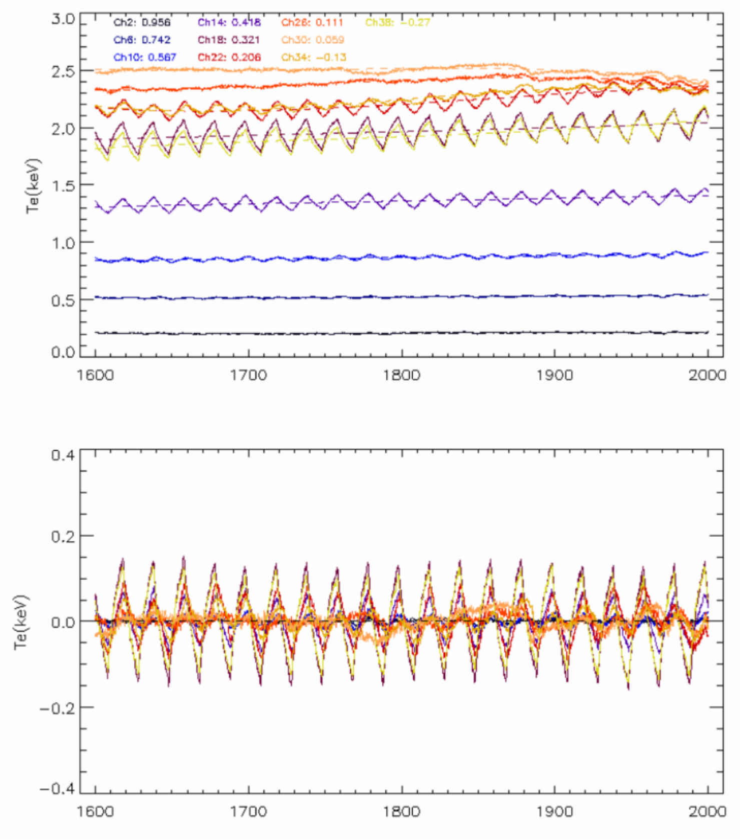

Figure 4.7: Detrended, $f_{mod} = 50Hz$ T_e data is displayed vs time. Use of a polynomial fit can remove secular variations in the background plasma from interfering with Fourier analysis. This L-mode discharge has a modest variation in baseline which is removed with a 5th order polynomial. So long as the order of polynomial is small compared with the number of modulation cycles, the detrending does not follow the modulation, but rather a moving average of the data.

The matrix is illustrated in Eq. 4.7

$$\mathbf{M} = \begin{bmatrix} cos\omega t_0 & sin\omega t_0 & ... & ... & ... \\ cos\omega t_1 & sin\omega t_1 & cos2\omega t_1 & sin2\omega t_1 & ... \\ cos\omega t_2 & ... & ... & ... & ... \\ ... & ... & ... & ... & ... \end{bmatrix} \tag{4.7}$$

A Fourier basis of arbitrary size can be chosen. The matrix M(f,t) does not have to be square. These experiments on DIII-D find that modulation with available ECH power produces a noise-level signal above about the 19th harmonic for 50 Hz modulation. Thus for this analysis, the Fourier basis is limited to 30 harmonics - sufficient to insure reasonable error bars. The time dimension of the Matrix is the same size as the data array, of order 250,000 for these discharges. After selecting a matrix, M(t,f), Eq. 4.6 can be solved for coefficients C(f) such that $\mathbf{M}C$ reproduces S(t).

$$S = \mathbf{M}C \Rightarrow \mathbf{M}^T S = \mathbf{M}^T \mathbf{M}C \Rightarrow (M^T M)^{-1} M^T S = C \tag{4.8}$$

Advances in matrix computing mean this equation can be solved for 30 frequencies and 100,000 data points in about 10 seconds. C is then a matrix of coefficients, such that

$$S \approx S_{fit} = C_0 cos\omega t + C_1 sin\omega t + C_2 cos2\omega t + ... \tag{4.9}$$

For signals on an arbitrary time base, and for time bases which are not commensurate with the modulation, this analysis method proves superior to the basic FFT. The result of this analysis is a real and imaginary set of coefficients defining the Fourier basis, whose uncertainties are well defined according to Eq. 4.10

$$\sigma_S^2 = \frac{(S - S_{fit})^T (S - S_{fit})}{n_{pts}} \tag{4.10}$$

Taking a spline and propagating the error in the radial derivative is then possible, producing a set of perturbation terms (shown in Fig. 4.8)

4.2.5 Fluctuation and Density Profiles Unchanged by Fast Modulation

An obvious questions follows when one modulates the electron temperature with gyrotron power. How much do the other plasma quantities change? Do they change enough to impact the validity of a strictly temperature-based model? Observing the results of density profile and core turbulence diagnostics suggests that they do not.

Electron Density, fluctuation amplitude, and rotation are all known to change with the application of ECH power. Studies with ECH heating have tied it to reductions in plasma density and rotation[72]. This is thought to be due to the evolution of trapped electron modes and related turbulence. Changes in turbulence with electron heating have been found to lead to changes in profiles of density and rotation. Particle flux driven by ECH is known as 'density pump out', and this effect can be so substantial that ECH can be used as a control on plasma density[5]. Changes in turbulence with modulation take a certain time to evolve, as changes in temperature with power modulation

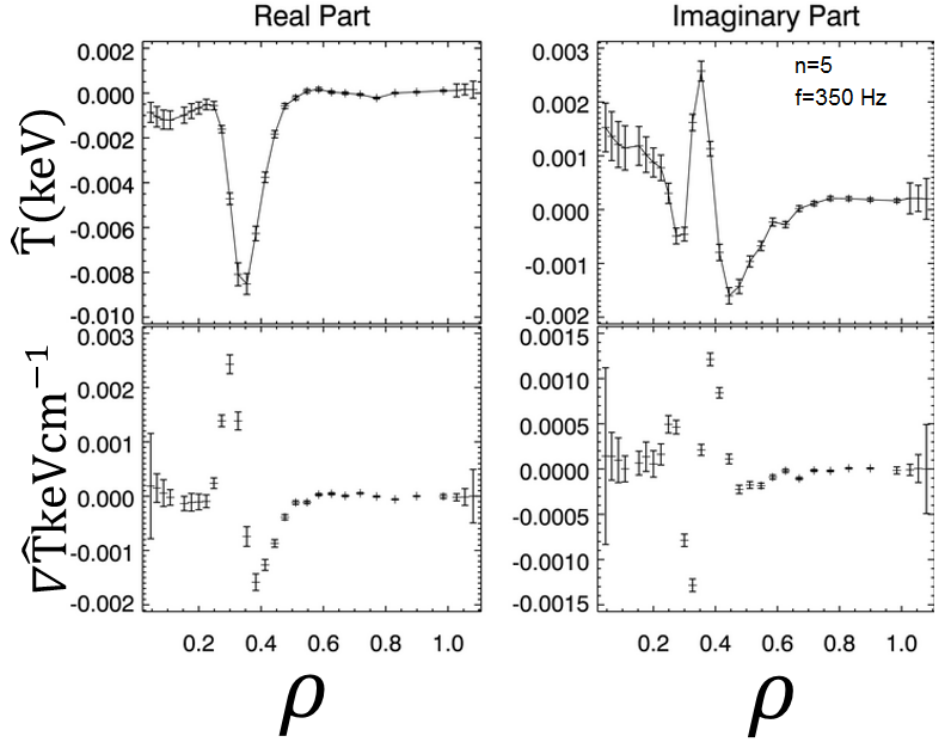

Figure 4.8: The temperature and gradient perturbation generated through this matrix analysis method. Real and complex errors are significantly smaller than those of the break-in-slope profiles or even those produced by FFT. Just the 350 Hz, n=5 harmonic of the 30 used to form a complete basis for the modulation is shown. In practice, modulation frequencies above 2kHz cannot be resolved in ECE data.

drive a transition. Turbulent evolution takes hundreds of milliseconds to produce a clear change in profiles density and rotiation profiles.

Given the timescales involved in turbulent evolution, for modulation frequencies above 10 Hz, the effect of modulated ECH is minimal. The plasma comes to equilibrium with the mean ECH power, and other parameters do not evolve significantly during modulation. This can be seen when comparing the on-off difference between diagnostics.

Correlation ECE[73] uses coupled channels in close proximity to measure the levels of microwave scale electron temperature turbulence. Figure 4.9 shows the amplitude of the fluctuations measured directly in the deposition region of a DIII-D discharge during 70 Hz modulation, as compared with the total gyrotron power.

,

The absence of turbulence modulation coincides with a very minimal change in density, well below the 2% uncertainty of the DIII-D Thompson system for any given modulation cycle. A coherent averaging technique based on data from the DIII-D interferometer[74], which observes a line-average density looking coreward from the midplane, can be used to reduce uncertainties. In the most extreme cases, this analysis finds a change of 0.5% over the modulation cycle, as indicated in Figure 4.10.

,

Fast modulation avoids changes in parameters other than heat trans-

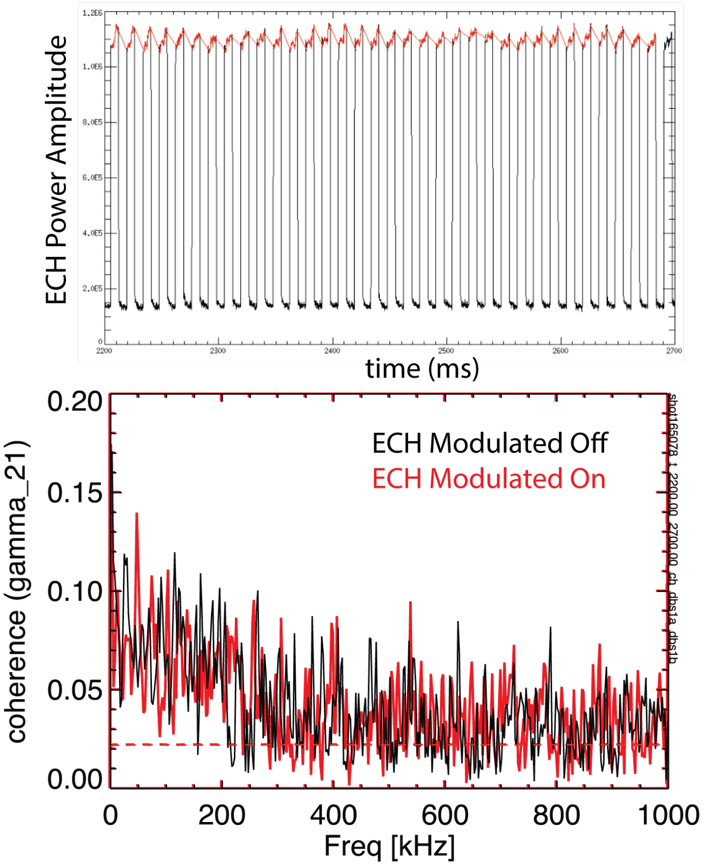

Figure 4.9: Correlation ECE measures the turbulent temperature fluctuations at the microwave scale. The black trace measures turbulence with power on, and red with power off. The coherence $gamma_{12}$ is proportional to the level of millimeter scale temperature fluctuations.

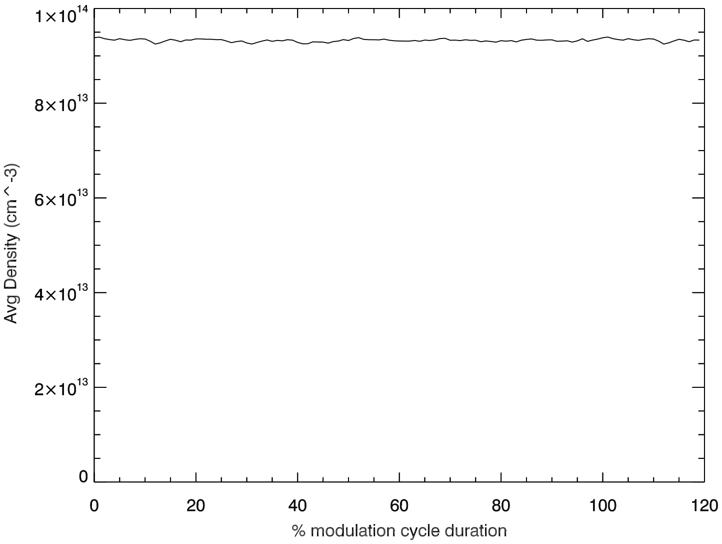

Figure 4.10: A coherently averaged density perturbation measured by core interferometery. This discharge shows the most substantial density variation of those sampled showing a visible shift of $\delta n_e/n_e < 1\%$. Such minor density modulation should not substantially alter the heat flux, but density dependencies will still be treated in fitting in Section 4.3.6.

port. This leads to an approximation - the transported derivative of density with the modulation is small. Because microwave power is a strictly heat source, its absolute time derivative is zero. Particle flux Γ_e is thus the only source of the density changes are flows induced in the plasma. This follows from the conservation equation:

$$\frac{dn_e}{dt} = \frac{\partial n_e}{\partial t} + \frac{\partial \Gamma_e}{\partial x} = \frac{\partial \Gamma_e}{\partial x} \tag{4.11}$$

$\tilde{\Gamma}_e \approx 0$ is then a valid approximation - particle flux does not vary considerably over the modulation cycle. The weak response of parameters other than temperature to modulation will help to simplify the heat equation in the upcoming section.

4.3 Energy Conservation & Transport-Driven Fluxes

4.3.1 Defining a Broadening Factor

Density fluctuations evolve and move past the ECH beam quickly enough that only their average effect can be measured. The turbulent eddy turnover time (100 μs) is slow compared to the RF propagation. When writing the heat equation, this separation of scales greatly simplifies the linearizion, allowing the heat equation to be grouped into constant and modulated terms through a baseline subtraction. Turbulence appears 'frozen-in' to the RF beam, but varies substantially over the thermal and particle transport timescales[55].

A variety of cases will be considered in the following sections, but all will make use of a simply defined broadening factor. The width of the ECH deposition profile is a function of numerous factors. The injected beam width, trajectory relative to the magnetic field and density gradient, and the temperature at the deposition region all play a significant role[37]. In this work, it will be convenient to express a broadening factor over the basic TORAY-GA profile which already treated these effects. Beam waist scales linearly with deposition profile width, with the exact proportionality being a function of the poloidal angles. Thus for this work we can consider a broadened profile which is the result of a convolution of the base deposition profile in 1D with a broadening function, as shown in its slab geometry form in Eq. 4.12.

$$p_{broad}(\rho) = \int_0^{\rho} p_{TORAY}(\rho') * B(\rho - \rho') d\rho' \tag{4.12}$$

For this analysis, a power conserving Gaussian filter is applied. The width of the Gaussian are quantified by a ratio, $b = FWHM_{Broadened}/FWHM_{TORAY-GA}$. The fitting method was first applied to the core-targeted discharge 165078. A set of broadening Gaussians with a FWHM in $\delta\rho$ ranging from .005 to .01 were applied to the dataset. A comparison of two broadened and an unbroadened heating profiles is shown in Fig. 4.11 below.

The consistency of these broadened profiles with measured perturbations will be assessed through transport fitting.

4.3.2 Broadening in Cylindrical Geometry

In this work, we consider a power deposition primarily in a cylindrical geometry. To conserve power while broadening a deposition function in

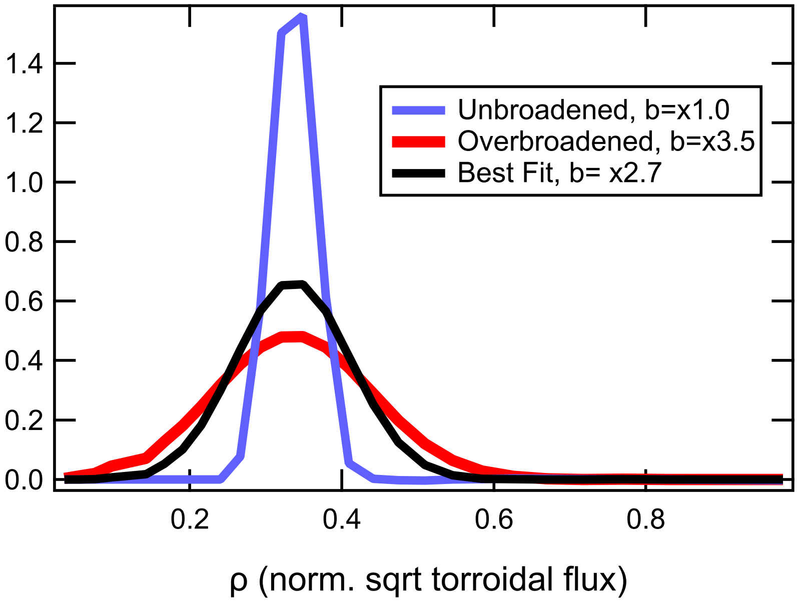

Figure 4.11: Power deposition profiles for an unbroadened TORAY-GA profile and two broadened profiles are shown. The selected diverted H-mode discharge used to evaluate these profiles shows the greatest degree of broadening of any study. In the following sections, it will be shown that fitting of a transport model can determine which of these source functions best corresponds to the measured perturbation.

cylindrical coordinates, a slightly different form, Eq. 4.13 must be used.

$$p_{broad} = \frac{1}{\rho}\int_0^{\rho} p_{TORAY}(\rho') * B(\rho - \rho')\rho' d\rho' \tag{4.13}$$

Using this form allows a broadening which accounts for the fact that power is redistributed along flux surfaces. A power-conserving radial form in cylindrical coordinates is the most needed in this work. The 1/R major radius expansion that comes with tokamak geometry is not treated, as this would require recourse to a full 3D transport model which cannot be diagnosed with existing 1D profile measurements.

As we can see from this result from TORAY-GA, 4.12, power deposition per unit volume is well-defined by a Gaussian shape. TORAY-GA performs its heat flux calculations in a power-normalized form, but presents ECH deposition in a per unit volume normalized form as needed for comparison with a radially-varying temperature perturbation. This is physically intuitive - an ideal ray carrying the same power, when scattered further out into the tokamak, will produce a smaller temperature perturbation than one which lands further inboard because there is more plasma in the cross sectional area hit by the ECH ray. In a cross-sectional sense this results in a flux which falls off by $1/r$ when performing the calculations in cylindrical coordinates.

High quality fitting which crosses the source region requires the 1/r falloff of cylindrical coordinates to converge, rather than a step function character. This fall-off in the power of this form matches the observed fall-off

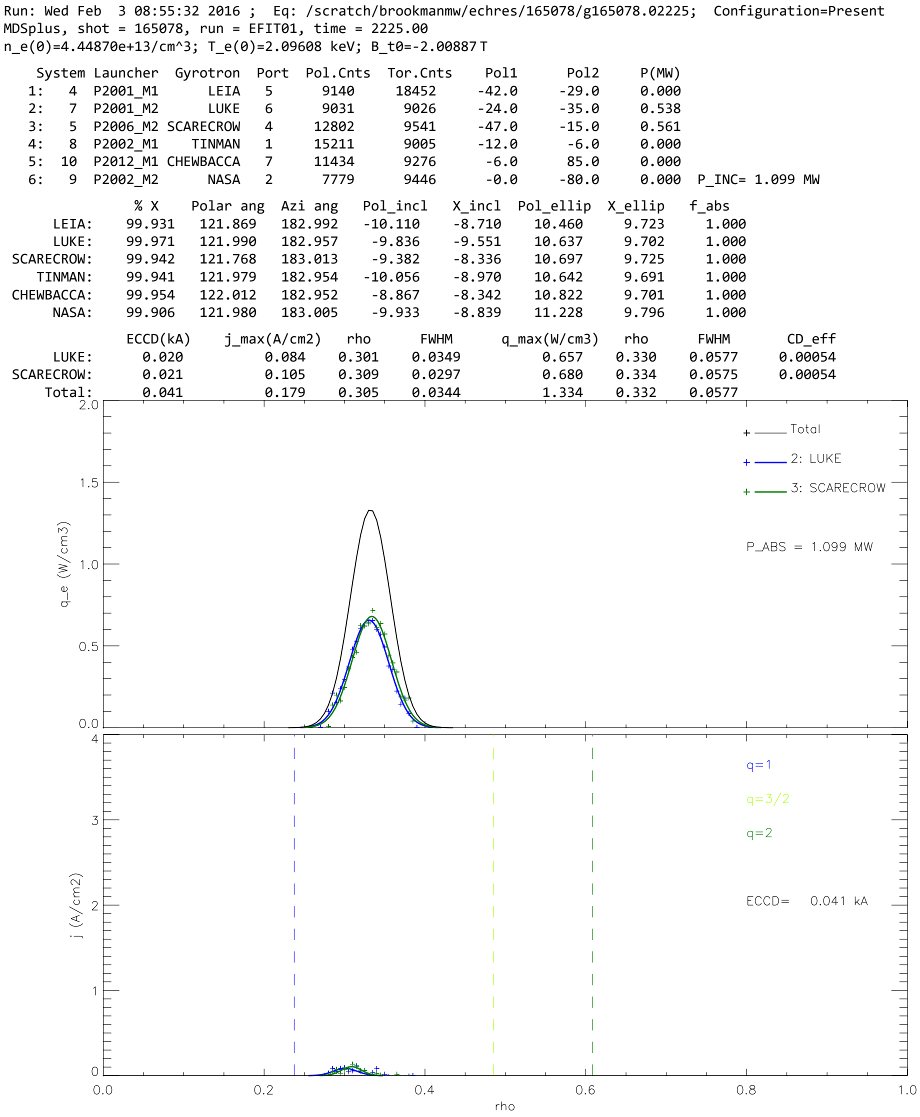

```
Run: Wed Feb  3 08:55:32 2016 ;  Eq: /scratch/brookmanmw/echres/165078/g165078.02225;  Configuration=Present
MDSplus, shot = 165078, run = EFIT01, time = 2225.00
n_e(0)=4.44870e+13/cm^3; T_e(0)=2.09608 keV; B_t0=-2.00887 T

    System Launcher  Gyrotron  Port  Pol.Cnts  Tor.Cnts    Pol1      Pol2     P(MW)
   1:   4  P2001_M1      LEIA   5      9140     18452     -42.0     -29.0     0.000
   2:   7  P2001_M2      LUKE   6      9031      9026     -24.0     -35.0     0.538
   3:   5  P2006_M2 SCARECROW   4     12802      9541     -47.0     -15.0     0.561
   4:   8  P2002_M1    TINMAN   1     15211      9005     -12.0      -6.0     0.000
   5:  10  P2012_M1 CHEWBACCA   7     11434      9276      -6.0      85.0     0.000
   6:   9  P2002_M2      NASA   2      7779      9446      -0.0     -80.0     0.000  P_INC= 1.099 MW

              % X     Polar ang  Azi ang   Pol_incl   X_incl  Pol_ellip  X_ellip   f_abs
      LEIA:    99.931   121.869   182.992   -10.110    -8.710    10.460     9.723     1.000
      LUKE:    99.971   121.990   182.957    -9.836    -9.551    10.637     9.702     1.000
 SCARECROW:    99.942   121.768   183.013    -9.382    -8.336    10.697     9.725     1.000
    TINMAN:    99.941   121.979   182.954   -10.056    -8.970    10.642     9.691     1.000
 CHEWBACCA:    99.954   122.012   182.952    -8.867    -8.342    10.822     9.701     1.000
      NASA:    99.906   121.980   183.005    -9.933    -8.839    11.228     9.796     1.000

              ECCD(kA)    j_max(A/cm2)    rho      FWHM      q_max(W/cm3)    rho      FWHM       CD_eff
      LUKE:     0.020           0.084    0.301    0.0349           0.657    0.330    0.0577     0.00054
 SCARECROW:     0.021           0.105    0.309    0.0297           0.680    0.334    0.0575     0.00054
     Total:     0.041           0.179    0.305    0.0344           1.334    0.332    0.0577
```

Figure 4.12: TORAY-GA deposition report for the 165078 discharge.The $q_e(\rho)$ is equivalent to $p_{ECH}(\rho)$ and is a power per unit volume. Power and current drive profiles can be characterized by a Gaussian fit with a defined FWHM. Convolution of two Gaussians by definition produces another Gaussian with a width $\sigma_{new} = \sqrt{\sigma_{ECH}^2 + \sigma_b^2}$. Broadening is performed on a per-gyrotron basis. The toroidal angle on this discharge does not generate a substantial driven current.

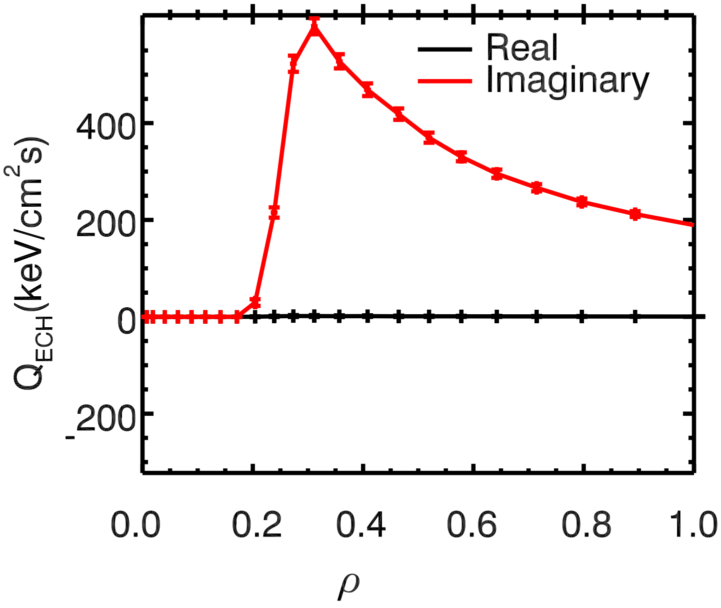

Figure 4.13: Integrated in cylindrical geometry, the per particle power deposition, here converted from the TORAY-GA default watts to keV.

in temperature perturbation. Examples of the integrated per-particle source function are displayed in Figure 4.13.

4.3.3 Energy Conservation Generated Fluxes

This work solves the heat equation for a set of heat fluxes through integration of the measured temperature perturbation $\tilde{T}_e$ and a trial $\tilde{p}_{ECH}$ profile ($\tilde{p}_{ECH}$ being the differential form of $\tilde{P}_{ECH}$). When treating the transport in cylindrical geometry, the heat flux contains an inherent $1/r$ radial variation, rather than the step character found for the same calculation in a slab geometry used in past studies[109]. Using separation of variables in r and t, the time-dependent portions can be Fourier transformed with the kernel $e^{2\pi i n f_{mod} t}$ into a harmonic series in modulation frequency, $f = f_{mod} * n$. Terms without a time dependence pass through as constants.

$$\tilde{Q}_e(r,t) = \frac{1}{r}\int_{r'=0}^{r}\left(\tilde{p}_{ECH}(r',t) - 3/2 n_e(r')\frac{\partial \tilde{T}_e(r',t)}{\partial t}\right) r' dr \tag{4.14}$$

Leveraging separation of variables in r and t, the time-dependent portions can be Fourier transformed with the kernal $e^{2\pi i n f_{mod} t}$ into a harmonic series in modulation frequency, $f = f_{mod} * n$. Terms without a time dependence pass through as constants.

$$\tilde{Q}_e\left(r,f\right) = \frac{1}{r}\int_{r'=0}^{r}\left(\tilde{p}_{ECH}(r',f) - 3i\pi f n_e(r')\tilde{T}_e(r',f)\right) r' dr \tag{4.15}$$

The key to this method is a combination of perturbative temperature measurements and broadened, properly phased deposition profiles. Fourier Analysis of ECH power comes from the calibrated forward power signals. Profiles come from an set of 5-10 of TORAY-GA power deposition simulations. The TORAY-GA ray tracing code already accounts for the effects of geometry and temperature on propagation[52], and the broadening factor b defined previously will be used as a metric. Differences in deposition profiles generate differences in heat flux. A comparison of fluxes based on broadened and unbroadened profiles is shown in Fig. 4.14 below. $\tilde{Q}_e$ is a complex number, and such can be expressed as amplitude and phase, which is physically intuitive, or in the form 'x+iy'. The latter form is easier to integrate and thus is the form used for analysis. Agreement between the calculated heat flux which follows from power conservation and the heat flux defined by a transport model is

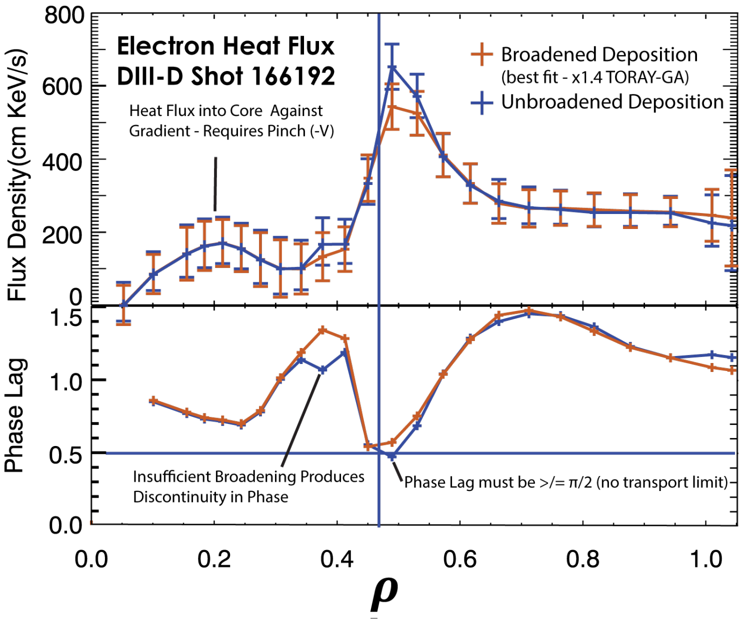

Figure 4.14: Amplitude and phase resulting from two different choices of ECH profile are shown. Comparing a broadened profile with an unbroadened profile produces key differences in the deposition region. A key indicator of the need for broadening is the phase lag of the unbroadened case. In this case, overestimating the peak heat deposition by using a TORAY-GA width profile produces a phase less than the $\pi/2$. Convective flows are needed to pull heat into the core in both cases.

key to this method. In the next section a transport model is defined based on modulation parameters.

The absolute differences in the profiles are small, but these differences strongly impact the fitting of transport coefficients, which will be considered in the next section.

4.3.4 Defining Transport Coefficients

The consistency between the calculated 1D heat flux and a 1D transport model is used in this work as a metric to evaluate broadened power deposition profiles. Strictly diffusive models fail to capture heat which flows against the gradient in many microwave heated plasmas[51]. Following the form of Ryter *et al*[68], diffusive (denoted by the coefficient D) and convective (denoted by the coefficient V) components are necessary to capture the effects of microwave heating. Expressing this as an equation for heat flux, Q_e:

$$Q_e\left(\rho, t\right) = -Dn_e \nabla T + Vn_e T. \tag{4.16}$$

The D and V coefficients are not constant. They can vary both radially and over the power modulation cycle, with an unknown dependence on tokamak parameters. Linearizing this form in time allows modulation-independent background heat flux to be seperated from the modulation induced portion, denoted $\tilde{Q}_e$.

$$\tilde{Q}_e = n_e(-D\nabla\tilde{T}_e - \tilde{D}\nabla T_e + V\tilde{T}_e + \tilde{V}T_e) + \tilde{n}_e(-D\nabla T_e + VT_e) \tag{4.17}$$

Rather than expanding directly in time, $\tilde{D}$ and $\tilde{V}$ are expressed as a set of partial derivatives in the dominant $\tilde{T}_e$ modulation[70].

$$\tilde{D} = \nabla\tilde{T}_e\frac{\partial D}{\partial\nabla T_e} + \tilde{T}_e\frac{\partial D}{\partial T_e} + \tilde{n}_e\frac{\partial D}{\partial n_e} + \nabla\tilde{n}_e\frac{\partial\nabla D}{\partial\nabla n_e} \tag{4.18}$$

$$\tilde{V} = \tilde{T}_e \frac{\partial V}{\partial T_e} + \nabla \tilde{n}_e \frac{\partial V}{\partial \nabla n_e} + \tilde{n}_e \frac{\partial V}{\partial n_e} \tag{4.19}$$

4.3.5 Grouping Modulated Terms into a Fitting Equation

The heat flux expressed by the transport model is complicated, Eq 4.17 has a number of dependencies. Inserting equations 4.18 and 4.19 into the flux formulation Eq 4.17 produces an equation for modulated heat flux. The dependences in these terms are complex, but we can use past work[70] to guide our grouping into a set of independent fitting parameters based on the dependence on the temperature perturbation $\tilde{T}_e$. Three terms are used - a convective term proportional to $\tilde{T}_e$, a diffusive term proportional to $\nabla\tilde{T}_e$, and one which depends on neither. These can be understood respectively as a convective, diffusive, and coupled heat flux. Sorting of this form is helpful, as temperature perturbation is much larger than the density perturbation, which is seen to be less than 1% in coherently averaged interferometer data.

$$\begin{aligned}\tilde{Q}_e = &-\nabla\tilde{T}_e(D + \nabla\ T_e \frac{\partial D}{\partial \nabla T_e}) + \tilde{T}_e(V + T_e \frac{\partial V}{\partial T_e} - \nabla\ T_e \frac{\partial D}{\partial T_e}) \\ &+ \nabla\tilde{n}_e(T_e \frac{\partial V}{\nabla n_e} - \nabla T_e \frac{\partial D}{\nabla n_e}) + \tilde{n}_e(T_e(\frac{V}{n_e} + \frac{\partial V}{\partial n_e}) - \nabla T_e(\frac{D}{n_e} + \frac{\partial D}{\partial n_e}))\end{aligned} \tag{4.20}$$

The modulated diffusion term can be assembled from all terms proportional to $\nabla\tilde{T}_e$:

$$D_M = D + \nabla\ T_e \frac{\partial D}{\partial \nabla T_e} \tag{4.21}$$

Similarly a modulation convection can be assembled from all terms containing $\tilde{T}_e$

$$V_M = V + T_e \frac{\partial V}{\partial T_e} - \nabla\ T_e \frac{\partial D}{\partial T_e} \tag{4.22}$$

The remaining terms are combined into coupled transport, $\tilde{\xi}$, which is discussed in the next section.

4.3.6 Coupled Transport

Coupled transport, $\tilde{\xi}$, contains terms driven by the modulated density and its gradient and any other small corrections. These could include an apparent flux from motion of ECE measurement locations due to plasma shift, non-thermal transport, modulated ion-electron exchange power, and Ohmic power modulation. These are grouped together as $\tilde{\xi}$ for the fit as they are functionally independent of the perturbed terms.

$$\tilde{\xi} = \frac{\nabla \tilde{n}_e}{n_e}(T_e \frac{\partial V}{\nabla n_e} - \nabla T_e \frac{\partial D}{\nabla n_e}) + \frac{\tilde{n}_e}{n_e}(T_e(\frac{V}{n_e} + \frac{\partial V}{\partial n_e}) - \nabla T_e(\frac{D}{n_e} + \frac{\partial D}{\partial n_e})) \tag{4.23}$$

This $\tilde{\xi}$ term must be given some frequency dependence to simultaneously fit fluxes across harmonics. The physical interpretation of this fact is that the $\tilde{\xi}$ term must evolve over the modulation cycle much as the other terms do. As used in past ballistic heat pulse work by Fredrickson[82], an exponential decay with a free phase can capture the dominant time response of the coupled transport. This term could also in principle capture the effects of fast electron transport modification to diffusion. The exponential decay of the form $f(t) = A * exp(-ct)$ has a Fourier transform $F(f) = 2A/(c + i2\pi f)$.

The modulation of diffusion is not necessarily in phase with the turn-on of the ECH perturbation, or the peak of temperature. Pulling the imaginary component out as a phase term θ_ξ, and the amplitude as $\xi_0 = A\sqrt{c^2 + (2\pi f)^2}$ allows simplification to the fitting form of $\tilde{\xi}$:

$$\tilde{\xi}(r, f) = \xi_0(r) \times e^{i\theta_\xi} \times \frac{4\pi c}{4\pi f_{mod}^2 + c^2} \tag{4.24}$$

Writing a fit term with this freedom allows a ballistic population without enforcing it. Both diffusion and convection are present to account for bulk components of the heat flux. Estimates for ITER parameters suggest that the level of fast electron transport predicted ($D_{rr} \approx .15 m^2 s^{-1}$) will not lead to a substantial broadening of the ECCD profile[75]. DIII-D studies which did not treat fluctuation broadening capped the levels of diffusive transport for fast electrons at a minimal $D_{rr} = 0.4 m^2 s^{-1}$[76]. While transport at this level can drive profile broadening, a value of $D_{rr} = 1.0 m^2 s^{-1}$ is considered the minimum level for deleterious broadening[75]. The observed broadening for L-mode is consistent to within uncertainties for both core and edge deposition in DIII-D, whereas the work of Harvey *et. al.*[77] predicts two orders of magnitude difference between edge and core current diffusion times. If diffusion of hot particles confounded broadening, b factors for core and edge deposition would differ, which is not found to be the case. Thus this work considered fast electron effects, if they are present, should be addressed by the $\tilde{\xi}$ term.

Fitting finds the amplitude of the coupled transport driven flux is smaller than either the diffusive or coupled terms. Only a fraction of the flux (15% at most) comes from coupled transport in the fitting discussed in the next section. Thus this work does not attempt to reduce ξ to its potential dependencies.

4.3.7 The Reduced Transport Model

These simplifications allow the complexity of Eq. 4.20 to be reduced to a simpler parameter set which can capture the bulk profile dependencies of modulated heat transport. Writing the coefficients in their simplified forms gives Eq. 4.25.

$$\tilde{Q}_e(r,t)/n_e(r,t) = -D_M \nabla \tilde{T}_e + V_M \tilde{T}_e + \tilde{\xi} \tag{4.25}$$

The consistency of this transport model with a chosen deposition function can be evaluated. Eq. 4.25 is compared the heat flux from energy conservation, Eq. 4.15 and agreement between these two forms of flux is used as a check on ECH deposition. The energy conservation derived heat flux is sensitive to $\tilde{p}_{ECH}(r,f)$.

4.3.8 Performing the Fit

Eq. 4.25 has five unknown parameters - D_M, V_M, and the 3 parameters of $\hat{\xi}$ are fit to the sets of heat fluxes calculated for each of the trial P_{ECH} deposition profiles. This avoids the challenge of conserving the total input power in a fit parameter form of P_{ECH} which includes radial variation. Fits are performed using the uncertainties propagated in each parameter using orthogonal distance regression, (ODR)[78]. A traditional least-squares fit uses variation of an independent variable, here $\hat{Q}_e/n_e$, to minimize the quadrature difference between the calculated and fit values. ODR uses variation of parameters in the dependent variables as well as the independent variable.

The independent variables, $\nabla\tilde{T}_e$, and $\tilde{T}_e$ no longer need to be taken as exact, when they in fact have uncertainties comparable to those of $\tilde{Q}_e$ When fitting the heat equation both the independent and dependent variables have substantial known errors. Q_e and its uncertainty are Monte Carlo integral quantities, not strictly local. Errors in $\nabla\hat{T}_e$ are larger than those in $\hat{T}_e$, but are of a similar magnitude. To treat these errors, ODR varies dependent variables as well, minimizing the uncertainty-weighted orthogonal separation between the data points. ODR fitting is used throughout the remainder of this work.

Fitting is performed by flatting the two variable dependency in r and f to a 1D array of all fit parameters. Because the flux at each location is fit as a function of local parameters, this form of fitting, shown in Fig. 4.15, does not conflate the frequency and radial coordinate, but rather attempts to maximize agreement consistent across the real and imaginary parts(the first and second half), against frequency (which defines the repeating bands in Fig. 4.15), and the radial coordinate.

Transport coefficients can change by an order of magnitude or more across the tokamak[50]. In the next section, results are presented from both locally constant fits made over a limited range of ρ and from polynomial fit coefficients. Benchmarking shows that these two methods are consistent to

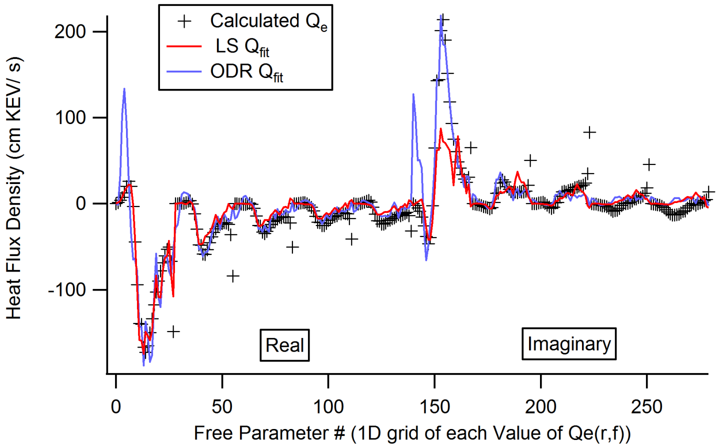

Figure 4.15: The fitting grid, nominally a function of two indirect variables, major radius and time, flatted into one dimension, in bands of channels transformed at the same frequency. The differences between results from orthogonal distance and a least squares fit are clear. Use of uncertainties derived from experiment to fit the nominally independent variable basis helps to substantially improve fits.

within the propagated uncertainties.

Chapter 5

Experimentally Separating Broadening and Transport

5.1 Overview

This section presents results of transport analysis of a set of modulated ECH experiments on the DIII-D Tokamak using the method of the previous chapter. A limited range of discharges with modulated ECH power was available in the historical dataset. These were supplemented by a number of results taken in piggyback and a half day of dedicated experiments. Dedicated discharge in consistent shapes explore the impact of geometry and power modulation, while a broad range of discharges produces substantial variation in edge turbulence. The level of millimeter-scale fluctuations conditions is a product of discharge conditions - QH-, H-, and L- mode have significant variations in edge turbulence. Only through varying the confinement mode can scattering-relevant fluctuations be varied enough to produce a scaling. For example, in a shape-matched discharge, the transition between L- and H-mode is associated with a factor of ≈ 4 drop in fluctuations measured by Doppler backscattering.

5.2 Discharge Conditions Explored

A range of discharge conditions with significantly different edge character can be achieved on DIII-D. This set of conditions were used as a means to produce an order of magnitude variation in fluctuation amplitude. Measurements in millimeter-scale fluctuations were taken with Doppler backscattering, supplemented by beam emission spectroscopy. L-mode is the default tokamak operating scenario, which has a substantial level of fluctuations associated with the density gradient at the edge of the machine[55]. During these experiments, fluctuations increased when the plasma is in a diverted configuration, as opposed to a limited configuration. The formation of an H-mode pedestal is known to be related to zonal flow suppression of turbulence[58]. Thus the time integrated edge fluctuation level measured in H-mode between prompt flows driven by edge localized modes is far lower than that measured in L-mode. QH-mode is a modification to H-mode wherein the pedestal is stabilized by a series of oscillations which have been found to lead to increased short wavelength turbulence [79]. Negative triangularity (-δ) L-mode discharges, a novel concept run on DIII-D, found the lowest levels of fluctuations. Similar discharges on TCV found substantially reduced turbulence was driven by changes in the shape-dependent trapped electron mode turbulence[80].

Only through varying the confinement mode can scattering-relevant fluctuations be varied enough to produce a scaling. For example, in a shape-matched discharge, the transition between L- and H-mode is associated with a factor of ≈ 4 drop in fluctuations measured by Doppler backscattering. Despite changes in geometry and temperature which accompany such a transition, it is possible to compare different conditions. Simulation find scattering-relevant fluctuations are significant only in the tokamak edge[3]. The discharges used in this effort can be found in table 5.2

Shot #	Confinement Mode	$f_{mod}(Hz)$	ρ_{ECH}
165146	ELM-y H-mode	70	$\rho = .25$
165147	ELM-y H-mode	70	$\rho = .6$
$157141 - 7$	QH-mode	27	$\rho = .7$
165078	Diverted L-mode	70	$\rho = .25$
165079	Diverted L-mode	70	$\rho = .6$
153542	Limited L-mode	50	$\rho = .25$
$144566 - 75$	Limited L-mode	50	$\rho = .6$
$166191 - 2$	$-\delta$ L-mode	50	$\rho = .45$

Table 5.1: A number of different discharges have the modulation data necessary for this perturbative analysis. This dataset consists of a large variety of modulation frequencies, deposition locations, and ECH powers.

Despite changes in geometry and temperature which accompany such a a variety of discharges, it is possible to compare different conditions. Simulations (Section 3.5) find scattering is significant only in the tokamak edge. Here, the interaction produces an effectively wider beam which then propagates normally into the core. TORAY-GA already accounts for the effects of geometry and temperature on propagation because it assumes an implicit beam width. Thus to separate those effects from the increased beam waist this work uses the broadening parameter, defined previously as $b = FWHM_{ECH}/FWHM_{TORAY}$. This b factor will be used together with turbulence amplitude to define a scaling relation.

Discharge:	Negative Triangularity	Diverted H- mode	QH- mode	Limited L- Mode	Diverted L- mode
DBS $\tilde{n}_e$ Amplitude:	3	5	8	10	12

Table 5.2: This table contains information about the density fluctuation amplitude measured by Doppler backscattering for the 5 edge conditions studied. Uncertainties are not available for DBS data, but fluctuations over the region $\rho = .9$ to $\rho = 1$ vary by 20% in these cases.

The range of density turbulence levels experienced in these discharges is placed into Table 5.2. Long averaging times mean the time-error is essentially negligible. Modulation rates are set to avoid transitions.

5.3 Fitting Results

5.3.1 Turbulence Variation Through Matched H- and L- Mode Discharges

Between H- and L-mode, the changes are modest - the ray path is similar, the core density is matched through gas puffing. The L-mode, however, possess a substantially higher degree of edge turbulence. Suppression of turbulence through zonal flows is the leading explanation for the formation of the H-mode pedestal. Thus the reduced turbulence measured in H-mode (see Sec. 3.3) is to be expected. Given the similarity of the discharge geometry, one can consider the consistency of the broadening factor under the differing levels of turbulence. Deposition and plasma profiles, as well as the Doppler backscattering channel measuring edge fluctuations for two matched core heating discharges are shown in Fig. 5.1.

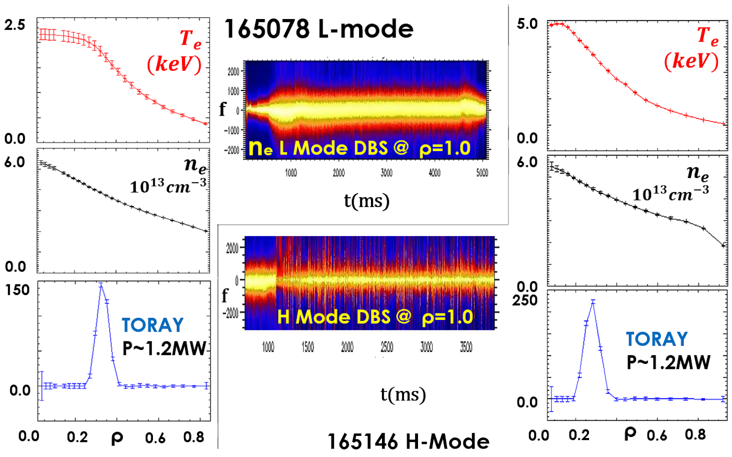

Figure 5.1: Electron density, temperature and power deposition traces are shown for the two discharges being compared. Also shown is the DBS power spectrum from an edge channel located at $\rho = .95$. It is this DBS channel which will be used in the following sections to quantify the edge turbulence responsible for scattering. Measured turbulence does not appear to be modulated by the ECH power.

Two power levels, 3 MW for H-mode and 1.2 MW for L-mode, were applied with $f_{mod} = 70Hz$. This is to avoid over-perturbing the L-mode discharge to the point where the plasma begins a rigid shift. Density and deposition location are matched in the shapes, but improved H-mode confinement leads to a higher temperature. This broadens the ECH resonance, but this effect is already treated by the TORAY-GA ray tracing code. Edge turbulence drops with the formation of the H-mode pedestal[81], allowing for a comparison of broadening in the same shape at two turbulence levels.

5.3.2 Fitting Locally Constant Coefficients

To compare these H- and L-mode discharges, constant coefficients were fit in the range $\rho = (.3, .6)$ for a series of broadening factors. The H-mode discharge shown in Table 1 and the L-mode in Table 2 show a clear minimization of χ^2 and reasonable transport coefficient for broadened profiles, with L-mode requiring significantly more broadening than H-mode. Also shown in these tables are the characteristic times, c, which define the best fit exponential decay. The two best-fit cases produce very similar characteristic timescale for coupled transport at the best-fit broadening factor.

Fitting of locally constant coefficients to these three discharges finds a degree of broadening in line with the measured turbulence fluctuations. The diverted L-mode measures the highest level of fluctuations, as shown in Table 5.2. Limited L-mode shows a modestly reduced level of fluctuations, and fitting indicates a lower degree of broadening. The lowest level of fluctuations of the

Broad. Factor	$D_M(cm^2/s)$	$c(1/s)$	χ^2
×1	$1.9 \pm .4$	423	2223
×2.0	$4.7 \pm .5$	386	520
×2.5	$4.6 \pm .4$	321	588
×**2.75**	$3.5 \pm .2$	293	**346**
×3.2	$3.6 \pm .2$	-2844	555

Table 5.3: Transport coefficients (D and c) and goodness-of-fit for selected values of b. This diverted L-mode is best fit from $\rho = (0.3, 0.6)$ with a substantial broadening factor. Constant coefficients in this section and the polynomial results in the prior chapter used to introduce this method find identical factors.

Broad. Factor	$D_M(cm^2/s)$	$c(1/s)$	χ^2
×1	$3.2 \pm .1$	747	4067
×1.2	$1.2 \pm .1.4$	2191	1223
×1.5	1.4 ± 1	877	916
×**1.7**	2.7 ± 1.3	306	**223**
×2.3	$5.4 \pm .8$	7025	393

Table 5.4: This diverted H-mode discharge, which is matched in density and shape to the previous discharges, fits best from $\rho = (0.3, 0.6)$ with a modest ×1.7 broadening. Diffusion across all choices is similar to the ONETWO value for baseline diffusivity $\chi_{eff} = 1.7 - 2.5$, suggesting a weak dependence of D_M on the modulation.

three is found in H-mode, as is the smallest b value.

5.4 Validation of the Heat Flux Method

This section discusses validation of this method of transport fitting. Through comparison with past transport studies and with perturbations generated by simulation codes, a level of confidence in the heat flux method can be found.

Discharge:	Diverted L-mode	Limited L-mode	Diverted H-mode
TORAY FWHM	0.055	0.072	0.067
Best Fit FWHM	0.15	0.17	0.11
Factor	×2.7	×2.3	×1.7

Table 5.5: FWHM of the best fitting broadened $P_{ECH}(r)$ from different shots. These discharge modes have a steadily decreasing level of edge turbulence as measured by DBS. More discharges will be added to this scaling in the coming section.

5.4.1 Broadening Factor is Independent of Deposition Location

Throughout this work, we will use a broadening factor b to describe the broadening experienced by the microwave beam. The width of ECH deposition is affected by a number of factors, including path length through the edge, edge fluctuation amplitude, and the characteristics of the plasma in the deposition region (T_e, n_e, Z_{eff}). To demonstrate the basic validity of the broadening factor, consider deposition at two different radii in the same plasma. In a diverted L-mode discharge, power was targeted near to the core ($\rho = .25$) and to the edge ($\rho = .6$), as shown in Figure 5.2. The TORAY-calculated deposition width is impacted by changes in profile quantities and geometry. The temperature and density at the points in the profile differ sharply. This results in a deposition width in the edge of $FWHM_{edge} = .065$ and a deposition width in the core of $FWHM_{core} = .055$.

Turbulence does not vary significantly with this change, as in both case power deposition is well inside the edge region and heating powers are matched. There is an impact on sawtooth amplitude (more frequent sawteeth accompany core heating) but this effect is minimized by limiting fits to outside of the sawtooth inversion radius[82] at $\rho = .3$.

The inherent deposition widths in the target region differ as a result of the sharply different profiles and incidence angle of the RF beam on the resonance. The TORAY-GA FWHM for core deposition is $\Delta\rho = .066$, and for the edge $\Delta\rho = .055$. The heat flux fitting method was applied to both discharges, with chi^2 minimization having a clear minimum in b in each case (Fig. 5.3)

Consistency of broadening factor, at a value of ≈ 2.7, provides some confidence in its use as a metric. Altering the center of the deposition function in fitting this discharge did not produce improvements in goodness-of-fit. This is consistent with past results that suggest good agreement between simulated and experimentally measured deposition centers[83][50].

5.4.2 Comparison of Coefficients with the Differential Heat Pulse Formulation

This section demonstrates that the integral method can reproduce well the results of past transport studies. Validation of this heat flux-based fitting method has been performed against a set of modulated ECH data in L-mode. In a series of discharges, multiple unpulsed gyrotrons were targeted to alter the temperature gradient at the plasma edge. Power was incrementally moved from edge to mid-radius to steepen the gradient, producing the 'critical gradient' behavior, where transport coefficients are found to be a function of temperature gradient above a certain value of gradient or in this case scale

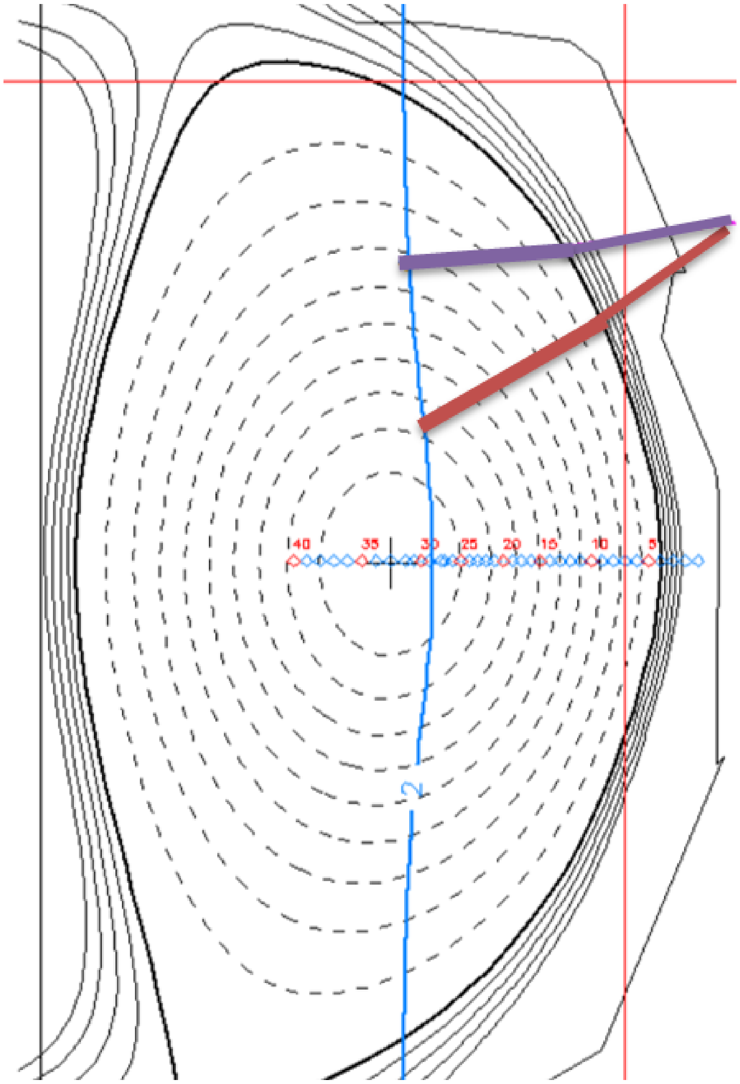

Figure 5.2: Shifting the targeting of heating power from the core to the edge in this diverted L-mode discharge does not substantially change the path through the edge fluctuations, but profile quantities at the two locations are sharply different. The inherent deposition in the core is significantly narrower in terms of $\Delta\rho$.

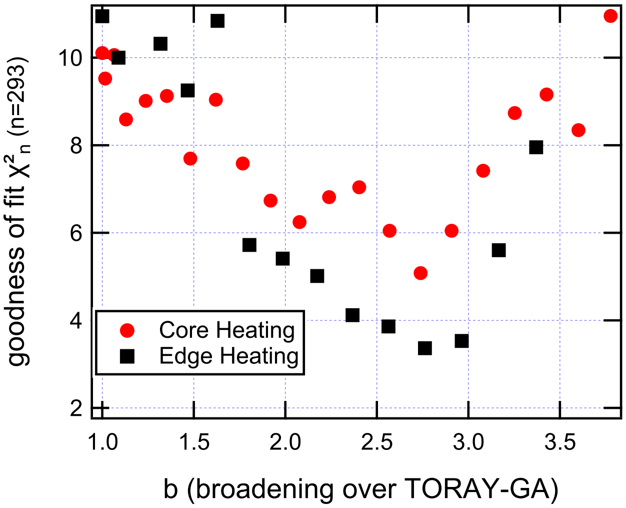

r

Figure 5.3: The χ^2 goodness of fit value is plotted against broadening factor for two cases. Core and edge deposition in the same discharge find a consistent broadening factor of ≈ 2.7, despite the 20% difference in TORAY-GA deposition width.

length $L_{T_e} = (\partial T_e/\partial r)/T_e$[109]. Results from this study, based on the differential form of the heat equation, can be used as a benchmark for the integral heat flux method presented here.

$$-D_{HP}\nabla^2\tilde{T}_e + V_{HP}\nabla\tilde{T}_e + \tilde{T}_e(\frac{3\pi}{f}i + \frac{1}{\tau}) = \tilde{P}_{ECH}/n_e \qquad (5.1)$$

DeBoo solves the heat equation in a different functional form, reproduced from his paper[109] as Eq. 5.1. The differential form of deBoo *et. al.* has a modulated diffusion, convection, and a third damping term $1/\tau$, similar to $\tilde{\xi}$. However, the order of the terms is different in this form, a second derivative of $\tilde{T}_e$ appears instead of an integral. This is advantageous as fitting can utilize the full errors in every quantity[6]. For experimental data, a second derivative is highly model dependent as are its uncertainties[50]. For a Monte Carlo integral, error bars are directly calculated from the uncertainty in the random draw. Minimizing intrinsic uncertainty in the fit equation improves the method's sensitivity to changes in power deposition.

To demonstrate the consistency of the integral method, it has been applied to the profile stiffness experiment of deBoo *et. al.*[109] This work fits transport coefficients to a limited radial range in a slab geometry. In the slab, the integral and differential form coefficients are directly comparable. Geometric factors do not enter the integral, and coefficients have no radial dependence. Thus $\int D_{HP}\nabla^2\tilde{T}_e dx$ is equivalent to $D_M\nabla\tilde{T}_e$, with a similar relation for V_M

and V . For example in cylindrical coordinates, the form is that of Eq. 5.2.

$$D_M = D_{HP} + 1/\nabla T_e \int_0^r \nabla D_{HP}(r')\nabla \tilde{T}_e(r')dr' \tag{5.2}$$

By limiting analysis to a constant value coefficient in the source-free region, the coefficients are comparable. This allows for a reproduction of the heat pulse measurements with a fitting of heat pulse data with constant coefficients just inside of the power deposition region at $\rho = .7$. A constant coefficient fit from $\rho = .2$ to $\rho = .6$ was made with both methods, and the results for the diffusion coefficient are given in Fig. 5.4.

5.5 Fit Transport Coefficients from Additional Discharges

This section discusses transport fitting results from discharges other than the diverted L-mode used to illustrate the broadening method above.

5.5.1 Limited L-mode

Limited L-mode discharges were the first explored with this method. A limited discharge is one where the last closed flux surface of the plasma is held next to the inner wall of the machine. Thus this surface defines the outer edge of the plasma, and seems to produce reduced turbulence as compared to the diverted L-mode discharge. chi^2 minimization again finds a clear minimum with increasing broadening factor.

Transport coefficients for this case were fit with a 5th order polynomial.

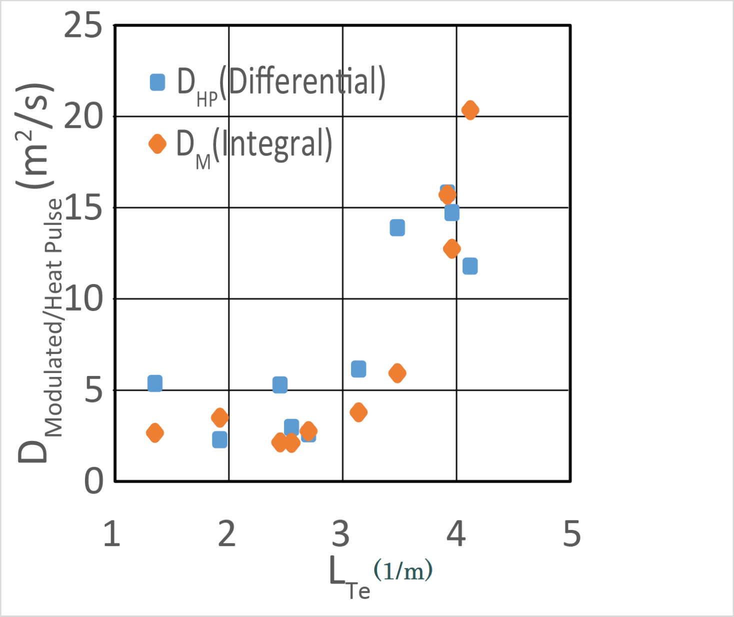

Figure 5.4: Integral method transport fitting can reproduce the critical gradient results from the perturbative experiment of deBoo *et. al.*[109]. The modulated diffusivity measured at $\rho = .6$ increases sharply as the electron temperature scale length, L_{T_e} approaches a critical value, here found to be $\approx 2.5m^{-}1$. The differential and flux integral method fits of diffusion coefficient are evaluated in a slab geometry from $\rho = .45$ to $\rho = .75$

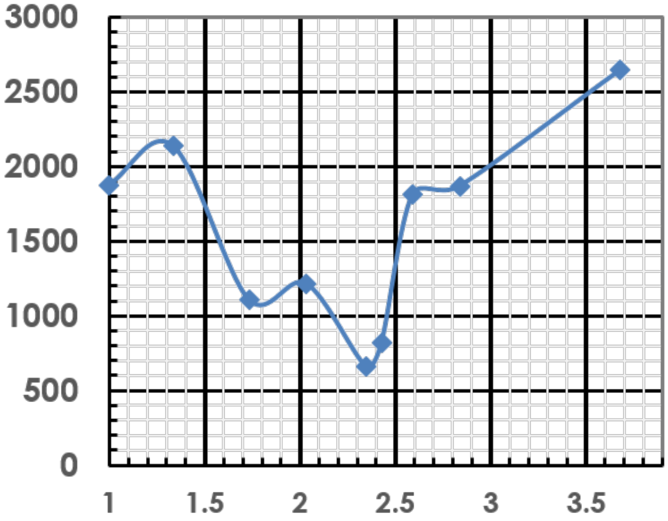

Figure 5.5: The inner wall limited discharge has a modestly lower level of turbulence than the diverted case considered above. χ^2 minimization carried out on an irregular grid was used to find the best fit b factor, which is approximately $2.3 \pm .3$.

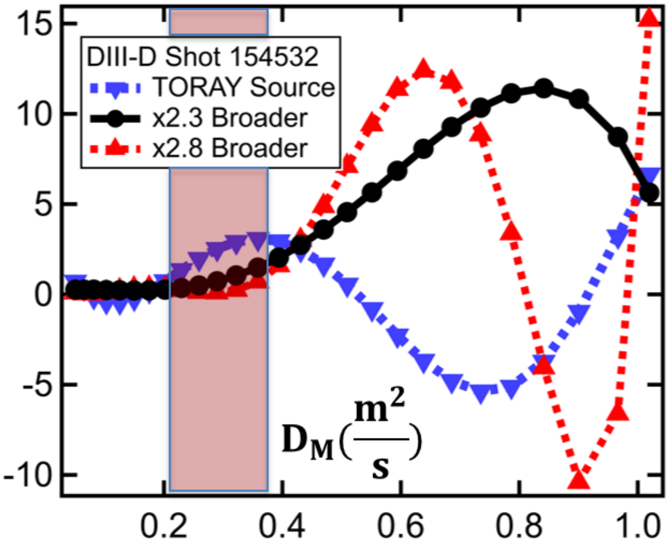

Figure 5.6: Smoothly varying ,consistently positive values of D_M for a Limited L-mode coincide with minimization of the χ^2. A 5th order polynomial can be used to represent radial variation in the Diffusion Coefficient (above). This can be compared to the ONETWO power balance diffusivity. The best fit occurs for a $b = 2.3 \pm .3$ broader FWHM for $P_{ECH}(r)$. This fits a consistently positive diffusion coefficient similar to the ONETWO value.

Results for 3 cases are shown in Fig. 5.6.

The modulated convection (Fig. 5.7) is higher in this discharge than any other, illustrating the significance of flows in the plasma for fitting microwave power deposition. It does not change significantly with changing broadening factor.

5.5.2 H-mode

Transport analysis in H-mode is complicated by the existence of edge localized modes (ELMs)[85]. This plasma phenomenon is generally considered

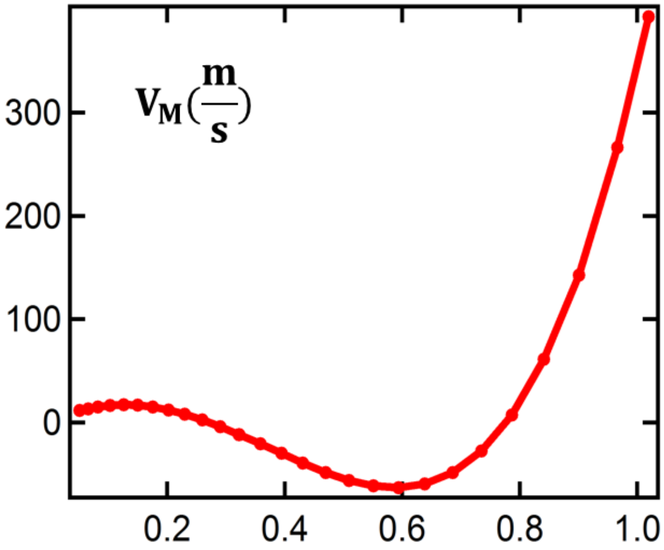

Figure 5.7: The modulated convection, V_M, plotted vs ρ. Adjusting b does not significantly alter the modulated convection profile, but the relative strength of convection is higher in this discharge than in any of the others studied.

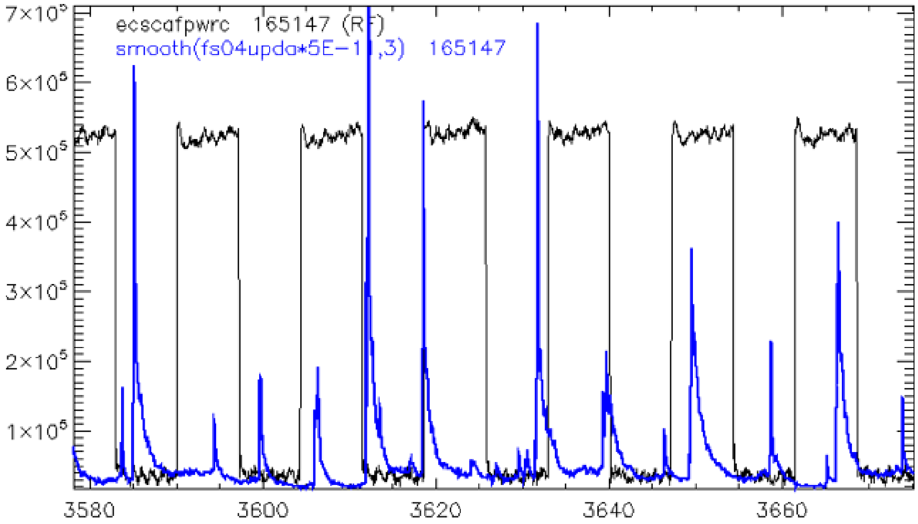

Figure 5.8: The line emission generated in the edge due to edge localized modes (ELMs) characterizes this phenomenon. Sharp, transient flows quickly relax the pedestal, carrying substantial energy with them. This confounds heat flux calculations in the ELM-perturbed region, $\rho > .6$.

to be a relaxation mode of the H-mode pedestal[86]. When high m/n number MHD modes in the edge approach a critical value, the result is a prompt flow of hot plasma from the outer plasma radius ($\rho > .6$) to the tokamak edge. These ELMs are detected by means of the D_α emission they generate (shown in Fig. 5.8), and their substantial effects on edge profile. An example of the change in the electron density profile shown in Fig. 5.9. Still, Hmode turbulence

The effects of ELMs (and potentially two islands, located outside of $\rho = .7$) have consequences for fit transport coefficients in this discharge. Outside of about $\rho = .6$, the 1D approximation used no longer applies. The coefficients, both diffusive and convective, go sharply negative outside of this radius.

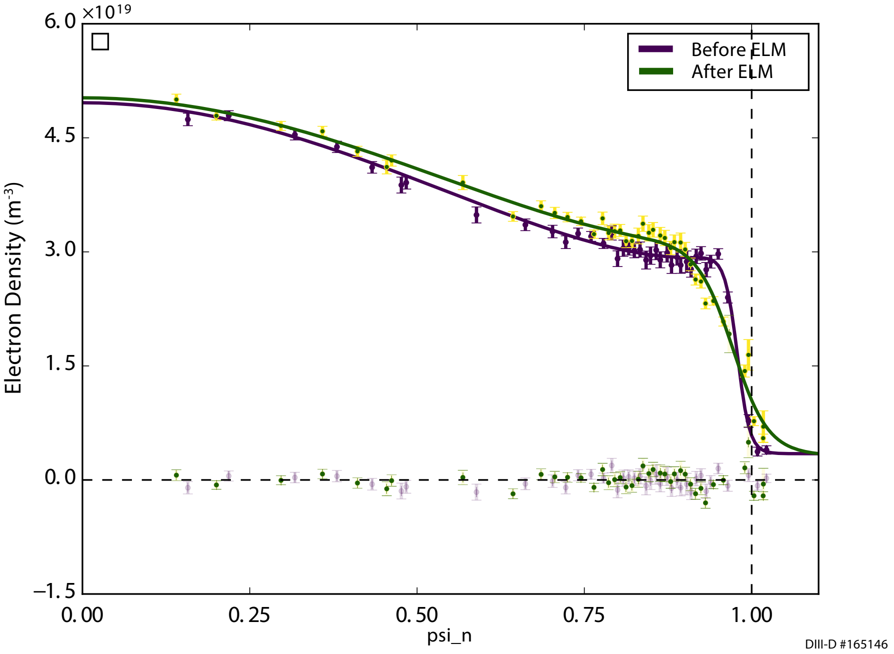

Figure 5.9: The change ELMs is clear in baseline profiles, such as this plot of electron density before and after the ELM crash. The primary effect of the ELM is to relax the edge gradient, but the effect of the perturbation extends further into the core of the plasma.

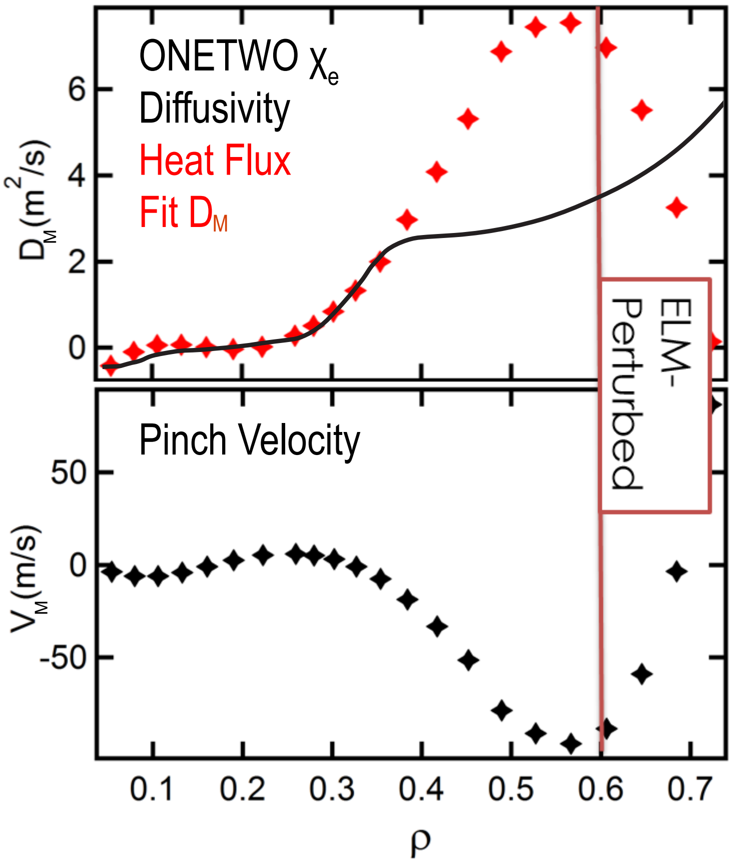

Figure 5.10: The modulated diffusivity and convection for an H-mode discharge are shown in this figure. In the core, the modulation diffusion is almost identical to the ONETWO derived diffusion, and convection is minimal. While ONETWO and modulated diffusivities do not necessarily match, agreement is good where the effects of modulation are minimal (inside the source region at $\rho = .25$).

5.5.3 Variation Between Locally Constant, Polynomial Coefficients

H-mode case provides an ideal test case for evaluating the viability of local coefficients. The local polynomial fit can potentially be influenced by features that are radially removed from the fit region. The ELM-perturbed edge of the H-mode generates a substantial flux, but when fitting a set of locally perturbed coefficients at the best-fit broadening factor, Fig. 5.11 shows a very good degree of consistency.

The base ONETWO-derived diffusivity is not necessarily identical to D_M, but where the dependencies of D on ∇T_e and T_e are not significant, the two should be comparable.

5.5.4 QH-mode

It must be noted that of the discharges studied, QH-mode shows the least improvement in ξ^2 with broadening. A minimal valley in ξ at $b = 1.9 \pm .4$ may be due to the weak impact of modulation on transport, as this discharge used only a single gyrotron to heat a high temperature plasma. This limits this discharge to fitting up to only the 11th harmonic. Also significant is the lower modulation frequency 27 Hz. Still, no significant density transport is seen with this modulation, nor modifications in the turbulence spectrum with ECH heating. Transport coefficients for the best fit case are shown in Figure

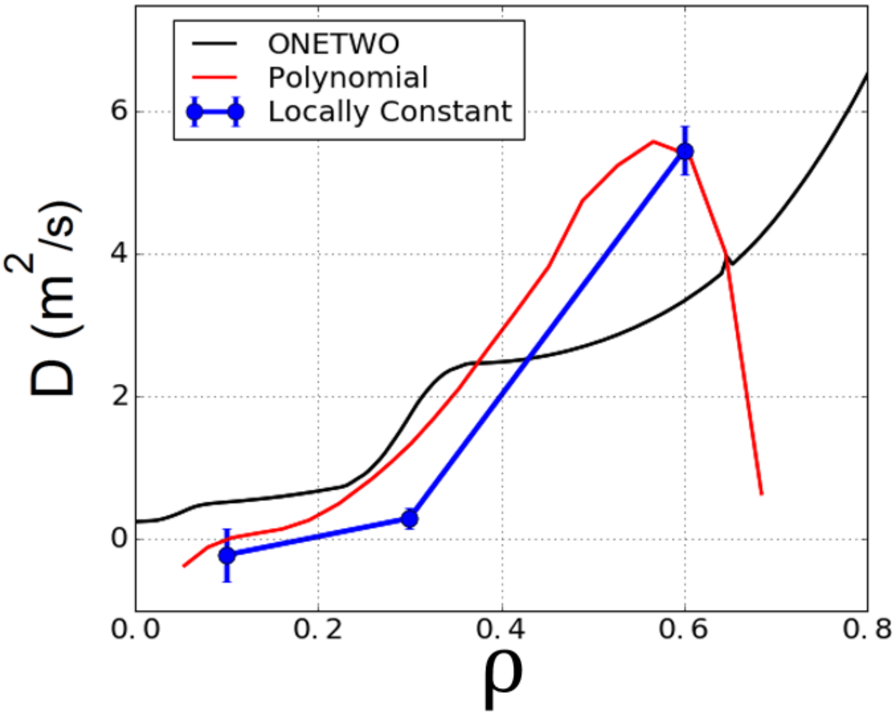

Figure 5.11: Polynomial and locally constant fits of coefficients in the H-mode discharge 165146. For locally constant coefficients, fits were performed from $\rho = 0 - .2$,$\rho = .2 - .4$,and $.4 - .8$. These are compared with the polynomial and baseline (non-modulated) ONETWO derived diffusivity. The form recovered by the two cases is very similar. The strongest difference is located at $\rho = .3$, which is within the deposition region.

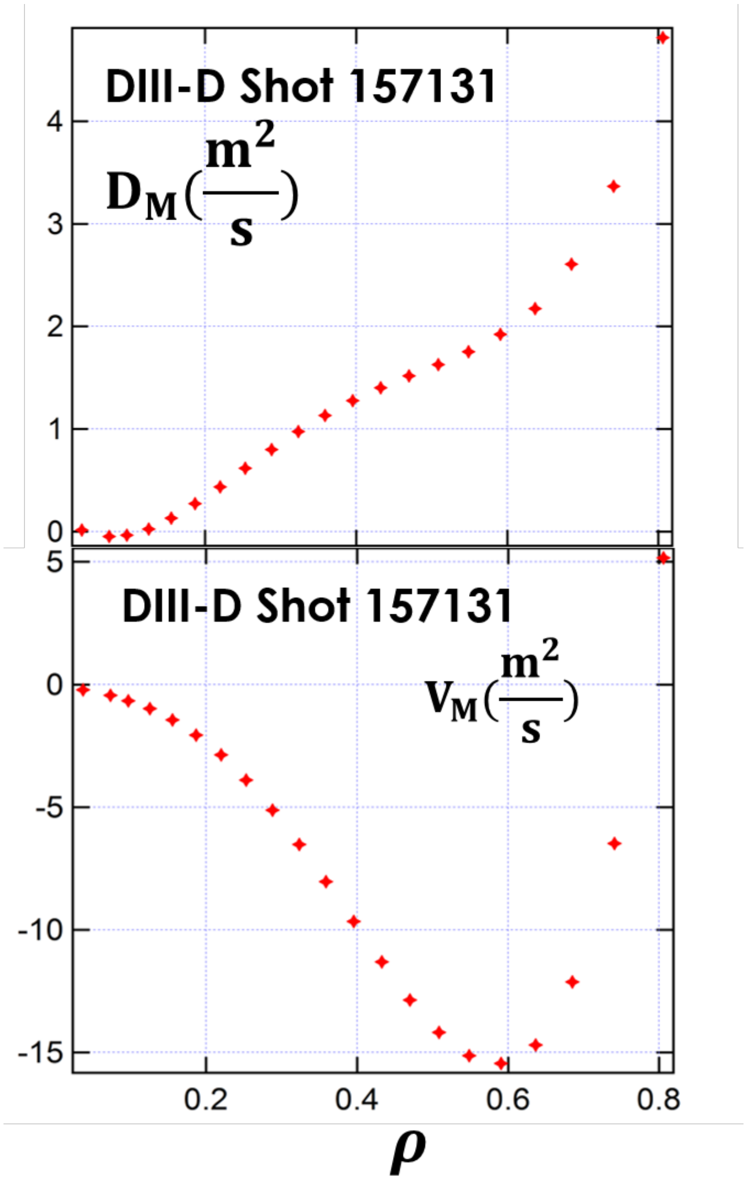

Figure 5.12: The modulated transport coefficients for a QH-mode discharge are consistently positive out to the edge, as there is no ELM perturbation to the heat flux. Levels of transport are also suppressed as compared to L-mode discharges fit earlier.

5.5.5 Negative Triangularity

Negative triangularity is a radical depature from other confinment modes on DIIID. By running an inverted discharge shape, a decrease of fluctuations is seen throughout the device. This is related to the suppression of TEM scale turbulence [80] . The low field side of the tokamak defines a sort of mirror machine on the low field side of the plasma. The same $1/R$ character than makes cyclotron emission useful as a diagnostic generates a trapped electron orbit, which runs from matched points on the top and bottom of the machine. This is known as a banana orbit.[15] These trapped electrons are associated with turbulent structures which cause significant large scale transport. Plasma shaping has a strong impact on the population of trapped electrons. Of special importance is the plasma triangularity, which parameterizes the relative location of top and bottom of the plasma compared to the outer midplane. Taking R_Z as the major radius of the top and bottom of the plasma, triangularity is defined as:

$$\delta = (R_{max} - R_Z)/a \tag{5.3}$$

Triangularity is positive in all other discharged considered in this work. When triangularity is negative, the top and bottom of the plasma are at a larger major radius than the magnetic axis. By operating in negative triangularity, the extent of the low field side of the plasma in R is limited, suppressing trapped particles and their associated turbulence[80]. A negative triangularity cross section is shown in Figure 5.13.

This discharge has some of the lowest turbulence levels measured, and consequently has the least broadening, with $b = 1.4 \pm .2$. Another effect of this suppression is improved confinement. While active efforts, led by Max Austin[84], are currently underway on DIII-D, initial pre-publication results suggest an H-mode level of confinement has been achieved in an L-mode discharge. The modulated transport coefficients observed in the core of this discharge reflect this reduced transport. Modulated diffusion in the core of the negative triangularity discharge (shown in Fig.) is lower than any other case considered here.

Modulated convection (Fig.) shows a much different shape, and is smaller than the other observed L-modes as well.

5.6 Linear Scaling of b with Fluctuation Level

The range of deposition widths and edge conditions have been combined to produce a beam broadening scaling with fluctuation amplitude in the edge ($\rho \approx .95$). Across the dozens of discharges in the dataset, propagation angle and deposition location may not always be identical. Previous work has shown that fluctuation amplitude and path length through fluctuations define a broadening factor which is otherwise path independent[6]. To produce a large variation in turbulence amplitude, multiple discharge conditions are considered. Selected intervals for data analysis have in excess of 15 modulations periods, and show density variations less than 1%.

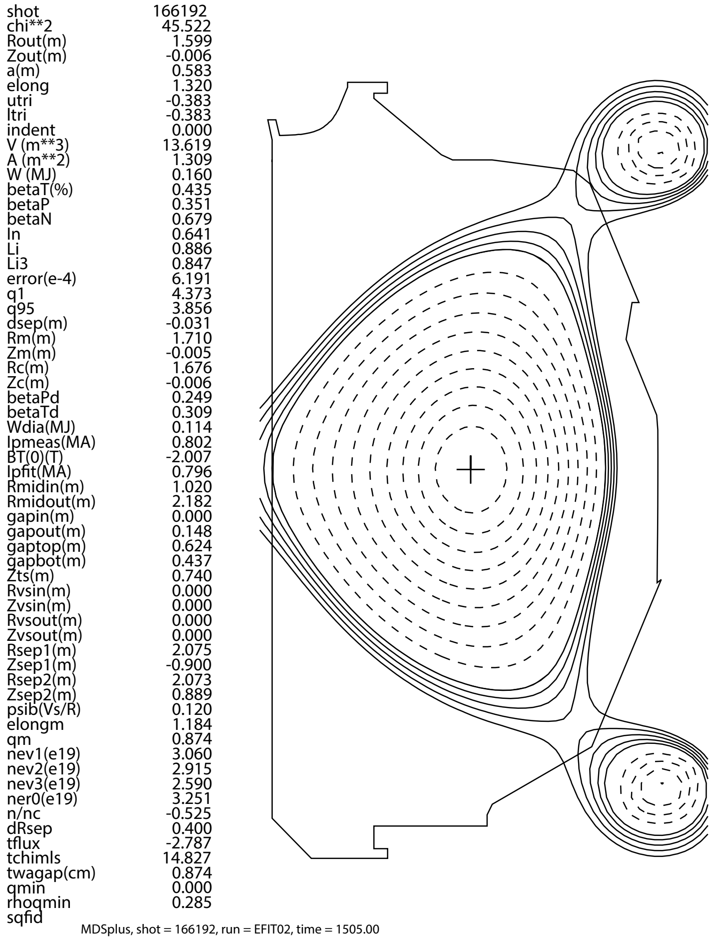

shot	166192
chi**2	45.522
Rout(m)	1.599
Zout(m)	-0.006
a(m)	0.583
elong	1.320
utri	-0.383
ltri	-0.383
indent	0.000
V (m**3)	13.619
A (m**2)	1.309
W (MJ)	0.160
betaT(%)	0.435
betaP	0.351
betaN	0.679
In	0.641
Li	0.886
Li3	0.847
error(e-4)	6.191
q1	4.373
q95	3.856
dsep(m)	-0.031
Rm(m)	1.710
Zm(m)	-0.005
Rc(m)	1.676
Zc(m)	-0.006
betaPd	0.249
betaTd	0.309
Wdia(MJ)	0.114
Ipmeas(MA)	0.802
BT(0)(T)	-2.007
Ipfit(MA)	0.796
Rmidin(m)	1.020
Rmidout(m)	2.182
gapin(m)	0.000
gapout(m)	0.148
gaptop(m)	0.624
gapbot(m)	0.437
Zts(m)	0.740
Rvsin(m)	0.000
Zvsin(m)	0.000
Rvsout(m)	0.000
Zvsout(m)	0.000
Rsep1(m)	2.075
Zsep1(m)	-0.900
Rsep2(m)	2.073
Zsep2(m)	0.889
psib(Vs/R)	0.120
elongm	1.184
qm	0.874
nev1(e19)	3.060
nev2(e19)	2.915
nev3(e19)	2.590
ner0(e19)	3.251
n/nc	-0.525
dRsep	0.400
tflux	-2.787
tchimls	14.827
twagap(cm)	0.874
qmin	0.000
rhoqmin	0.285
sqfid	

MDSplus, shot = 166192, run = EFIT02, time = 1505.00

Figure 5.13: The cross section of a negative triangularity discharge is sharply different than those shown earlier in this work. The D-shape of DIII-D is inverted, with positive consequences for both confinement and fluctuation level.

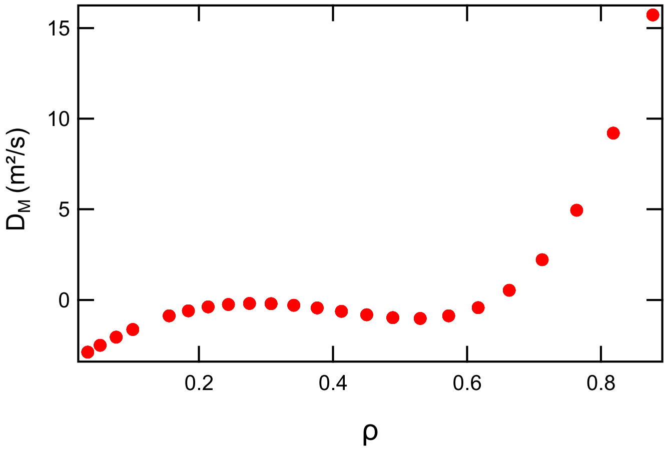

Figure 5.14: Modulated diffusion in the negative triangularity discharge is suppressed throughout the core. Only in the very edge does it approach the levels of a standard L-mode.

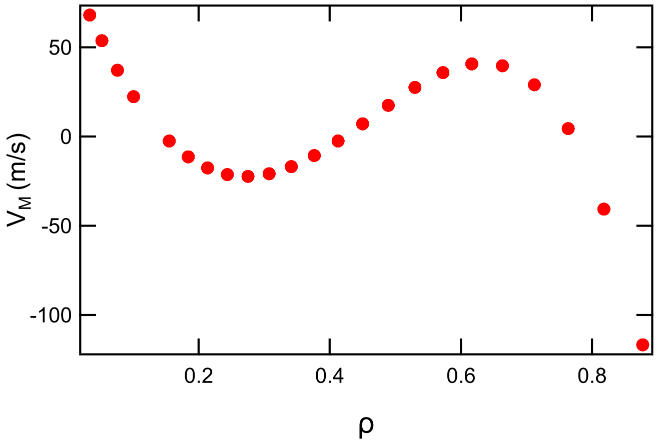

Figure 5.15: Again, the convection coefficient for the negative triangularity L-mode looks very different from those others studied. Reduced transport in this discharge appears to extend beyond the steady state coefficients to the modulated coefficients as well.

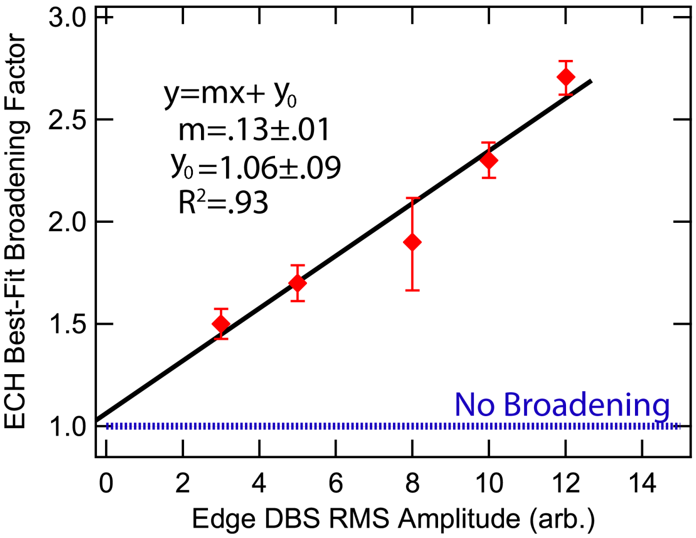

Figure 5.16: A collection of 19 discharges in 5 conditions have both fluctuation data and modulation needed to form a scaling. Broadening of the narrow RF beam used in deposition calculated in TORAY-GA will lead to a corresponding increase in deposition width. The horizontal axis is the normalized amplitude from the Doppler backscattering system at $\rho = .95$. The vertical axis is the factor increase in deposition profile width over TORAY-GA's equilibrium, no-fluctuation deposition FWHM in ρ. This approximation holds for DIII-D's launcher, which is 25 degrees above the major axis.

Fit ranges are selected to avoid magnetic islands and the edge localize mode-perturbed edge of H-mode plasmas, whose temperature effects can extend from the edge $\rho = .6$.[86] Figure 5.16 shows these broadening factors assembled by discharge condition. Uncertainties in the experimental data are derived from the statistical interpretation of χ^2. An increase in the reduced goodness of fit, χ^2_ν , by a standard deviation is taken as an approximate 1σ value for b, producing a 10-25% uncertainty in broadening factor.

b factors are substantial, contrary to some expectations that the level of scattering observable in current generation devices is small[2]. Still, such a substantial degree of scattering presents an opportunity as well. These experiments are already being used as a test for a generation of ray and beam tracing codes which are sensitive to the effects of fluctuations[4][3].

5.6.1 Addressing Confounding Factors

These microwave deposition profiles are substantially broader than predicted in past power deposition analysis on DIII-D[87] and in experimental benchmarking of ECCD deposition[88]. In those studies, beam deposition was found to be comparable to the ray tracing predicted widths when significant transport coefficients were applied. One flaw in much of those forms of analysis is that they did not attempt to fit across frequencies of the Fourier transform simultaneously. Time evolution, in the Fourier domain, becomes frequency dependence. Thus fitting across harmonics simultaneously, as done in this work, is a test of the causality of the heat flux.

This causal sensitivity is likely the reason for the wildly varying, often aphysical diffusivity that come with an incorrect degree of broadening. Broadened deposition implies that power appears immediately in a wider region. The temperature perturbations associated with heating extend far outside the heating region because of transport - they are non-negligible even at $\rho = .8$ when core heating. Figure 5.17 shows the radial extent of the Fourier transformed perturbation for a high power case. Clearly transport must match the amplitude variation, but more subtly it must also match the phase information.

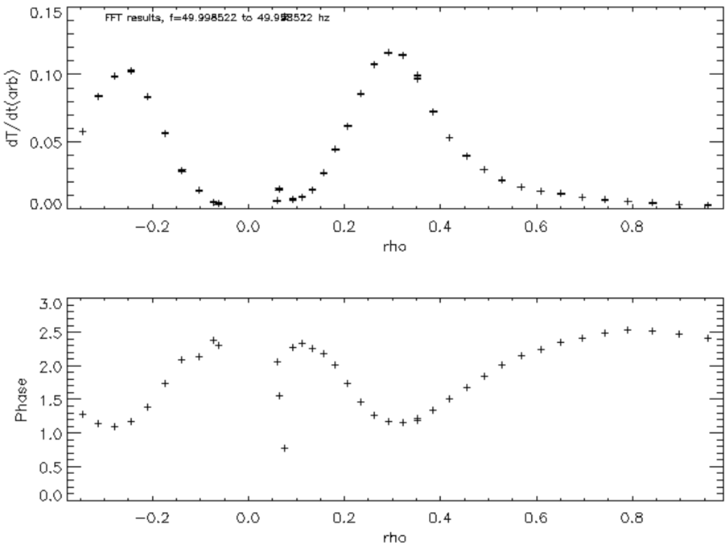

Figure 5.17: The Fourier analyzed $\tilde{T}_e$ profile has nonzero signal far from the deposition region, with phase and temperature perturbations coherent with the ECH driven all the way to the plasma edge. In the integral formulation, the value of flux at every point depends on the perturbation inside that radius. The phase relationship even far from the deposition region is therefore sensitive to the choice of source function - power transported from a narrow deposition region may replicate the correct amplitude, but will not have the correct phase due to the time lag implicit in linear transport.

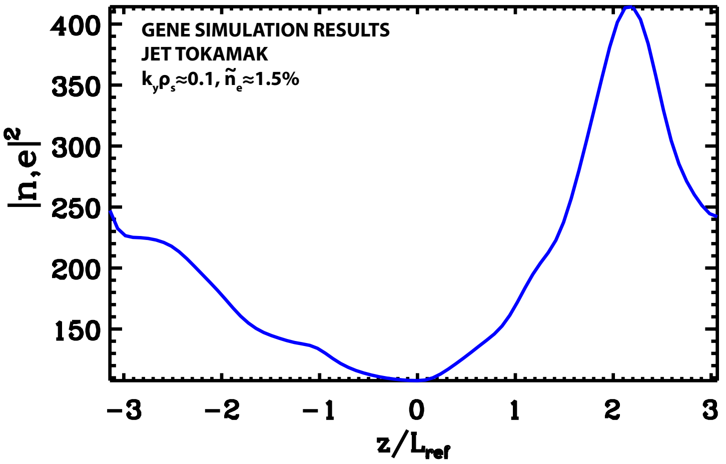

Figure 5.18: GENE gyrokinetic simulations of electron turbulence driven by microtearing modes[89] on JET. Turbulent fluctuation amplitude is plotted against a poloidal angle proxy. $z/L_{ref} = 0$ is equil (Fig. CO D. R. Hatch)

Not all deposition studies find consistency with ray tracing codes. The author points to the study of Kirov *et. al.*[83], which contain the most robust transport modeling. Experimental studies using the ASTRA transport code and TORBEAM derived deposition found broadening factor of approximately 2. This is despite the fact that TORAY-GA has been benchmarked and found good agreement in deposition width with the TORBEAM code[49].

Questions have also been raised about the poloidal variation in the level of fluctuations. Simulations from David Hatch at the University of Texas show a clear relation between poloidal angle to fluctuation amplitude. Simulations with the gyrokinetic GENE code show that the level of scattering relevant fluctuations (those with $k_y\rho \approx 2$), are actually minimal on the midplane.

Chapter 6

Implications of Broadening for ITER and Conclusions

6.1 Targeted Modes

On ITER, both 3/2 and 2/1 tearing modes will be targeted for ECCD suppressions. Literature references based on fluctuation-free current drive profiles inform the expected power requirements. A total of 25 MW of EC power are planned for all purposes in ITER. The 3/2 mode is expected to require $\approx 7MW$ of constant power to suppress. Growth of this mode is slow, on the order 5 seconds, so gyrotrons will likely have time to turn on and track the island structure[90]. The 2/1 mode has a substantially higher risk of locking, and it can grow from seed islands to a size of 5 cm in only 2-3 s, at which point it begins to risks locking and disrupting the plasma[42]. Locking could generate such large prompt heat fluxes as to damage the inner wall of ITER, and as such must be avoided.

6.2 Profile Flattening

Even in the absence of locking, islands have a significant impact on core ion temperature, and thus to fusion gain. Unsuppressed islands cause a temperature profile flattening, which can be estimated following the method of Sauter and Zohm[91]. In this formulation, fusion gain cost of an island chain is assessed as a function of the profile flattening it drives. Equation 6.1 gives a reduction in the ion temperature T_i as a function of the radial location of the tearing mode r_{TM}, the width of the island, w_s, and the plasma minor radius, a.

$$\frac{\Delta T_i}{T_i(r=0)} \approx -4\frac{r_{TM}^3 w_s}{a^4} \tag{6.1}$$

The overall reduction in ion temperature has a cost in terms of fusion product, which is simply estimated as a 5/2 factor in the ion temperature.

$$\frac{\Delta P_{fusion}}{P_0} \approx -\frac{5}{2}\frac{\Delta T_i}{T_i(0)} \tag{6.2}$$

Failure to suppress these islands will limit the maximum Q achievable on ITER, even in the absence of locking. Unsuppressed islands cause a profile flattening, which can be estimated according to the formulation of Sauter and Zohm[91]. An unsuppressed 2/1 mode will limit Q to 4, due to T_i flattening, while an unsuppressed 3/2 limits Q to 7. However, it must be noted that fusion gain is impacted by both unsuppressed islands and by always-on EC power use. ITER is expected to use 50 MW of power in its baseline configuration, and thus with an expected fusion power of 500 MW, a gain of Q=10 can be achieved[92]. Constant use of the 25MW of gyrotron power limits maximum gain to Q=6.7. The cost in fusion gain for these processes in expressed in Figure 6.1.

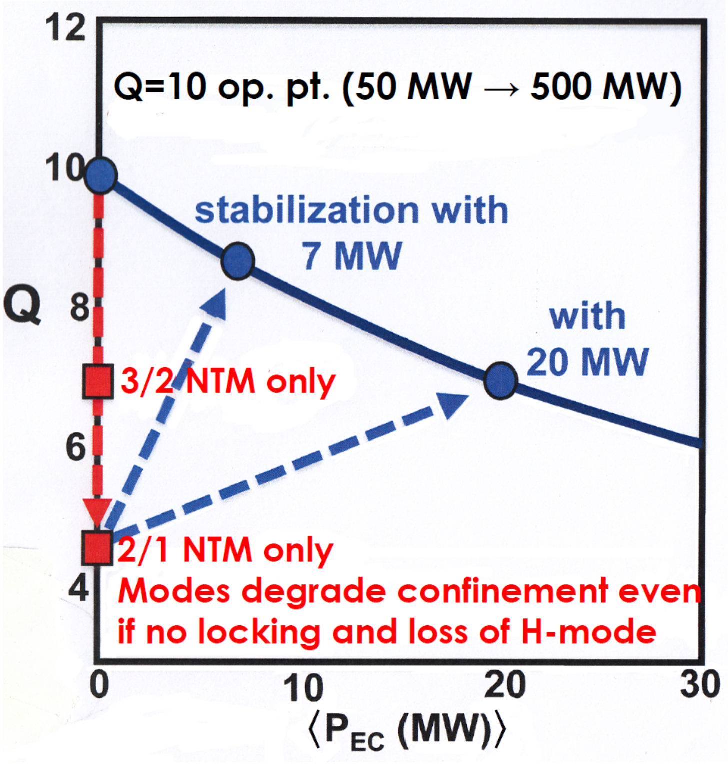

Figure 6.1: This diagram shows the cost in terms of fusion gain, Q, of either suppressing tearing modes or leaving them unsuppressed. This discounts the risk of locking. Islands are associated with a degree of profile flattening, which can be calculated based on the formulation of Sauter [91]. There is a trade-off, in that the use of ECH power increases the input power which defines the gain $Q = P_{fusion}/P_{in}$ (Fig. courtesy of R.J. Haye).

6.3 Predicting Costs of Broadening on ITER

Fluctuation broadening of the ECH beams of the magnitude observed on DIII-D is plausible for ITER. While fluctuation levels are lower, 30% on DIII-D[61] as compared to 10% on ITER[2], the path length through the plasma is over ×3 longer. Studies made using the beam-tracing WKBEAM code provide information on the power cost of deposition broadening on ITER[93]. The width of the beam relative to the current drive profile has been explored as a free variable. When the width of the ECCD profile is less than that of the current, only the total current deposited is relevant. When power deposition is wider than the targeted island that suppression becomes more expensive as power is lost outside the island chain.

With this in mind, estimates for a factor of ×2 deposition broadening, which is typical of these discharges, render full suppression difficult, but not impossible. Assuming use of narrower deposition from the lower launcher module, and correct alignment, power costs can be estimated from the work of Poli *et. al.* [93]. 3/2 suppression requirements will nearly double, to $12MW$. Costs for the wider 2/1 mode are increased by a smaller factor, to $10MW$. Efforts using experimentally-benchmarked simulation codes, capable of resolving the effects of broadening, are strongly advised based on these results. With the use of O-point modulation [42], costs increase only 30% for 2/1 suppression with ×2 broadening[93]. Development of intelligent mode detection and ECCD modulation schemes[94][95] is, in the author's opinion, the best way to insure that the available power is sufficient for full suppression, guaranteeing the viability of ECCD NTM suppression to contribute to ITER's high gain mission.

6.4 Conclusions

In this work, a linear transport model was used to fit the electron heat flux generated by electron cyclotron heating. Deposition was found to be x1.7-2.8 wider than predicted by ray tracing through a no-fluctuation equilibrium, increasing linearly with edge turbulence amplitude. Experimental broadening factors are found to be consistent with full wave simulations, but indicate a broader deposition than modern beam and ray tracing codes which do not take into account full wave mechanics and make simplifying assumptions about turbulence. Transport is fit with a 3-term model which includes diffusion, convection, and coupled transport effects. This fitting produces a consistently broadened deposition, which scales with density fluctuation amplitude.

A paper containing some of the crucial points of this work is in review for submission to *Nuclear Fusion*. A significant simulation effort, detailed only briefly in this thesis, is also underway and will result in a PhD thesis for Matthew Thomas of the University of York. The simulation paper complimenting the experimental work finds a consistent degree of broadening in 3 DIII-D cases where full wave analysis has been performed. This work has provided the first experimental confirmation of fluctuation broadening of ECH deposition, and will provide benchmarking for future simulation efforts. The transport fitting routines developed also have the potential to enhance understanding of multivariate transport in plasmas. Future work could include expanding these methods to density transport in tokamaks, and analysis of other forms of modulated transport besides that induced by microwave heating.

Bibliography

[1] H. Kyriakos & A. K. Ram Phys. Plasmas **17**, 022505 (2010)

[2] A. Köhn *et al*, *Plasma Phys. Control. Fusion* **58** 105008 (2016)

[3] M.B. Thomas *et al*, *In preparation for Nuclear Fusion* (2017)

[4] Y. Peysson et Al Plasma Phys. Control. Fusion **53**, 124028 (2011)

[5] M.W. Brookman *et al*, Rev. Sci. Inst **87**, 11E517 (2017)

[6] M.W. Brookman *et al*, Proc. EC19, EPJ Web *Accepted for Publication* (2017)

[7] U.S. Energy Information Administration, ”US Crude Oil and Natural Gas Reserves”, (2016) /urlhttps://www.eia.gov/naturalgas/crudeoilreserves/

[8] U.S. Energy Information Administration, Petroleum Spot Prices”, (2017) /urlhttps://www.eia.gov/dnav/pet/hist/LeafHandler.ashx?n=PET&s=RWTC&f=A

[9] A. C. C. Sips *et al*, Plasma Phys. Control. Fusion **47** (2005)

[10] M.S. Andersen, Ecological Indicators **79** 11 (2017)

[11] R.A. Rohde & R.A. Muller , PLoS ONE **10**(8): e0135749 (2015) https://doi.org/10.1371/jour

[12] International Panel on Climate Change, Climate Change 2014: Synthesis Report. IPCC, Geneva, Switzerland (2014)

[13] J.R. Hansen, Rev. Geophys. **48**, RG4004 (2010)

[14] Authors Note: I alloted myself one joke for the body of this work. Other jokes are incidental, and should not be considered funny.

[15] J. Wesson, *Tokamaks* Oxford Science Publications (2011)

[16] A.S. Kadyrov Phys. Rev. Lett. **114** 183201 (2015)

[17] Eurofusion Consortium, Retrieved 6/13/17, `https://www.euro-fusion.org/2005/12/50-years-of-lawson-criteria/`

[18] D. Maisonnier *et al*, Nuclear Fusion **47** 1524 (2007)

[19] R. E. Bilstein, *Stages to Saturn: A Technological History of the Apollo/Saturn Launch Vehicles* NASA SP-4206.(1996)

[20] V. C *et al*, *Plasma Physics and Controlled Fusion*

[21] T. J. Dolan /textitet al, Phys. Rev. Letters **5** 141 (1960)

[22] R.F. Post /textitet al SUMMARY OF UCRL PYROTRON (MIRROR MACHINE) PROGRAM `retrieved:https://www.osti.gov/scitech/biblio/4275223` (1959)

[23] A.A. Ivanov and V. V. Prikhodko, Plasma Phys. & Ctrld. Fusion **55** 063001 (2013)

[24] T. Klinger *et al*, Plasma Phys. Control. Fusion **59** 014018 (2017)

[25] K.H. Burrell , *et al*

[26] C. Petty and T. Luce *et al*, Nucl. Fusion **34**(1) 121, (1994)

[27] B. Crowley *et al*, Fusion Eng. and Design **96-97** 443 (2015)

[28] J. Lohr *et al*, Journal of Infrared, Millimeter, and Terahertz Waves. **37** 22 (2016)

[29] D.M. Ponce-Marquez *et al*, Rev Sci Instrum.**10**, 81 (2010)

[30] P. Gohil *et al*, Fusion Engineering **2** 1199 (1991)

[31] M. E. Austin and J. Lohr, *Rev. Sci. Instrum.* **74** 1457 (2003)

[32] James Clerk Maxwell. "On Faraday's lines of force". Transactions of the Cambridge Philosophical Society,**10** , pp. 27-83 (1856)

[33] D. A. Boyd *et al* The Physics Teacher **25** 22 (1987)

[34] W. Horton and G. Hu,*Turbulent Transport in Magnetized Plasmas* World Scientific Publishing (2012)

[35] I.H. Hutchinson *Principles of Plasma Diagnostics* Cambridge University Press (2002)

[36] R. Fitzpatrick, Lecture Notes, Retrieved 7/14/2017 from `https://farside.ph.utexas.edu/teaching/plasma/Plasma/node75.html`

[37] V. Erckmann and U. Gasparino , Plasma Phys. Ctrl. Fusion **36** 1869-1962 (1994)

[38] Bornatici M.,"Theory of electron cyclotron absorption of magnetized plasmas." Plasma Physics ,**24**(6) 629 (1982)

[39] R. Chatterjee *et al* Fusion Engineering and Design **53** 113 (2001)

[40] C.T. Holcomb *et al* Nucl. Fusion **54** 093009 (2014)

[41] A. YoungHwa *et al*, Nucl. Fusion **57** 016001 (2017)

[42] R. J. La Haye *et al*, Nucl. Fusion **46** 451 (2006)

[43] Kobayashi T. *et al*, Plasma and Fusion Research, **3** 014-1-014-3 (2008)

[44] C.C. Petty *et al* Phys. Rev. Lett. **83** 3661 (1999)

[45] L. Schmitz *et al*, Nucl. Fusion **52** 023003 (2012)

[46] R.J La Haye *et al*, ECA **25A**, 1357 (2001)

[47] R.J. La Haye *et al*, Nucl. Fusion **57** 014004 (2017)

[48] R. J. La Haye *et al*, AIP Conference Proceedings **1689** 030018 (2015)

[49] R. Prater *et al*, Nucl. Fusion **48**, 035006 (2008)

[50] M. Zerbini *et al*, Plasma Phys. Control. Fusion **41** 931 (1999)

[51] P. Mantica *et al*, Phys. Rev. Lett. **95**, 185002 (2005)

[52] R. Prater *et al*,, Nucl. Fusion **48** 035006 (2008)

[53] J. Decker et Al, EPJ Web of Conf. **32**, 01016 (2012)

[54] Y. Peysson *et al*, Plasma Phys. Control. Fusion **54**, 045003 (2012)

[55] B.D. Dudson and J. Leddy: *Submitted to PPCF* https://arxiv.org/abs/1609.03360 (2016)

[56] W. Horton *et al*, Plasma Phys. Controlled Nucl. Fusion **29**, 901 (1987).

[57] C. Holland *et al*, Nuclear Fusion **56** 066043 (2017)

[58] T. L. Rhodes *et al*, Physics of Plasmas **9** 2141 (2002)

[59] T. L. Rhodes *et al*, Rev. Sci. Instrum. **81** 10 (2010)

[60] G.R. McKee *et al*: *Plasma and Fusion Research: Regular Articles* **2** S1025 (2007)

[61] M.W. Shafer *et al*, *Phys. Plasmas* **19** 032504 (2012)

[62] A. K Ram *et al*,Physics of Plasmas 056110 (2013)

[63] B.D. Dudson *et al*: *Computer Physics Communications* **180** 1467-1480 (2009)

[64] A. Hasegawa and M. Wakatani: *Phys. Rev. Lett.* **50** 9 (1983)

[65] P.C. Strangeby: *The Plasma Boundary of Magnetic Fusion Devices* Taylor & Francis (2000)

[66] S.J. Zweben *et al*, *Plasma Phys. Control. Fusion* **49** 7 (2007)

[67] T.R.N. Williams *et al*, *Plasma Phys. Control. Fusion* **56** 075010 (2014)

[68] F. Ryter *et al*, Nucl. Fusion **49** 062003 (2009)

[69] R.E. Stockdale, K.H. Burrell, W. Tang, Bull. Am. Phys. Soc. **31** 1535. (1986)

[70] K.W. Gentle *et al*, Phys. Fluids **31**, 1105 (1988)

[71] L. Guidi *et al*, J. Phys.: Conf. Ser. **775** 012005 (2016)

[72] Weisen H. *et al*, Nucl. Fusion **41**, 1227 (2001)

[73] C. Sung *et al*, Rev. Sci. Instrum. **87**, 11E123 (2016)

[74] T. N. Carlstron *et al*, Rev. Sci. Instrum. **61** 2865 (1988)

[75] F. J. Casson *et al*, Nucl. Fusion **55** 012002 (2015)

[76] C.C. Petty *et al*, Fusion Sci. and Tech. **57**.1 10 (2010)

[77] R. W. Harvey *et al*, Phys. Rev. Lett. **88** 205001 (2002)

[78] P.T. Boggs *et al*, Contemporary Mathematics **112**, 186 (1990)

[79] J. C. Rost *et al*, Physics of Plasmas **21** 062306 (2014)

[80] A. Marinoni *et al* ,Plasma Phys. Control. Fusion **51** 055016 (2009)

[81] C.L. Rettig, *et al*, Nucl. Fusion **33** 643 (1993)

[82] E.D. Fredrickson *et al*, Phys. Rev. Lett. **65**, 2869

[83] K.K. Kirov *et al*, Plasma Phys. Control. Fusion **44** 2583-2602 (2002)

[84] M.E. Austin *et al*, 58th Annual Meeting of the Division of Plasma Physics of the American Physical Society, JP10.00112 (2016)

[85] A. W. *et al* Plasma Phys. Control. Fusion **44** 945 (2002)

[86] A. W. Leonard *et al*, Plasma Phys. Control. Fusion **44** 945 (2002)

[87] . M Zerbini *et al*, Plasma Phys. Control. Fusion **41** 931 (1999)

[88] C.C. Petty *et al*, Nucl. Fusion **42**, 1366 (2002)

[89] D. R. Hatch *et al*, *Nucl. Fusion* **56**10 104003 (2016)

[90] F. Poli *et al*, Bull. Amer. Phys. Society., Poster presented at APS-DPP 2016, TO4.00013 `https://www.burningplasma.org/resources/ref/APSDPP%202016/TO4.00013_Poli.pdf` (2016)

[91] O. Sauter, H. Zohm, ECA **29C** P-2.059 (2005)

[92] G.L. Jackson *et al*, Nucl. Fusion **55** 023004 (2015)

[93] E. Poli *et al*, Nuclear Fusion **55.1** 013023 (2015)

[94] W. Kasparek *et al*, Nucl. Fusion **56** 126001 (2016)

[95] E. Kolemen *et al*, Nucl. Fusion **54** 073020 (2014)

[96] Retrieved from ITER organization website 5/13/2016 `https://www.iter.org/FactsFigures`

[97] H. Renner *et al*, Nucl. Fusion **40** 1083 (2000)

[98] W. Horton *et al*, Phys. Plasmas **13**, 042513 (2006)

[99] H. Kyriakos & Ram A.K. Phys. Plasmas **17**, 022505 (2010)

[100] Y. Peysson *et al*, Plasma Phys. Control. Fusion **53**, 124028 (2011)

[101] C.L. Rettig *et al*, Nucl. Fusion **33**, 643 (1993)

[102] K.K. Kirov *et al*, Plasma Phys. Ctrl. Fusion **44**, 2583 (2002)

[103] D. R. Ernst *et al*, 25th IAEA Fusion Conference EX/2-3 (2014)

[104] Y. Peysson & J. Decker *et al.* F.S.T 65, 22 (2014)

[105] P. Nikkola *et al*, Nucl. Fusion **43** 1343 (2003)

[106] K.W. Gentle *et al*, Phys. Plasmas **13**, 012311 (2006)

[107] Harvey R.W. *et al*, Phys. Rev. Lett. **88**, 205001 (2002)

[108] R.E. Stockdale *et al*, Bull. Am. Phys. Soc. **31**, 1535 (1986)

[109] J.C. deBoo *et al*, Phys. Plasmas **19**, 082518 (2012)

[110] Z. Chang and J.D. Callen,Nucl. Fusion **30** 219 (1990)

[111] Y. Peysson *et al*, Plasma Phys. Control. Fusion **53**, 124028 (2011) K. Zhurovich *et al*, Rev. Sci. Instrum. **76**, 053506 (2005)

[112] M. W. Brookman *et al*, *In preparation for Nuclear Fusion* (2017)

Vita

Michael William Brookman

The author, Michael Brookman, was born in Rockford, IL. He would like to thank Tom and Lea Brookman for their participation in this foundational effort. He's also writing this section in the third person for consistency. Long hours in the school library gave Michael a lifelong interest in science fiction. As he approached graduation from Brodhead High School, in Brodhead, Wisconsin he was asked to contemplate a future career. 'What could be more satisfying than making science fiction real', he thought. After a visit to the University of Wisconsin's Madison Symmetric Torus, Michael felt that fusion energy was not only interesting, but also vital to mankind's future. Michael enrolled as a physics major, joined the MST group after his freshman year.s. Working with Abdulgader Almagri gave him an excellent foundation in experimental physics. After his graduation, he was invited by Dr. William Rowan at the Institute of Fusion Studies, to joint the group in the summer of 2011. He started graduate studies that Fall, working on Alcator C-mod during semester breaks. He moved to lovely San Diego, CA in 2014. Max Austin provided key developmental guidance and an introduction to plasma diagnostics. With the help of innumerable scientists, technicians, and engineers, Michael has completed his Graduate Studies, and is now ready to embark on a career with

General Atomics in San Diego, CA.

When he's not trying to understand microwaves, Mike enjoys cooking, weight lifting, and cat herding.

Permanent address: 3938 Florida St
San Diego, CA, 92104

This dissertation was typeset with LaTeX[†] by the author.

[†] LaTeX is a document preparation system developed by Leslie Lamport as a special version of Donald Knuth's TeX Program.